Understanding Hot to Ultra Hot Jupiters through General Circulation Models and High Resolution Spectroscopy

by

Hayley Beltz

A dissertation submitted in partial fulfillment
of the requirements for the degree of
Doctor of Philosophy
(Astronomy and Astrophysics)
in The University of Michigan
2023

Doctoral Committee:

Associate Professor Emily Rauscher, Chair
Professor Fred Adams
Professor Michael Meyer
Professor John Monnier

Hayley Beltz

hbeltz@umich.edu

ORCID iD: 0000-0002-6980-052X

I dedicate this thesis to every dog I have had the pleasure of petting

and to my 10-year old self,

who would have thought current me is impossibly cool.

ACKNOWLEDGEMENTS

"Despite everything, it's still you."

– Toby Fox, *Undertale*

I could not have completed this thesis without the support of so many people lifting me up.

I want to thank Emily Rauscher for being an incredible advisor over the past five years and creating an environment where I can learn and grow. (Even if I *still* need to be reminded to choose my battles carefully)

My graduate cohort is comprised of some of the best young scientists I know and individuals I consider myself very lucky to be able to call friends. I think we've helped shape the department for the better, and I hope we see each other at AAS meetings in the years to come.

This work would not of been possible without the help of collaborators. Isaac Malsky deserves a special mention for his remarkable code-gremlin abilities that helped expand the breadth of science I was able to accomplish and the numerous quality-of-life upgrades resulting from his computational skills. I also want to thank Arjun Savel, who helped with much of the post-processing.

Finally, I also want to thank my parents, who have always believed in me, even when I didn't believe in myself. Sending me to space camp all of those years ago sure paid off, huh?

From the bottom of my heart, thank you.

TABLE OF CONTENTS

LIST OF FIGURES

Figure

LIST OF TABLES

Table

ABSTRACT

With orbital periods of only a few days, hot Jupiters and the even hotter ultrahot Jupiters are classes of planets that exist in an irradiation regime unlike anything in our solar system. These atmospheres are drastically influenced by the extreme levels of irradiation from their host star. Due to their proximity, these planets are expected to become tidally locked into synchronous orbits, meaning that their rotation period and orbital period are equal. This results in a permanent dayside and nightside on the planets, causing the large scale atmospheric dynamics of these objects to be governed by heat redistribution. In addition, these extreme temperatures cause atmospheric species to ionize on planet daysides, which can contribute to the lack of uniformity in the spatial distribution of species in these planets' atmospheres. The movement of these ions also opens the door to interactions with the planet's magnetic field.

Very little is known about how magnetic effects can shape the atmospheres of these planets. In order to understand these planets more thoroughly, I use two main tools: 3D numerical modeling and high resolution spectroscopy. In this thesis, I explore multiple numerical treatments of magnetic effects, highlighting the strengths and weaknesses of each. Using our model's state-of-the-art kinematic magneto-hydrodynamic (MHD) approach, I characterize a magnetic circulation regime that manifests in the upper atmosphere of ultrahot Jupiters as a result of our magnetic drag treatment. I also dive into the observational signatures of this regime, reviewing the effects on phase curves, emission, and transmission spectroscopy. Too often are magnetic effects ignored in analyses and models, and this thesis works to emphasize the importance of these effects.

CHAPTER I

Introduction

"I am finally getting the recognition I have always given myself"

– Peggy Hill

1.1 Hot and Ultrahot Jupiters

The year I was born, there were fewer than 10 confirmed exoplanets. Now, as I write this dissertation, the number exceeds 5,000[1]. These planets vary in size, composition, and irradiation, residing often in unique environments for which we have no basis of comparison in our solar system. In less than 30 years, exoplanet astronomy has exploded in growth thanks to the work of countless individuals and advancements in observing techniques and theoretical modeling. From utilizing the *Hubble Space Telescope, (HST)*—a telescope launched prior to the confirmation of *any* exoplanet—to uncover atmospheric information of nearby planets to becoming the second-largest category[2] of applied time for Cycle 2 of *JWST*[3], the field of exoplanets has created a

[1]https://exoplanetarchive.ipac.caltech.edu/

[2]https://www.stsci.edu/contents/news/jwst/2023/jwst-observers-submitted-a-record-breaking-number-of-proposals-for-cycle-2

[3]For the purpose of this dissertation, I will only refer to this telescope by its acronym, due to its namesake's participation in the Lavender Scare during his time at NASA and in the US government. It is my hope that one day, this amazing instrument will be renamed after a more deserving individual.

firm foothold in the field of astronomy in a short period of time.

In addition to finding exoplanets, astronomers are now able to characterize their atmospheres in many ways, such as detecting the presence of molecules or even measuring wind speeds. This process, which often combines observations and theoretical atmospheric models, has allowed the field's understanding of planet diversity to grow. The biggest and hottest of these planets, where many of these techniques were first used, will be the focus of this dissertation. Hot Jupiters (HJs) and their even hotter counterparts, ultrahot Jupiters (UHJs), are gas giant planets that orbit extremely close to their host stars, inhabiting an irradiation regime not seen in our solar system. Due to the favorable flux contrast ratios with their host starts, these planets are often great observational targets for multiple observational methods. For the purpose of this dissertation, we consider a hot Jupiter to be roughly a Jupiter sized planet (radius between $\sim 0.6\ R_{Jup}$ and $2\ R_{Jup}$) orbiting their host star in $\lesssim 10$ days (*Gan et al.*, 2023). When the equilibrium temperature of the planet surpasses 2200 K, the planet enters the UHJ regime (*Tan and Komacek*, 2019).

It is important to consider HJs and UHJs in context with the known distribution of exoplanets. In alignment with the time honored tradition for any exoplanet talk or dissertation, Figure 1.1 shows the period and mass distribution for all known exoplanets. The blue oval has been added to roughly indicate the parameter space for HJs and UHJs. Due to their relative ease of detection, this parameter space is highly populated compared to other categories of exoplanets. HJs' and UHJs' large masses and short orbital periods make these planets ideal targets for discovery via radial velocity and transits, the two most common methods for finding exoplanets.

Because of this ease of detection, our total population of exoplanets are biased towards these planets, meaning that they are over-represented in the exoplanet catalogue. Recent exoplanet demographic work[4] suggests these planets are actually

[4]It should be noted that most demographic surveys do not differentiate between hot Jupiters and ultrahot Jupiters, instead classifying them all as hot Jupiters

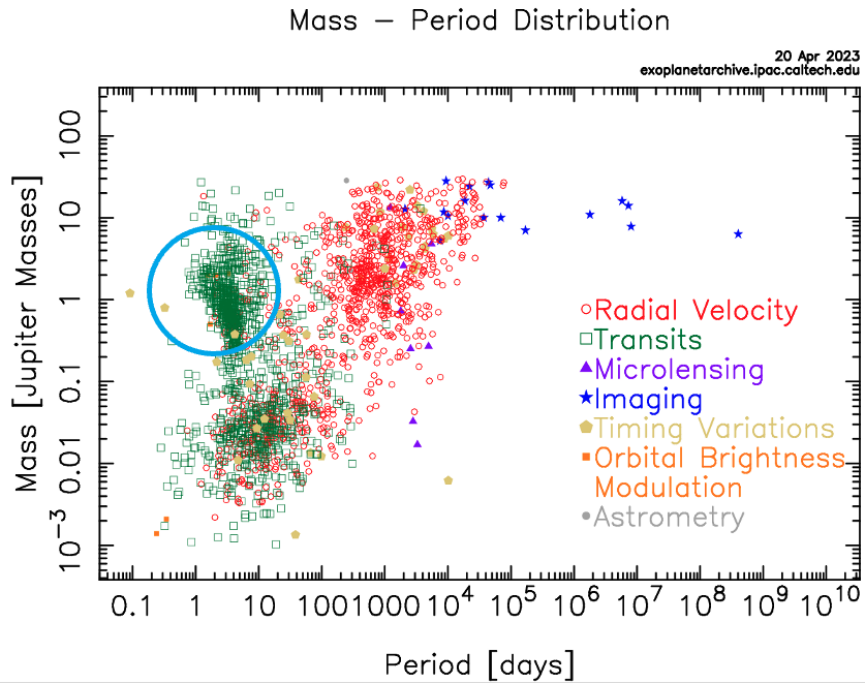

Figure 1.1 Distribution of exoplanets by period and mass, color coded by their method of detection. The approximate location of hot and ultrahot Jupiters are shown with the blue oval.

quite rare. A recent review by *Zhu and Dong* (2021) calculates a frequency rate of $0.62 \pm 0.09\%$. There is also a dependence on host star, with *Gan et al.* (2023) reporting a $0.27 \pm 0.09\%$ occurrence rate for hot Jupiters around M dwarfs. Looking at FGK stars, *Wittenmyer et al.* (2020) reports a frequency of $0.84^{+0.70}_{-0.20}\%$. I show a plot from *Gan et al.* (2023) in Figure 1.2 which summarizes various efforts in constraining this frequency for different stellar host types. *Zhu and Dong* (2021) notes that RV surveys tend to return higher frequency rates for these planets compared to transit surveys. This may be due to stellar host differences as RV surveys often exclude close stellar binaries from their sample. The metallicity of the host star also plays a role, with higher metallicity stars being slightly more likely to host hot Jupiters. (*Guo et al.*, 2017).

In spite of their overall rarity among the planet population, hot and ultrahot Jupiters offer a window into physical regimes not often seen, making them excellent

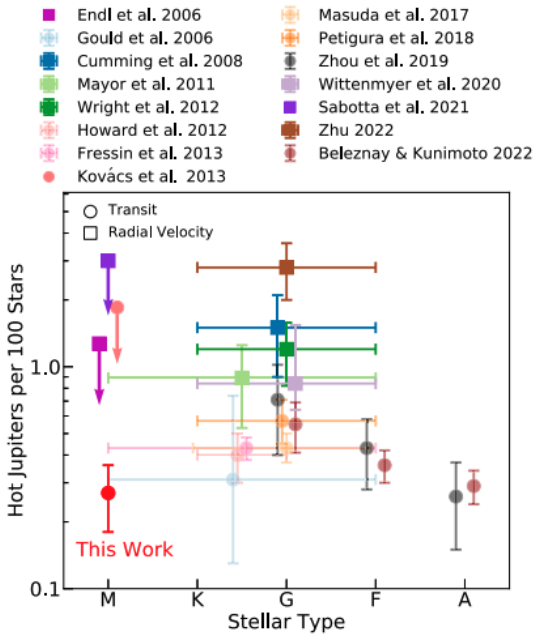

Figure 1.2 Occurrence rates of hot Jupiters from different demographic studies, originally appearing as Figure 13 in *Gan et al.* (2023)

"laboratories" for testing our understanding of the physical mechanisms operating at these high temperatures. In addition, these planets are ideal for testing techniques and instruments on high signal to noise data, which can inform how these techniques are used for smaller, dimmer planets.

1.2 Observational Methods for Atmospheric Characterization

There are a variety of different methods that astronomers use to study the atmospheres of exoplanets. The most common of which include phase curves, emission spectroscopy, and transmission spectroscopy. In this dissertation I focus on *high resolution* spectroscopy, which requires different data reduction and interpretation techniques than lower resolution methods. The general principle of the observational techniques remain the same though; emission spectroscopy measures the thermal emission from a planet's atmosphere and transmission spectroscopy measures starlight that has

been filtered through the planet's atmosphere, when the planet blocks light from the host star during transit. Each of these observational techniques can probe different pressure regions of the planet atmosphere, and combining them together can help build a picture of composition, structure, and/or dynamics of a planet's atmosphere.

1.2.1 Phase Curves

Phase curves are a powerful observational tool that provides multi-dimensional information of a planet's atmosphere. This technique involves measuring the planet's emitted flux over a wavelength band throughout its entire orbit. Hot and ultrahot Jupiters are some of the only planets astronomers have full coverage phase curves of due to their short orbital periods. Since the whole orbit of the planet is covered, instruments like *HST* or *JWST* can measure the disk-integrated flux around the entire planet. From this, the difference in flux from the brightest and dimmest parts of of the planet (known as the amplitude) can be calculated to determine the day-night ratio of the planet. Additionally, phase curves reveal the subobserver longitude for the brightest integrated hemisphere of the planet, known as the hotspot offset. Both of these observables can then be compared to atmospheric models.

I show an example phase curve of the hot Jupiter HD 189733b in Figure 1.3. From this observation, multiple pieces of information can be learned about this planet. For instance, this planet has a slight eastward shifted hotspot—denoted by the fact that the maximum brightness occurs before secondary eclipse. Additionally, the figure shows a minimum and maximum flux—indicative of a day-night temperature gradient. If the planet was uniform in temperature, the phase curve would be a flat line that dips only for primary and secondary eclipse, when the planet or starlight is physically blocked.

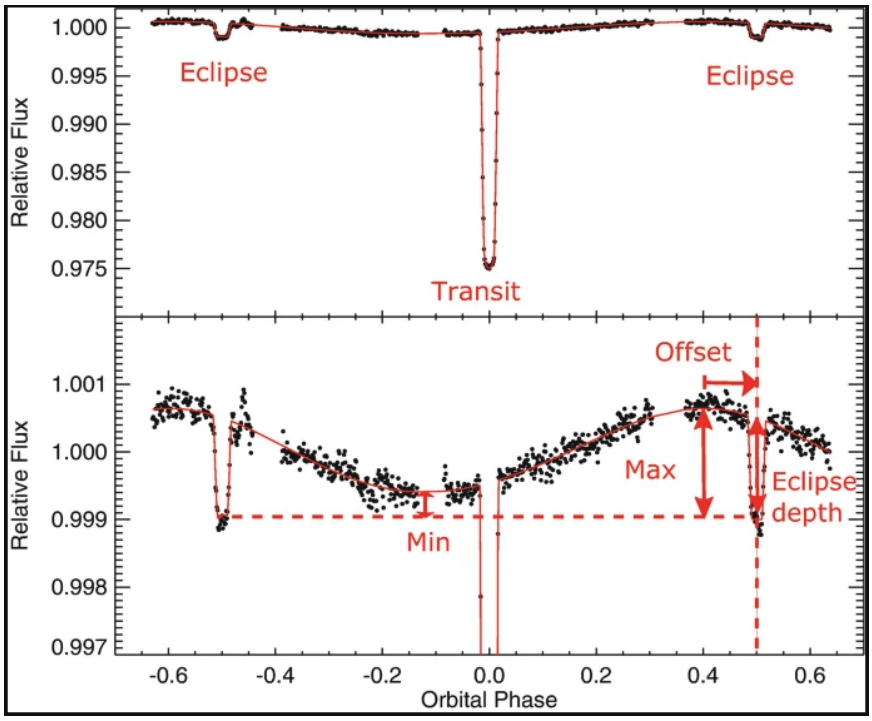

Figure 1.3 *Spitzer* 3.6μm phase curve of the hot Jupiter HD 189733b with important features highlighted. Annotations are done by *Parmentier and Crossfield* (2018) on the original phase curve published by *Knutson et al.* (2012).

1.2.2 High Resolution Spectroscopy

High Resolution Spectroscopy (HRS) ($R \gtrsim 30,000$) is a relatively recent observational technique that allows for more unambiguous detection of molecules in exoplanet atmospheres than ever before. At its core, HRS takes advantage of the sheer number of lines that can be resolved as the resolution increases, as shown in Figure 1.4. This figure shows a model of CO absorption at differing resolutions. While the lowest resolution black line (corresponding to *HST*'s specifications) only gets a single data point in this wavelength range, the highest resolution spectra contains hundreds. Since $SNR \sim \sqrt{\text{Number of Lines}}$ (*Birkby*, 2018), molecules that were previously too faint to detect in lower resolution are now accessible by combining hundreds or even thousands of lines. HRS also takes advantage of the fact that the relative motion of the planet is greater than that of the host star from our perspective. This relative motion

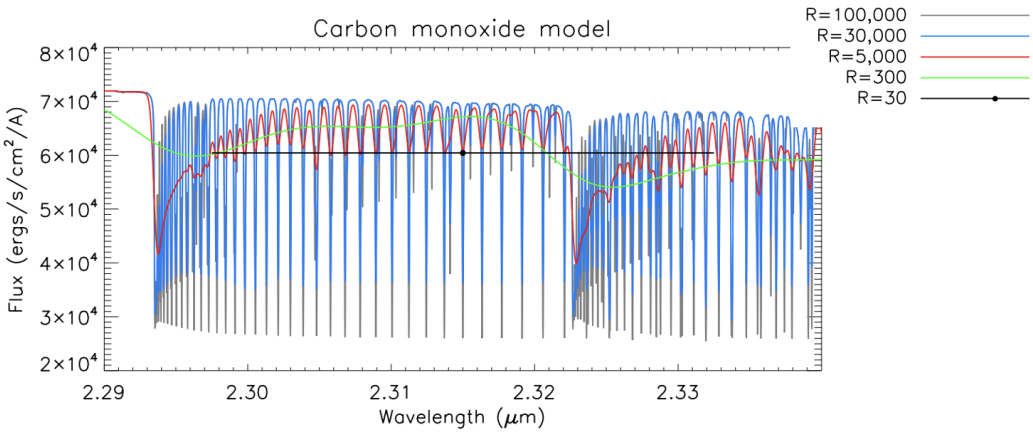

Figure 1.4 Carbon Monoxide absorption lines at a variety of different resolutions. One can see that as the resolution increases, so does the number of lines. Figure adapted from *Birkby* (2018).

is also time-varying, which allows the planet signal to be separated from the host star and telluric signals, which tend to not shift in wavelength with time.

1.2.2.1 Cross-Correlation

Cross-correlation is a simple, but powerful statistical technique to determine how similar two functions or signals are. First, one of two functions is artificially shifted or lagged behind the other one.[5] Assuming $f(n)$ and $g(n)$ are our two functions, at the lagged location s, a cross-correlation coefficient can be calculated via:

$$C(s) = \frac{R(s)}{\sqrt{s_f^2 * s_g^2}} \tag{1.1}$$

where

$$R(s) = \frac{1}{N} \sum_n f(n) g(n-s) \tag{1.2}$$

and s_f^2 and s_g^2 are the variances of the two functions (*Brogi and Line*, 2019). The more similar the two functions are, the larger the cross-correlation coefficient will be.

[5]In HRS, this corresponds to shifting in velocity space

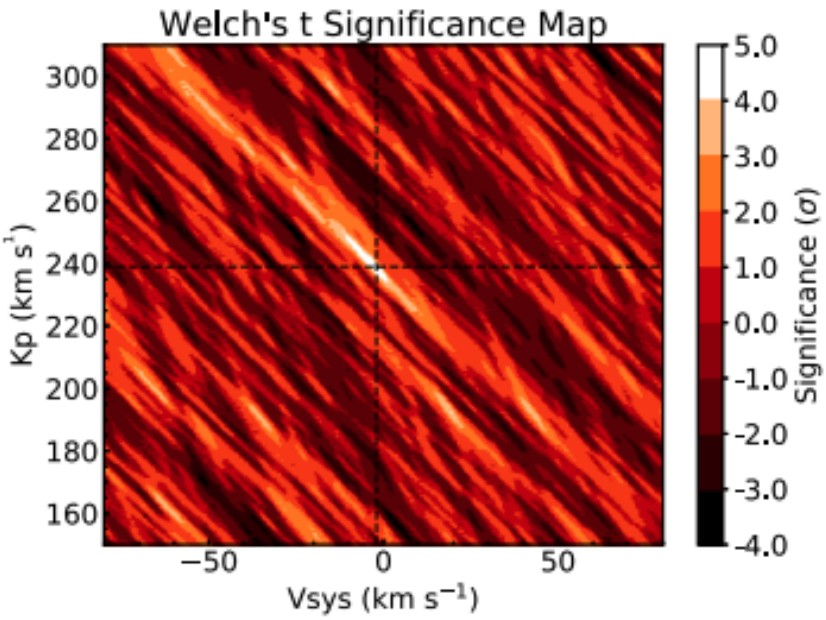

Figure 1.5 An example of a cross-correlation significance map, originally from *Nugroho et al.* (2017). One can see that the region of highest significance is slightly blueshifted from the planet's expected position (denoted by the black dashed lines). This offset is common and often attributed to winds or atmospheric motion.

In HRS, astronomers shift an atmospheric model spectrum to a variety of different velocities and calculate the cross correlation coefficient at each of these velocities. One can then convert these coefficients to detection significances using methods such as the log-likelihood approach (*Brogi and Line*, 2019) or Welch's t test (*Nugroho et al.*, 2017) to assess the detection strength of the molecule for the atmospheric model used.

In Figure 1.5, I show an example of detection of TiO from *Nugroho et al.* (2017). As is common in HRS, the peak detection is slightly offset from the "expected" planet location indicated by the black dashed line. This offset is likely due to atmospheric motion. In addition to the detection, one can see that the surrounding parameter space investigated is rather noisy; there are regions where the signal reaches up to 3 σ, despite being very far away from the expected position of the planet. This is a consequence of the cross-correlation technique and often detections $\lesssim 5\sigma$ are labeled as tentative for this reason.

1.2.2.2 Emission Spectra

In HRS emission spectroscopy, astronomers measure the thermal emission from the planet. However, there are two other major sources that drastically impact the data that must be removed—Earth's pesky telluric lines and stellar contamination from the host star. Compared to the exoplanet's spectrum however, both of these contaminants are roughly uniform with time. Thus, by removing time independent components from a dataset, one is left with two time-dependent sources: the exoplanet's spectrum and noise. At this point, the exoplanet signal is not visible by eye—which is one of the differences between high and low resolution analysis—as the planet spectrum and noise are roughly the same order of magnitude (*Birkby*, 2018). In order to learn about the planet, an atmospheric template is now needed for cross correlation.

The emission spectra of a planet will be influenced by the planet's temperature structure, large scale Doppler shifting from winds and rotation, and compositional makeup. Emission spectra are mostly composed of the light leaving the planet's photosphere, which can differ significantly in pressure from planet to planet. (Stronger lines originating from smaller pressures and weaker lines from higher pressures are still present, however.) The planet's photospheric pressure level is largely influenced by the gravity of the planet, with higher gravity planets having their photospheres deeper in their atmospheres.

The first use of HRS in emission used data from *CRIRES* (*Kaeufl et al.*, 2004) where *Brogi et al.* (2012) looked at the dayside emission of τ Boo b, detecting CO. Importantly, this is a *non-transiting* planet, showing that this technique can be used for a large parameter space of orbital configurations.

1.2.2.3 Transmission Spectra

Transmission spectra, unsurprisingly, can only be observed from planets that are transiting from our point of view. This cosmic lottery is not completely out of our

control though. Planets that are larger are easier to measure and planets on shorter orbital periods are more likely to transit, making hot and ultrahot Jupiters excellent targets for transmsission analysis. An important difference between this technique and emission spectroscopy is in the quantities being measured. While emission measured the light radiated by the planet, with transmission spectra we are measuring the *absorption* of light through the planet's atmosphere. Therefore, considerations of the host star effects are more important here than for the emission technique.

Similar to HRS emission spectra, high-resolution transmission spectroscopy strategically uses the planet's motion to help separate the signal from the background. Often, this is accomplished via data reduction techniques, such as principle component analysis (PCA) (e.g. *de Kok et al.*, 2013; *Piskorz et al.*, 2016). This method uses linear algebra to find the dominant signals in the data such as Earth's telluric, stellar lines, and air mass effects. These components are removed one at a time to optimize the final detection strength and can be used in high-resolution emission spectroscopy as well.

High resolution spectroscopy saw its first ever successful use with *Snellen et al.* (2010) who detected CO in the atmosphere of HD 209458b with *CRIRES* (*Kaeufl et al.*, 2004) transmission data. The molecule CO was strongly detected. However, notably the peak detection was found at a blueshift $2 \pm 1 kms^{-1}$ away from the expected location. This additional blueshift was attributed to the strong winds on the planet and showed the range of capabilities for HRS.

1.3 General Circulation Models (GCMs)

The main theoretical tool used throughout this dissertation is a numerical model known as a General Circulation Model (GCM). This type of numerical simulation solves a set of equations known as "the primitive equations of meteorology" in the frame of reference of the planet. These equations describe the energy balance neces-

sary at a constant pressure level. The horizontal momentum equation is:

$$\frac{d\mathbf{v}}{dt} = -\nabla\Phi - f\mathbf{k} \times \mathbf{v} + D_{\mathbf{v}} \tag{1.3}$$

where $\mathbf{v}$ is the horizontal velocity, $\Phi = gz$ is the geopotential, f is the Coriolis parameter ($2\Omega\sin(\phi)$) where Ω is the planet's rotation rate and ϕ is the latitude. Additionally, $\mathbf{k}$ is the vertical unit vector and $D_{\mathbf{v}}$ representing drag/friction. The vertical momentum is expressed as:

$$\frac{d\Phi}{dP} = -\frac{1}{\rho} \tag{1.4}$$

where ρ represents density. With $\omega = \frac{dP}{dt}$ representing the vertical velocity in pressure coordinates, the continuity equation can be expressed via

$$\nabla \times \mathbf{v} + \frac{d\omega}{dP} = 0 \tag{1.5}$$

which is essentially a conservation of mass. Finally, the thermodynamic energy equation is

$$\frac{dT}{dt} = \frac{q}{c_p} + \frac{\omega}{\rho c_p} + D_T \tag{1.6}$$

where q is the radiative heating rate and c_p is the specific heat (*Wallace and Hobbs*, 2006; *Showman et al.*, 2009).

By allowing these equations to operate on an initial atmospheric structure for enough timesteps, GCMs are able to simulate temperature and wind fields for planetary atmospheres.

In addition to the primitive equations of meteorology, GCMs must also facilitate heating and cooling resulting from radiation. The most basic method for this is Newtonian relaxation, which forces the temperature structure to a pre-determined profile. At higher complexity, radiative transfer prescriptions are used. The GCMs presented

in this dissertation use a double-gray radiative transfer (*Roman and Rauscher*, 2017) routine, but more sophisticated treatments such as correlated-k or picket fence can be found as well, each of which influences the final atmospheric profile in distinct ways (*Lee et al.*, 2021).

On top of this, many GCMs have additional routines for physics such as clouds, magnetic effects, or molecular dissociation, to name a few. Because of this, different GCMs have their own strengths and weaknesses which should be considered before modeling a planet. Of course, no single GCM contains all possible physical processes in exoplanet atmospheres, as that would be computationally infeasible, but also unnecessary since the relative importance of physical processes varies depending on the characteristics of the planet being modeled.

1.3.1 Large Scale Hot and Ultrahot Jupiter Atmospheric Dynamics

There are no hot Jupiter analogues in our solar system and their strong irradiation regime results in unique atmospheric structures. The atmospheric circulation of hot and ultrahot Jupiters is driven to first order by the fact that these planets are expected to be in tidally synchronous orbits (*Rasio et al.*, 1996). This results in a permanent dayside which always faces the host star and a permanent nightside which never becomes irradiated. These planets are thus characterized by strong day-night temperature gradients and therefore vary strongly as a function of longitude. This highlights the importance of using a 3D model, as these effects are inherently multidimensional.

The radiative forcing from the close host star combined with the rotation of the planet results in strong transonic winds throughout the planet atmosphere as a heat redistribution mechanism (*Tan and Komacek*, 2019; *Showman et al.*, 2020). In particular, a superrotating equatorial jet forms (*Showman et al.*, 2010; *Rauscher and Menou*, 2010) which extends deep into the planet's atmosphere. This jet shapes the

global dynamics of the planet and often advects the hottest spot on the planet east of the substellar point. These features robustly appear across multiple atmospheric models (e.g. *Rauscher and Menou*, 2012; *Heng et al.*, 2011; *Mayne et al.*, 2014; *Dobbs-Dixon and Agol*, 2013; *Deitrick et al.*, 2020, to name a few) and have been confirmed through observations (*Knutson et al.*, 2012; *Zellem et al.*, 2014; *May et al.*, 2022).

1.3.1.1 How do HJs and UHJs Atmospheres Differ?

In this dissertation , Chapter II focuses on a canonical hot Jupiter, while Chapters III, IV and V focus on a canonical ultrahot Jupiter. Up until this point, I have been grouping together HJs and UHJs, but important differences exist between the two categories. Specifically, the higher temperature of UHJs leads to different levels of influence from physical processes. One example of this is molecular hydrogen dissociation. On the dayside of UHJs H_2 is dissociated, a reaction that cools the surrounding area (as energy is needed to dissociate the molecule). Once the hydrogen is blown by the strong winds to the nightside, the temperature is cool enough for recombination to occur, releasing heat and warming the nightside (*Bell and Cowan*, 2018). This process thus reduces the day-night temperature gradient of the planet. The hotter temperatures of UHJs also result in increased ionization of atmospheric species (*Parmentier et al.*, 2018) which can lead to stronger atmospheric magnetic effects (*Perna et al.*, 2010a). I will go into more detail of magnetic effects in UHJ atmospheres in Section 1.3.3.

UHJs are also more likely to exhibit temperature inversions in their atmospheres—regions where increasing in altitude corresponds to increasing temperatures. This behavior is important because thermal emission spectra from these regions will result in emission features as opposed to absorption features. Chapter IV explores the affect of temperature inversions on high resolution emission spectra extensively. The physical reason for these inversions are still debated, but the most well-accepted

theories include absorption of H^- opacity (*Tan and Komacek*, 2019), inefficient heat transfer from day to nightside (*Heng and Showman*, 2015), high altitude optical or UV absorbing species (*Hubeny et al.*, 2003; *Fortney et al.*, 2008), or high C/O ratios (*Mollière et al.*, 2015). These inversions are restricted to the dayside of the planet and evidence suggests the strength of the inversion may scale with the stellar type of the host star (*Baxter et al.*, 2020).

Also due to their higher temperatures, certain physical processes are muted or negligible for UHJs that play important roles for HJs. Perhaps the most significant of these are clouds and aerosols. *Roman et al.* (2021) explored cloud coverage for various irradiation temperatures spanning both the HJ and UHJ regime. For UHJs, clouds were non-existent on the dayside and would likely be constrained to nightside upper latitudes, if present at all. HJs on the other hand can have clouds throughout nearly the entire atmosphere, which can influence observations (*Harada et al.*, 2021). These clouds initiate feedback with the temperature structure by either heating or cooling the atmosphere, depending on the cloud extent and local conditions. Clouds and hazes at high altitudes are often cited as the main cause of flat, featureless transmission spectra (*Kreidberg et al.*, 2014). Through extensive modeling, *Helling et al.* (2020) found that hydrocarbon hazes should play nearly no role in UHJ atmospheres, but can influence cloud formation and overall C/O ratios. In this dissertation, due to its large focus on UHJs and magnetic effects, there will be no cloud models presented.

1.3.2 The Issue of Inflated Radii

One current tension with observational data is that many hot and ultrahot Jupiters have larger radii than predicted from interior evolutionary models (*Baraffe et al.*, 2010). There is reason to believe that stellar irradiation plays a role in this inflation, but additional factors must be at play, as shown in Figure 1.6. From this figure, it is apparent that there are more inflated planets at higher equilibrium temperatures,

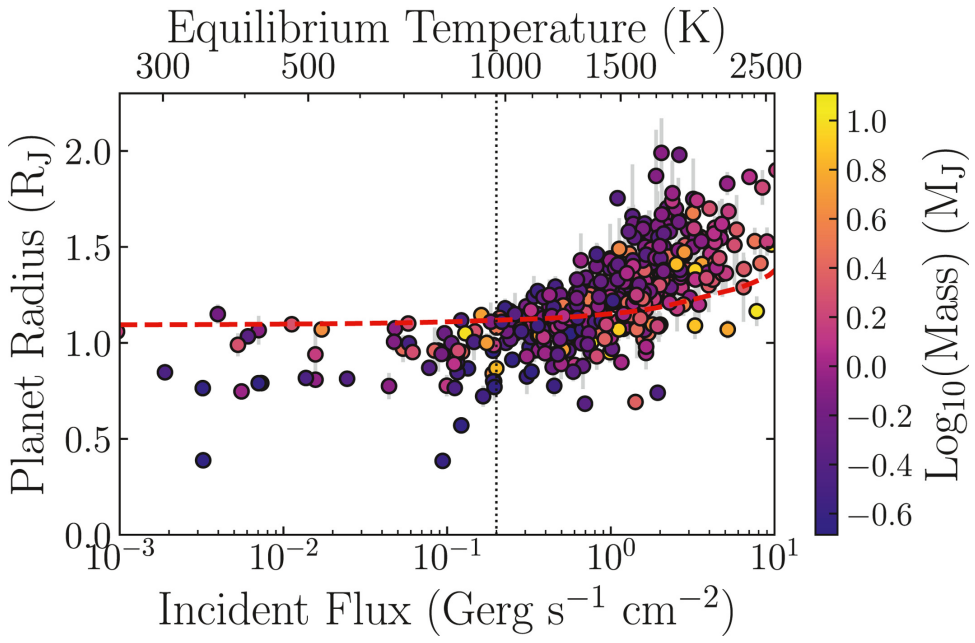

Figure 1.6 Observed radii of gas giant exoplanets as a function of incident flux. The red dashed line represents the radius of a Jupiter-sized planet with a H/He atmosphere without any inflation mechanisms. This can be considered an approximate upper limit for non-inflated planets, so planets above this line are likely inflated. Figure from *Fortney et al.* (2021), updated from *Thorngren and Fortney* (2018).

however not every planet at high equilibrium temperatures is inflated. In addition, planets receiving the same amount of incident flux can be different degrees of inflated, hinting that other mechanisms must be at play.

Some mechanism (or a combination of many) must be involved that regularly deposits energy deep into the planet's interior, otherwise one would expect the planet to deflate (*Heng and Showman*, 2015). There are many suggested mechanisms for this inflation, including inefficient internal cooling, tidal dissipation, vertical mixing and Ohmic dissipation, to name a few (*Fortney et al.*, 2021).

For this dissertation, I will limit the discussion to Ohmic dissipation, as it is the most relevant to the other themes explored. First suggested by *Batygin and Stevenson* (2010) and *Perna et al.* (2010b), Ohmic dissipation is a natural consequence of the planet's magnetic field interacting with the strong winds containing ions. In our solar system, a majority of the planets have some sort of magnetic field. We thus expect

that exoplanets should have magnetic fields as well, but have yet to directly detect a magnetic field in a planet outside our solar system. Scaling laws predict that hot Jupiters or ultrahot Jupiters should be able to host fields of the same size if not larger than those found in our solar system (*Christensen et al.*, 2009; *Yadav and Thorngren*, 2017).

Due to the temperatures of UHJs, many species will become thermally ionized. As these ions are blown around the planet, they will create an electrical current, which will eventually be dissipated, depositing energy. If this energy is large enough and deposited deep enough in the atmosphere, this could fuel radius inflation (*Batygin and Stevenson*, 2010). *Thorngren and Fortney* (2018) suggests Ohmic dissipation could be the main mechanism of giant planet inflation. However, work from *Wu and Lithwick* (2011) and *Ginzburg and Sari* (2015) suggest that this mechanism alone is not enough to fully explain the inflated radius problem.

1.3.3 Magnetic Treatments in GCMs

Most GCMs have no dedicated routines or treatments for magnetic effects. However, many GCMs apply a "catch-all" uniform drag to encompass these effects as well as other dissipation and drag sources. I discuss below why this approximation is particularly bad for UHJs. Our method of applying magnetic drag in a 3D atmosphere is only topped in physical realism by specialized non-ideal MHD models. Due to their computational complexity, very few of these models have been run for UHJs or HJs. These types of models treat magnetic effects with fewer simplifying assumptions, but at the cost of reducing complexity in the radiative transfer, limited ranges in magnetic resistivity, and underestimation of wind speeds due to treatments of viscosity (*Rogers and Showman*, 2014; *Rogers and Komacek*, 2014; *Rogers*, 2017; *Hindle et al.*, 2019).

1.3.3.1 The Uniform Drag Approach

Many GCMs (*Komacek and Showman*, 2016; *Kreidberg et al.*, 2018; *Arcangeli et al.*, 2019, for example) apply a Rayleigh drag term with a uniform drag timescale to their horizontal and vertical momentum equations to mimic the effects of Lorentz forces and/or other dynamical effects. This mainly results in increased day-night temperature gradients, smaller hotspot offsets, and decreased wind speeds. To first order, these outcomes are also found when we apply our more complex active magnetic drag. However, the uniform drag method has problematic implications when applied to two regions differing strongly in temperature on the same planet. Based on local conditions, one can roughly approximate the magnetic field needed to produce such a particular drag timescale (*Kreidberg et al.*, 2018). For example, in Chapter III, I calculate a GCM for the UHJ WASP-76b with a uniform drag timescale of 10^4 s, a timescale considered representative of "strong" drag. At a pressure $\sim$ 0.1 bar, the dayside equator can reach temperatures of 2500K. In order to generate drag at a strength corresponding to this timescale at this temperature, the planet's global magnetic field strength would need to be $\sim$6 Gauss, which is reasonable. However, on the nightside, the equator can reach as low as 1500K. Because at this lower temperature the magnetic resistivity is orders of magnitude smaller, the resulting field strength necessary create this amount of drag on the nightside is 300 G. This is clearly an issue, as the global magnetic field strength should not be multiple orders magnitude larger on the nightside where we expect *weaker* magnetic effects. By allowing our drag timescale to vary locally, we are able to avoid this pitfall with our active drag treatment described below.

1.3.3.2 Our approach: Kinematic MHD/ Active Drag

Instead of applying a uniform drag, we represent magnetic effects via a Kinematic MHD/Active Drag approach, first proposed in *Perna et al.* (2010a). Due to its length,

I will not reproduce the entire derivation here. Instead, I will outline the logic and note important approximations. By beginning with the non-ideal MHD induction equation, *Perna et al.* (2010a) makes order of magnitude estimates of each term based on quantities relevant to a hot Jupiter atmosphere. From this several terms become negligible and thus so long as the magnetic Reynolds number, R_m (to be defined shortly) is less than one, the atmosphere can be treated as operating in the purely resistive regime. From this, the paper uses the resistive induction equation and cleverly derives a timescale based on the Lorentz force felt by the ions. This timescale is as follows:

$$\tau_{mag}(B, \rho, T, \phi) = \frac{4\pi\rho\ \eta(\rho, T)}{B^2|sin(\phi)|} \tag{1.7}$$

where B is the chosen global magnetic field strength, ϕ is the latitude, ρ is the density. η represents magnetic resistivity,

$$\eta = 230\sqrt{T}/x_e \text{ cm}^2 \text{ s}^{-1}. \tag{1.8}$$

where ionization fraction, x_e, can be calculated using the Saha equation.

Perhaps the main advantage of this timescale is the ability to apply widely different amounts of drag to different parts of of the atmosphere. Figure 1.7 (which first appeared in *Rauscher and Menou*, 2013), shows the log of calculated drag timescale (in seconds) under different density and pressure conditions reasonable for a hot Jupiter atmosphere. One can see the large range in timescale lengths under these different conditions. Compared to the uniform drag approach, this allows for a more physically-consistent way of applying magnetic effects.

As with any approximation, it is important to understand its assumptions and limitations to ensure that it is used correctly. Perhaps the most important for the kinematic MHD approach is the assumption that the magnetic field is aligned with the planet's axis of rotation. This is a simplifying assumption, which results in the active

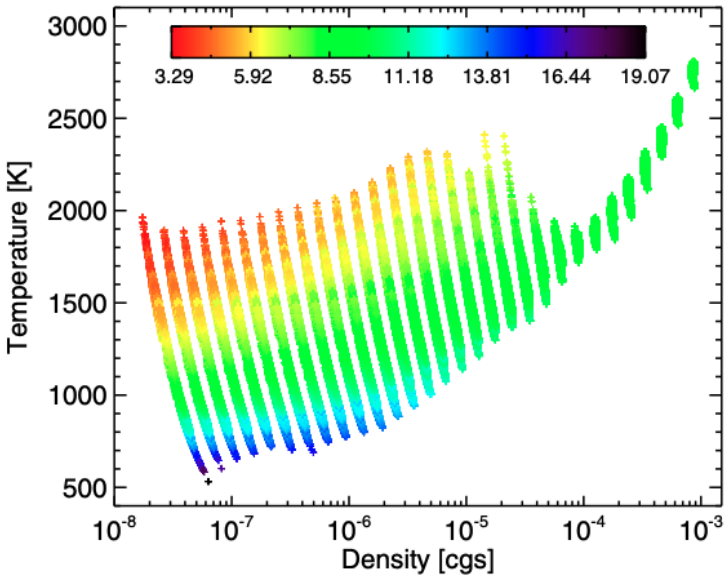

Figure 1.7 Active Drag timescales calculated for different temperatures and densities. The log of the timescale in seconds is denoted by the color of each point. Our active drag timescale can vary many orders of magnitude for a single planet, allowing for a more sophisticated drag approach than uniform. Figure originally from *Rauscher and Menou* (2013)

drag being applied only in the east-west direction, as that is the only direction where the ions would be crossing magnetic field lines perpendicularly. This is currently a limitation of the routine, as we see tilted magnetic fields in our solar system [6]. However, given the field's lack of unambiguous detection on any exoplanet magnetic field, let alone a degree of tilt, this approximation is reasonable for the state of the field.

The other important consideration for this prescription is that the magnetic Reynolds number, R_{mag}, is low. This value can be expressed as (*Hindle et al.*, 2021b)

$$R_{mag} = \frac{UH}{\eta} \tag{1.9}$$

where U represents the east-west wind speed and H being the atmospheric scale height. Based on the derivation outlined in (*Perna et al.*, 2010a), the active magnetic

[6]The author has lofty dreams of including tilted magnetic fields in this GCM once she finishes her dissertation

drag scheme is valid for $R_{mag} < 1$. I show the Magnetic Reynolds numbers for our models in Chapter III. For a majority of atmospheres of the models presented in this dissertation, the condition of $R_{mag} < 1$ is easily met. Regions in the dayside upper atmosphere of some UHJ models approach this limit, and therefore these regions should be interpreted with appropriate caution.

1.4 Dissertation Overview

Chapter II explores the first use of a 3D GCM as an atmospheric template for high resolution emission spectroscopy of a hot Jupiter, showing for the first time in HRS emission spectroscopy, 3D models can out-preform a suite of 1D models. This paper also explores the effect of differing rotation rates on the resulting emission spectra. This work has been published in the Astrophysical Journal.

Chapter III explores the effect of our active magnetic drag on the atmospheric structure of the ultrahot Jupiter WASP-76b. I look at the change in circulation regime as a result of this active drag and explore its effects on bolometric phase curves. Chapter IV explores the effect of magnetic drag on high resolution emission spectra and V explores its effect on high resolution transmission spectra. This latter set of three papers provide a roadmap for understanding how magnetic effects can shape the atmospheres and observables of ultrahot Jupiters and have all been published in the Astrophysical Journal. Finally, in Chapter VI, I pontificate upon the state of the field, how my research fits into the emerging picture of exoplanets and predictions for the future.

CHAPTER II

A Significant Increase in Detection of High-resolution Emission Spectra Using a Three-dimensional Atmospheric Model of a Hot Jupiter (Beltz et al 2021)

'Yeah!!! Yeah!!!!!!!!!!!!!! Im Doing it!!! Im experiencing 3d"

– Culture Icon, @Dril

2.1 Preface

Results in this chapter were published in: *Beltz, H., Rauscher, E., Brogi, M., and Kempton, E., 2021. A Significant Increase in Detection of High-resolution Emission Spectra Using a Three-dimensional Atmospheric Model of a Hot Jupiter. The Astronomical Journal, 161, 1* and are reproduced here with minor style revisions by permission of the American Astronomical Society under the non-exclusive right of republication granted to authors.

2.2 Abstract

High resolution spectroscopy has opened the way for new, detailed study of exoplanet atmospheres. There is evidence that this technique can be sensitive to the complex, three-dimensional (3D) atmospheric structure of these planets. In this work, we perform cross correlation analysis on high resolution ($R \sim 100,000$) CRIRES/VLT emission spectra of the Hot Jupiter HD 209458b. We generate template emission spectra from a 3D atmospheric circulation model of the planet, accounting for temperature structure and atmospheric motions—winds and planetary rotation—missed by spectra calculated from one-dimensional models. In this first-of-its-kind analysis, we find that using template spectra generated from a 3D model produces a more significant detection (6.9 σ) of the planet's signal than any of the hundreds of one-dimensional models we tested (maximum of 5.1σ). We recover the planet's thermal emission, its orbital motion, and the presence of CO in its atmosphere at high significance. Additionally, we analyzed the relative influences of 3D temperature and chemical structures in this improved detection, including the contributions from CO and H_2O, as well as the role of atmospheric Doppler signatures from winds and rotation. This work shows that the Hot Jupiter's 3D atmospheric structure has a first-order influence on its emission spectra at high resolution and motivates the use of multi-dimensional atmospheric models in high-resolution spectral analysis.

2.3 Introduction

High Resolution Spectroscopy (HRS) is a relatively recent, powerful method for exoplanet atmospheric characterization. It uses a spectral resolution high enough ($R \gtrsim 30,000$) to unambiguously detect the unique sets of spectral lines from atoms or molecules in an exoplanet's spectrum. While the planet's spectrum is often orders of magnitude weaker than the stellar noise, its signal can be detected via cross-

correlation with a template spectrum due to the increased number of lines present at high resolution. This is accomplished by exploiting the planet's changing orbital radial velocity along the observers line of sight which helps to remove the stellar and telluric signals, whose spectral features remain effectively at fixed wavelengths over the duration of a typical observation. By removing the components of spectrum that are constant with time, one is left with noise and the planet spectrum, which can then be detected via cross-correlation. *Birkby* (2018) presents a review of the HRS method and recent results from its use.

HRS was first applied to the well-known hot Jupiter HD 209458b using the CRIRES instrument on the VLT (*Snellen et al.*, 2010), definitively detecting CO in transmission spectra from the planet. Further analysis of the transmission spectra of this planet at high resolution have resulted in detections of water vapor (*Sánchez-López, A. et al.*, 2019) and helium (*Alonso-Floriano, F. J. et al.*, 2019). Emission spectra of this planet have also been measured with HRS, providing evidence against an atmospheric temperature inversion (*Schwarz et al.*, 2015), as well as determining both carbon monoxide and water abundances when combined with lower resolution data (*Brogi et al.*, 2017; *Gandhi et al.*, 2019). In this paper we present a re-analysis of the previously published CRIRES/VLT data for this planet (*Schwarz et al.*, 2015), but with template spectra generated from a three-dimensional atmospheric model.

One of the unique strengths of HRS is that at the highest resolutions ($R \sim 100,000$) the observed spectra can contain information about the *atmospheric* motion of the planet. The original HRS result by *Snellen et al.* (2010) found hints of day-to-night winds on the planet in a net blue-shift of the planet's spectrum by 2 ± 1 km s^{-1} (during transit, day-to-night winds blow toward the observer). Transmission spectra of the hot Jupiter HD 189733b also show evidence for atmospheric motion, including both net Doppler shifts from winds and Doppler broadening from a combination of rotation and eastward equatorial winds (*Louden and Wheatley*, 2015; *Brogi et al.*,

2016; *Flowers et al.*, 2019). Measured Doppler broadening in high-resolution emission spectra of directly imaged planets/companions have also been used to constrain the rotation rates of these objects (*Snellen et al.*, 2014; *Schwarz et al.*, 2016; *Bryan et al.*, 2020).

The two sources of atmospheric motion—winds and rotation—are not physically independent.For a recent review of hot Jupiter dynamics, see *Showman et al.* (2020). One of the governing forces in determining atmospheric circulation is the Coriolis force, meaning that the rotation rate of a planet strongly influences the wind structure and speeds. Hot Jupiters are commonly assumed to be tidally locked into rotation rates synchronous with their orbits (e.g., *Rasio et al.*, 1996), but deviations from this expected rotation state would have consequences for the speed and structure of atmospheric winds (*Showman et al.*, 2009), which then influences the expected Doppler shifts and broadening in HRS data (*Rauscher and Kempton*, 2014). It is an ongoing debate within the community as to how tidal forces interact with the complex structure of hot Jupiters and whether we should assume them to be synchronized or not (*Gu and Ogilvie*, 2009; *Arras and Socrates*, 2010; *Auclair-Desrotour and Leconte*, 2018; *Lee*, 2020; *Yu*, 2020).

Given the exquisite spectral detail measurable by HRS, including constraints on atmospheric motions, we may wonder how sensitive it is to the full three-dimensional nature of the planet; and what degree of bias will a one dimensional model introduce. Another way to state this is whether or not one-dimensional atmospheric models are sufficient to accurately interpret HRS data. Especially for hot Jupiters, where we expect hundreds of Kelvin temperature contrasts across the globe (*Rauscher and Menou*, 2012; *Dobbs-Dixon and Agol*, 2013; *Kataria et al.*, 2016; *Parmentier et al.*, 2018; *Deitrick et al.*, 2020; *Drummond et al.*, 2020) , differences in the local atmospheric structure can result in limb- or disk-integrated transmission or emission spectra (respectively) that are significantly different from a spectrum calculated us-

ing a 1-D model. Several studies have considered how the 3-D nature of a planet can influence lower resolution spectra (e.g., *Fortney et al.*, 2006, 2010; *Burrows et al.*, 2010) and, in particular, ways that the use of 1-D models could bias our interpretation of spectral data (e.g., *Feng et al.*, 2016; *Blecic et al.*, 2017; *Caldas et al.*, 2019b; *Pluriel et al.*, 2020). For HRS data, several studies have simulated high-resolution spectra from different 3-D models, both in transmission (*Miller-Ricci Kempton and Rauscher*, 2012; *Showman et al.*, 2013; *Kempton et al.*, 2014; *Rauscher and Kempton*, 2014) and emission (*Zhang et al.*, 2017; *Harada et al.*, 2019), demonstrating that the complex atmospheric structures of hot Jupiters can influence HRS data.

Flowers et al. (2019) presented a first-of-its-kind analysis of HRS data, using simulated transmission spectra from 3-D models as template spectra in the cross-correlation analysis of observations of the hot Jupiter HD 189733b. Not only was the planet's signal detected at high significance (supporting the validity of the 3-D models), but this work also consistently detected the Doppler signature of day-to-night winds on this planet. When the Doppler effects from the winds were artificially excluded from the calculation of the template spectra, the planet's signal was detected with an anomalous blue-shift; when the effects of the winds were included, the detection was at the expected planet velocity.That is, ignoring the Doppler effects on simulated transmission spectra resulted in incorrect inferred planetary motion, confirming their measurable influence in the observed spectra.

Here we present an analogous study to *Flowers et al.* (2019), but for emission spectra (as opposed to transmission), in which we use simulated spectra from 3-D models in the HRS cross-correlation analysis. In addition to studying a complimentary observational technique—emission instead of transmission—we also target a different bright hot Jupiter than that analysis, namely HD 209458b. HRS transmission spectra can be directly influenced by atmospheric motion, but are only secondarily affected by the three-dimensional temperature structure *Flowers et al.* (2019). We expect that

HRS emission spectra may be much more sensitive to differences in atmospheric thermal structure around the planet, given that any Doppler effects from atmospheric motion will be most sensitive to the brightest regions of the planet (*Zhang et al.*, 2017). In this paper we empirically determine how sensitive HRS emission spectra are to the 3-D nature of a particular planet, as well as to what degree various aspects of the atmospheric structure contribute to the observed data. Specifically, we study the sensitivity of the data to the planet's rotation period by running a suite of 3-D models for a range of rotation rates, producing a set of consistent temperature and wind structures for each case. We also test the sensitivity of the data to atmospheric chemistry by comparing an assumption of well-mixed abundances or local chemical equilibrium values in the radiative transfer routine we use to post-process the 3-D models and create simulated spectra. We also analyze the relative contributions of the two main opacity sources over the wavelengths of observation (2.285 to 2.348 μm): carbon monoxide and water. Finally, we test the sensitivity of the data to Doppler effects from atmospheric motions by cross-correlating with simulated spectra calculated with and without those effects.

In Section 2.4, we explain the various numerical methods used in this work: the three-dimensional atmospheric model and the radiative transfer routine used to post-process the 3-D models and calculate simulated emission spectra. Additionally, we briefly describe the results of these standard hot Jupiter models. In Section 2.5 we describe the observational data, along with details of our reduction and analysis methods. In Section 2.6 we present the results of our cross-correlation analysis, comparing the strength of planetary signal detected when using template spectra from 1-D or 3-D models, and comparing the aforementioned assumptions regarding chemistry, opacity sources, Doppler effects, and rotation rates. In Section 2.7 we summarize our main results.

2.4 Numerical Models: 3D GCMs and Simulated Emission Spectra

In order to create simulated high-resolution emission spectra for HD 209458b, we first use a General Circulation Model to predict the three-dimensional atmospheric structure of the planet—that is, thermal and wind structure— and then post-process the results using a detailed radiative transfer routine that accounts for the correct geometry and atmospheric Doppler shifts. These modeling methods and results are not particularly novel, having formed the basis of previous papers (*Miller-Ricci Kempton and Rauscher*, 2012; *Rauscher and Menou*, 2012; *Rauscher and Kempton*, 2014; *Roman and Rauscher*, 2017; *Zhang et al.*, 2017); however, our suite of models for this particular planet have not been published previously and so we briefly describe the results in order to set the stage for the comparison between the simulated emission spectra and observed data.

2.4.1 General Circulation Model

General Circulation Models (GCMs) are three-dimensional computational atmospheric models that simulate the underlying physics and circulation patterns of planetary atmospheres. For this work, we utilized the GCM from *Rauscher and Menou* (2012) with the radiative transfer scheme upgraded as described in *Roman and Rauscher* (2017). This model solves the primitive equations of meteorology: the standard set of fluid dynamics equations with simplifying assumptions appropriate for the atmospheric context, solved in the rotating frame of the planet (see an early review by *Showman et al.*, 2010). The radiative heating and cooling of the atmospheric uses a double-gray scheme. That is, radiation is treated with two different absorption coefficients under two regimes; an infrared coefficient to model the thermal interaction of the gas with radiation and an optical coefficient to model the absorption

of incoming starlight. For a more detailed explanation of the GCM, see *Rauscher and Menou* (2012) and *Roman and Rauscher* (2017).

We model the hot Jupiter HD 209458b using the parameters listed in Table 4.4.1, with system parameters from *Stassun et al.* (2017), a high internal heat flux appropriate for this inflated hot Jupiter (*Thorngren et al.*, 2019), and absorption coefficients and gas properties set to match our previous models of hot Jupiter atmospheres (e.g., *Rauscher and Menou*, 2012). Typically, we assume that hot Jupiters have been tidally locked into synchronous orbits, meaning that the rotation period and orbital period are equal. In order to empirically test this, we ran the GCM for a total of 12 different rotation rates spanning values faster and slower than synchronous. The slowest rotation rate was chosen to ensure that at least one of the models fell into the disrupted circulation regime for slow rotation previously found in *Rauscher and Kempton* (2014). We then extended our rotation rate sampling (at 0.25 km/s in rotation speed) to comparably cover faster rotation rates. We list the set of chosen rotation periods and their corresponding equatorial rotational velocities in Table 2.4.1, along with some representative wind speeds from each model.

We ran each model at a horizontal spectral resolution of T31, corresponding to a physical scale of $\sim$4 degrees at the equator and with 45 vertical layers evenly spaced in log pressure from 100 bar to 10 microbar. The planets were initialized with a globally averaged temperature-pressure profile and no winds. See *Guillot* (2010) for a derivation of profiles and *Rauscher and Kempton* (2014) for a discussion of the global averaging parameter chosen (set to $f = 0.375$ here). Each simulation was allowed to run for 3000 orbits; by this point the upper atmosphere (including the infrared photosphere) had reached a steady state. *Carone et al.* (2019) recently demonstrated that the treatment of the deep atmosphere in hot Jupiter simulations—in particular the depth of the bottom boundary and the assumed strengths of convective adjustment and frictional/magnetic damping—can influence the circulation results predicted for

Table 2.1. HD 209458b System Parameters

Parameter	Value
Planet radius, R_p	9.9×10^7 m
Gravitational acceleration, g	9.434 m s^{-2}
Orbital Period	3.525 days
Orbital revolution rate, $\omega_{\rm orb}$	2.06318×10^{-5} s^{-1}
Synchronous rotation speed [a]	2.04 km s^{-1}
Substellar irradiation, $F_{\rm irr}$	1.06×10^6 W m^{-2}
Planet internal heat flux, $F_{\rm int}$	3500 W m^{-2}
Optical absorption coefficient, κ_{vis}	4×10^{-3} cm^2 g^{-1}
Infrared absorption coefficient, κ_{IR}	1×10^{-2} cm ^{2} g^{-1}
Specific gas constant, R	3523 J kg^{-1} K^{-1}
Ratio of gas constant to heat capacity, R/c_p	0.286
Stellar radius, R_*	1.19 $M_\odot$
Stellar effective temperature, T_{*eff}	6090 K

[a]In the case of synchronous rotation, this is the corresponding velocity at the equator, calculated as $2\pi R_p/\omega_{orb}$.

the upper, observable atmosphere. Nevertheless, their models of HD 209458b show that this planet exhibits the standard hot Jupiter circulation pattern, in agreement with our results here.

2.4.2 GCM Results

Most of our models display the quintessential features expected for hot Jupiters: a strong eastward equatorial jet which advects the hottest spot on the planet slightly eastward of the substellar point and reduces—but does not eliminate—a large day-to-night temperature contrast of hundreds of Kelvin. We show this temperature structure for the synchronous model in Figure 2.1. The equatorial jet characteristically extends throughout most of the atmosphere; Figure 2.2 shows the zonally averaged winds for the synchronous model. Higher in the atmosphere an additional, significant component of the winds is a substellar-to-antistellar flow pattern; in Figure 2.2 this

Table 2.2. Suite of General Circulation Models

Rotation period (days)	Rotational speed (km/s)	Max. wind speed at IR photosphere (km/s)	Max. wind speed at 0.1 mbar (km/s)
9.08	0.79	2.50	6.28
6.91	1.04	2.64	4.44
5.57	1.29	5.65	6.87
4.67	1.54	5.64	6.76
4.02	1.79	5.61	6.64
3.53	**2.04**	**5.64**	**6.32**
3.14	2.29	5.43	6.19
2.83	2.54	5.47	6.15
2.58	2.79	5.10	5.72
2.37	3.04	4.78	5.56
2.19	3.29	3.77	5.02
2.03	3.54	4.62	5.17

Note. — The bolded values are for the model in a tidally-locked, synchronous rotation state. The rotational speeds are calculated as $2\pi R_p/\omega_{\rm rot}$. Continuum emission comes from the IR photosphere (at $\sim$65 mbar), while the absorption line cores come from pressure regions nearer to 0.1 mbar. Wind speeds are measured in the rotating frame of the planet.

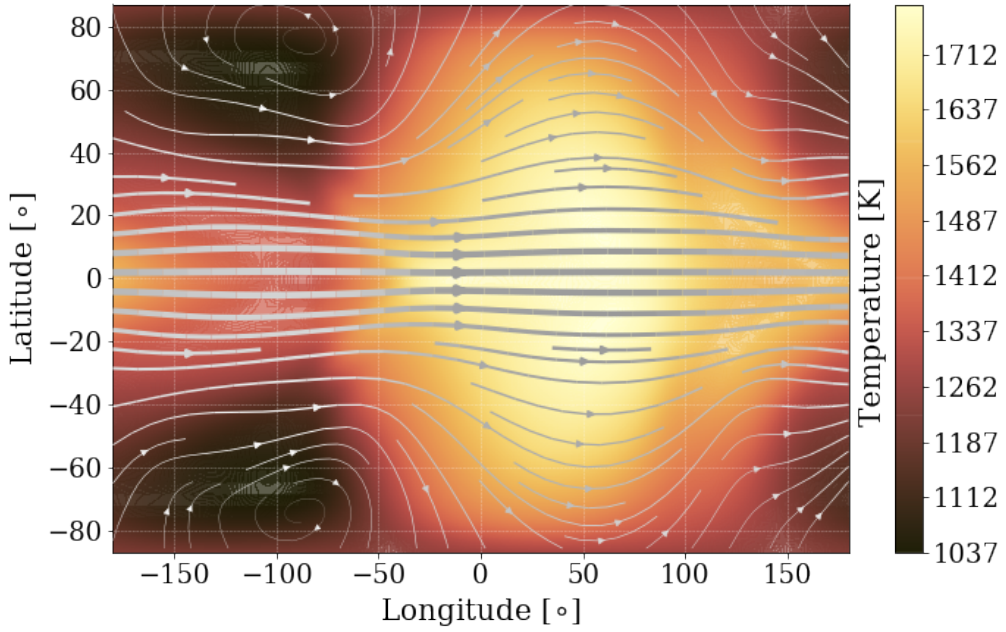

Figure 2.1 The temperature structure near the infrared photosphere ($\sim$ 65 mbar), for our synchronously rotating model of HD 209458b, centered on the substellar point (at 0,0). Streamlines have been overplotted, with thicker lines showing stronger winds. In the eastward direction, the winds reach a speed of 5.6 km/s. The hottest gas has been advected to the east of the substellar point by a strong equatorial jet, in the typical hot Jupiter circulation pattern.

shows up as a decrease in the averaged east-west wind speed.

Figures 2.14 and 2.15 in the Appendix show maps of the temperature and winds at the infrared photosphere for all of the 12 models with different rotation rates. In line with results from previous investigations of non-synchronously rotating hot Jupiters (*Showman et al.*, 2009; *Rauscher and Kempton*, 2014; *Flowers et al.*, 2019), we find that as the rotation rate increases, the stronger Coriolis force causes the equatorial jet to become more narrow and eventually secondary, higher latitude jets form. The wind speeds tend to decrease with increasing rotation rate (see Table 2.4.1), conspiring to create generally similar temperature patterns at the infrared photospheres of each model (Figure 2.14).

The exceptions to these trends are the two most slowly rotating models, whose circulations have been disrupted from the standard hot Jupiter pattern. This disrup-

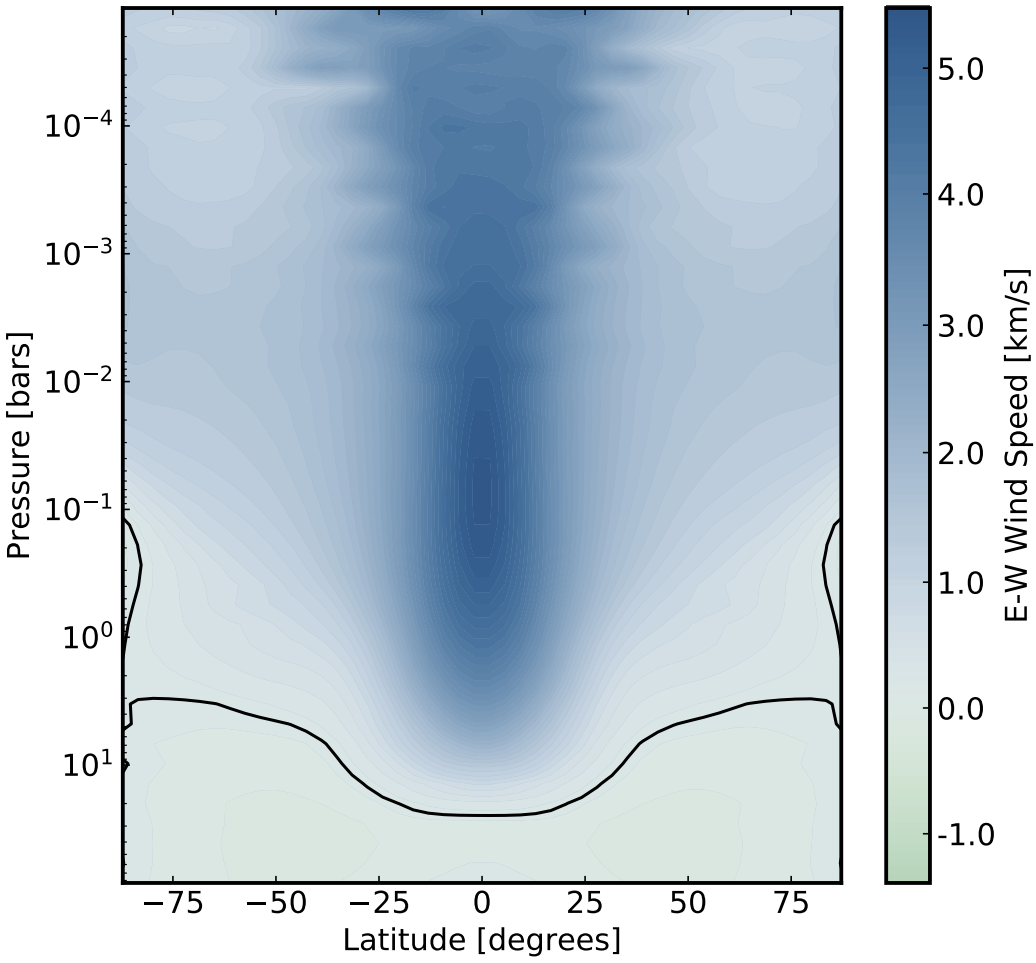

Figure 2.2 Longitudinally averaged east-west wind speeds throughout the atmosphere, for the synchronous rotation case. The eastward equatorial jet (dark blue) extends deep into the atmosphere. The black contour shows the boundary between eastward (positive) and westward (negative) winds.

tion for very slow rotators was first identified by *Rauscher and Kempton* (2014), and the dynamics have been studied by *Penn and Vallis* (2017). For the purpose of this paper, these most slowly rotating models help to provide a lower limit to the possible rotation rate of HD 209458b, as the westward flow and corresponding advection of the hottest region of the atmosphere would result in an orbital phase curve of thermal emission significantly different from what has been previously observed for this planet. In Figure 2.3 we show phase curves of the total thermal emission[1] from each model, calculated throughout one orbit. While most of the models do show similar curves, which peak near the measured phase of maximum flux at 4.5 micron (0.387 ± 0.017; *Zellem et al.*, 2014), the two most slowly rotating models are ruled out by this data as they peak later in phase. Nevertheless, we include these models in the rest of our analysis in order to investigate how they are constrained by HRS data.

Finally, since the CRIRES/VLT emission spectra of HD 209458b are the focus of our paper, we also show the temperature structure and line-of-sight velocities (from both winds and rotation) in the upper atmosphere of the synchronous model in Figure 2.4, shown in an orientation corresponding to the first night of observation. This is the region of the atmosphere from which the flux in the CO line cores emerges, meaning that the detailed structure of those line shapes comes from the brightness-weighted local Doppler shifts, integrated across the visible hemisphere. Since the winds are dominantly eastward, they contribute to the Doppler shifts in the same direction as the rotation field. However, the line-of-sight velocity contours are slightly bent away from being strictly aligned with the rotation axis by the specific atmospheric flow pattern.

The full set of orthographic projections for our suite of 12 models is shown in Figure 2.16 in the Appendix. Aside from the two most slowly rotating models, we

[1]Due to the double-gray radiative transfer in our GCM, the thermal emission is effectively bolometric, making it challenging to compare directly to the 4.5 micron flux from *Zellem et al.* (2014). The phase of peak flux, however, is more directly comparable as it is indicative of the photospheric temperature structure.

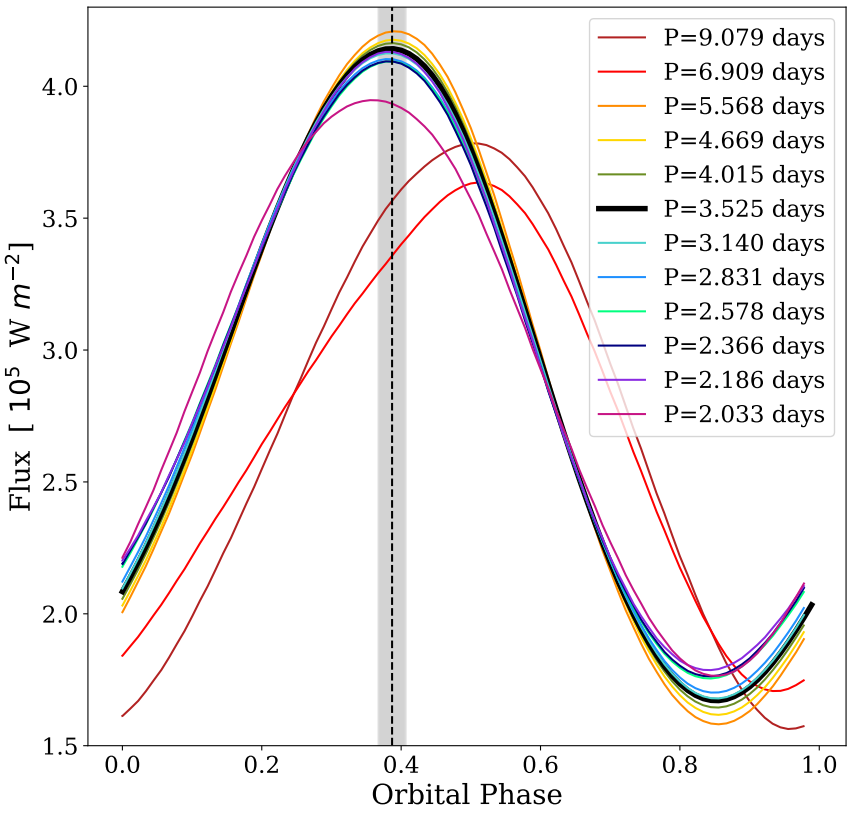

Figure 2.3 Calculated orbital phase curves of total thermal emission from our suite of models with different rotation rates. Only the models with the slowest two rotation rates—with circulation patterns disrupted from the standard hot Jupiter eastward flow—have phase curves that peak after secondary eclipse (which would occur at a phase of 0.5, not shown here). Since phase curves measured at 4.5 microns of HD 209458b show a peak before the secondary eclipse (at 0.387 ± 0.017 *Zellem et al.*, 2014, shown by the black dashed line and grey shaded area), we find that all models except the two slowest rotators are consistent with observations.

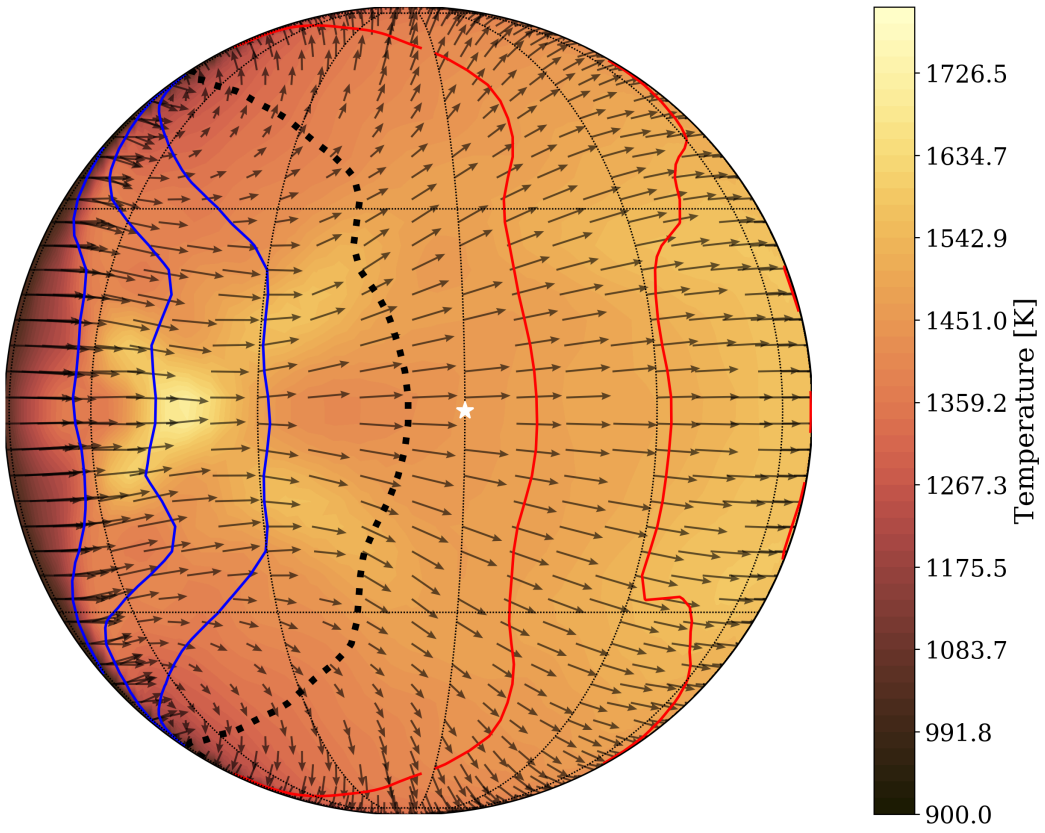

Figure 2.4 The temperature structure of the upper atmosphere ($\sim$ 0.1 mbar), within the region from which the flux in the CO line cores emerges. The projection is centered on the subobserver point at a phase corresponding to the beginning of the observation, shortly after secondary eclipse. The substellar point is marked with a white star. Also shown are contours of the line-of-sight velocity toward (blue) or away (red) from the observer, due to contributions from both the winds and rotation of the planet (Equation 2.2). The contour levels shown in red and blue are $\pm$2, 4, and 6 km/s. The black dotted contour shows the boundary of 0 km/s. Note that whereas at the infrared photosphere the hottest region is east of the substellar point, here it is west of the substellar point due to convergence in the atmospheric flow at that location.

see similar temperature and line of sight velocity fields across the rest of the models. While higher blue-shifted line-of-sight velocities occur on the visible hemisphere, the red-shifted flow extends across a larger fraction of the planet disk. In contrast, the two slowest rotators have weak contributions to the velocity field from their rotation, and the winds generally work in an opposite direction to the rotation, leading to very little Doppler shifting compared to the other models. In addition, the temperature structure is fairly uniform across the visible hemisphere.

A hot feature exists on the western side of the planet (from our perspective, to the left of the subobserver point), where we also see strongly blue-shifted velocities from the combination of rotation and winds blowing around from the night side. Chevron features like this, regions of flow convergence and associated heating, are commonly seen in hot Jupiter GCMs (e.g., *Showman et al.*, 2009; *Rauscher and Menou*, 2010; *Komacek et al.*, 2019) and are related to the transport of momentum from higher latitudes to the equator (*Showman and Polvani*, 2011). Depending on the particular model—and the pressure level within the atmosphere—chevron features may appear to the east or west of the substellar point. Here we see multiple chevron features, both near the infrared photosphere and in the upper atmosphere. New state-of-the-art GCMs in *Deitrick et al.* (2020) also show these features, at multiple resolutions and robust against assumptions regarding vertical hydrostatic equilibrium (see their Figures 19 and 22).

While we have already determined that the phase curve data for HD 209458b excludes the two slowest rotation states for this planet (Figure 2.3), we are still interested to compare the simulated high-resolution emission spectra from these models to the rest of the suite. For most of the models, based on Figures 2.4 and 2.16 we expect that the integrated emission spectra should show both red- and blue-shifting of the CO lines, but the detailed line shapes will be controlled by the complex three-dimensionality of the atmospheric temperature and line-of-sight velocity structures.

Due to the slowing of the winds with increasing rotation rate (see Table 2.4.1 and Figure 2.16) we may expect similar Doppler-induced line profiles for these models. In contrast, for the two most slowly rotating models there may be very minimal Doppler effects shaping the line shapes in their simulated emission spectra.

2.4.3 Radiative Transfer Post-Processing

In order to generate high-resolution emission spectra from our three-dimensional models, we apply the code and method outlined in *Zhang et al.* (2017). Briefly, we take the output from the GCM (temperature and winds at 48 × 96 × 60 points in latitude × longitude × pressure; see Figure 2.5 for the synchronous case and Figure 2.17 for all of the GCM outputs) and solve the radiative transfer equation in a geometrically-consistent manner to produce the thermal emission spectrum emanating from the visible hemisphere of the planet.

The radiative transfer equation is solved in the limit of pure thermal emission:

$$I(\lambda) = B_o e^{-\tau_0} + \int_0^{\tau_o} e^{-\tau} B \; d\tau, \tag{2.1}$$

where I is the intensity at each wavelength λ, B is the Planck function (calculated from the local temperatures) and τ is the slant optical depth along the line of sight toward the observer, taking into account varying opacities throughout the path. We strike 2,304 (= 48 × 96/2) individual line-of-sight intensity rays through the atmosphere and then integrate with respect to the solid angle subtended by each grid cell to produce the planet's emission spectrum in flux units.

To correctly account for the line-of-sight geometry we must first interpolate the temperature and wind output from the GCM onto a fixed-*altitude* vertical grid. This interpolation allows us to readily strike straight-through rays along the observer's sight line. This geometrically-consistent approach to the radiative transfer is some-

what unique in calculations of emission spectra from GCMs. A more common and computationally less challenging technique is to calculate the radiative transfer along radial profiles and assume isotropic emission from the top of the atmosphere. *Caldas et al.* (2019b) have recently shown that using correct ray-tracing geometry is important in calculating transmission spectra from 3-D models; we are not aware of a similar study of geometry's importance in calculating emission spectra.

As a consequence of having varying temperature conditions over the visible hemisphere of the planet, we may expect that our integrated spectra are influenced by spatial variations in the chemical abundances of our main opacity sources. Based on the temperature range spanned by the GCM outputs and the wavelength range modeled (2.28 – 2.35 μm), we expect that H_2O and CO will be the dominant opacity sources. One of the simplest assumptions we can make about the abundances of H_2O and CO is that they are in chemical equilibrium for the local conditions at each location in the atmosphere. However, this neglects the important influence of mixing from atmospheric dynamics, which is likely to bring these species out of chemical equilibrium. The physically and chemically sophisticated work by *Drummond et al.* (2020) demonstrated that 3-D mixing is expected to alter the chemical structure of hot Jupiter atmospheres, with the vertical and horizontal advection components both being significant (with similar results also found by *Mendonça et al.*, 2018). In their model of HD 209458b, however, they found minimal differences in the abundances of CO and H_2O between their kinetics model and the assumption of chemical equilibrium. While they predicted minimal differences between these cases in their simulated (lower resolution) emission spectra, here we further investigate the influence of chemical abundances in high resolution emission spectra.

The double-gray radiative transfer scheme within our GCM simplifies the multi-wavelength opacities of the atmosphere, meaning that we do not prescribe a specific chemistry, nor does the simulation predict chemical mixing. In order to investigate

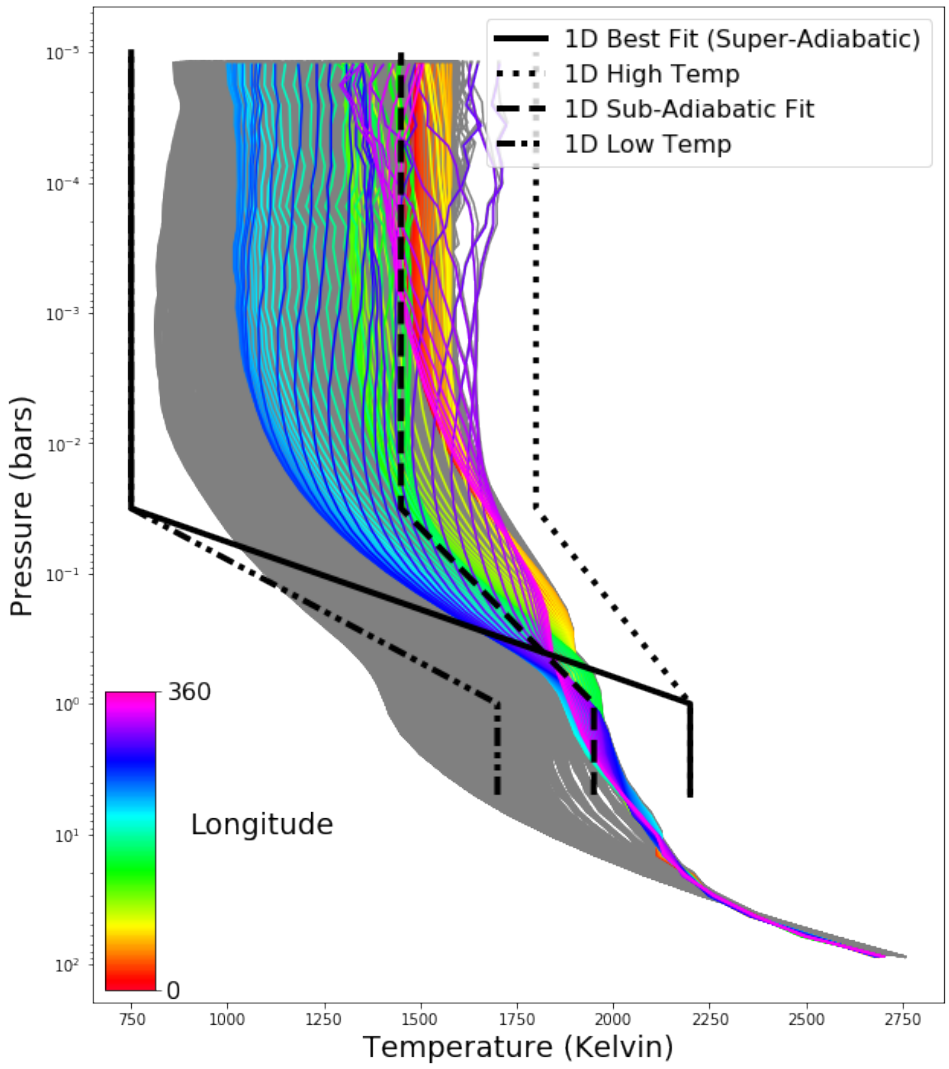

Figure 2.5 Temperature-pressure profiles throughout the atmosphere for our synchronously rotating model of HD 209458b. The rainbow lines show equatorial profiles, with the hue corresponding to the longitude east of the substellar point. The gray profiles are from the entire planet. We use this 3-D atmospheric structure, together with the local wind velocities, to calculate simulated high-resolution emission spectra for cross-correlation with the observed data.The black lines show examples of four temperature-pressure profiles from a suite of 1D models (described in Section 2.6.1) also used to simulate spectra. These models cover the same temperature range realized by our 3-D models, but use only a single profile to represent the entire planet. Note that the best-fit model from this suite has an unrealistic super-adiabatic profile.

the impact of chemistry on the emission spectra, we consider two extreme cases within our post-processing framework: abundances determined everywhere by local chemical equilibrium, or abundances that are fully homogenized throughout the atmosphere and set to some constant volume mixing ratio (VMR). The first assumption applies to the limit where dynamics do not create any significant chemical disequilibrium, while the second may be a proxy for fully efficient mixing, with the caveat that we still need to choose a value for the homogenized abundances. We choose to fix the values for water and CO to the best-fit values from a previous retrieval analysis of these same data (VMR values of $1 \times 10^{-3.5}$ for CO and 1×10^{-5} for water, *Brogi et al.*, 2017).

There is significant evidence in the literature suggesting a water abundance below the solar equilibrium value (which would be $\sim 5 \times 10^{-4}$; *Madhusudhan*, 2012) for HD 209458b (although see *Line et al.*, 2016). From previous analysis of these HRS data, a marginal evidence for H_2O was claimed by *Brogi and Line* (2019), with a peak around VMR $\sim 1 \times 10^{-5.5}$ but with an unbounded lower limit. From HST transmission spectroscopy, *Barstow et al.* (2017) and *Pinhas et al.* (2019) both retrieve a low water abundance of 1×10^{-5} and $1 \times 10^{-4.7}$, respectively. These results are particularly significant as they are obtained with models accounting for the presence of aerosols, and therefore include their known ability to mimic a low water abundance by reducing the contrast of the water band in the WFC3 pass-band. Lastly, a recent attempt at combining both low-resolution and high-resolution emission spectroscopy was presented by *Gandhi and Madhusudhan* (2019), resulting in a VMR of $1 \times 10^{-4.1}$. The observational constraints presented above and the weak detection of water in these data inspired us to explore an additional set of models without water vapor, along with our constant VMR models with water under-abundant compared to equilibrium calculations.

In order to self-consistently account for Doppler shifts resulting from winds and

rotation in the high-resolution spectra given that the resolution is comparable to the speeds of atmospheric motion (∼km/s), we calculate the line-of-sight velocity for a latitude-longitude (θ, ϕ) pair at an atmospheric height of z as:

$$v_{LOS}(\theta,\phi) = -u\sin(\theta) - v\cos(\theta)\sin(\phi) + w\cos(\theta)\cos(\phi) - (R_p + z)\Omega\sin(\theta)\cos(\phi) \quad (2.2)$$

where u, v, w are the wind speeds in the east-west, north-south, and radial directions, respectively, and Ω is the planet's bulk rotation rate. We calculate simulated spectra both with and without these Doppler shifts, so that we can quantitatively evaluate how much they contribute to the observed data.

We calculate the simulated emission spectra at a higher spectral resolution ($R \sim 250,000$) than that of CRIRES data across the same wavelength range (2.2855 – 2.3475 μm). During the data analysis, the simulated spectra are convolved with a Gaussian kernel to match the resolving power of CRIRES ($R = 100,000$).

As the planet rotates throughout the time of observation, we calculate spectra for each exposure time. The atmospheric structure from the GCM is output every 4 degrees in phase. In order to match the more frequently sampled observed phases, we created interpolated spectra as follows. For each exposure (corresponding to some orbital phase) we take the GCM outputs from the two nearest-neighbor phases, rotate each atmosphere to the correct orientation, calculate simulated spectra from each, and then combine those two spectra, weighting linearly by how close each GCM output is to the phase of observation. Even before this weighted average, the spectra produced from two adjacent GCM outputs differed only marginally. For the fastest rotating model, the average difference was less than 5%. For the slowest rotating model, this difference was only 0.6% on average. Thus, in our interpolation process, the resultant changes to the spectra were on order of a few percent at most.

2.4.4 Simulated Emission Spectra

Simulated spectra from the full set of 12 rotation models over a partial range of the total wavelength coverage for a time near the beginning of the observation (phase of ~ 0.52) are shown in Figure 2.6. For each model, versions of the spectrum with and without Doppler effects are plotted in solid and dashed lines, respectively. As expected from the discussion of their circulation patterns above, the models with the slowest rotation rates have very little Doppler broadening. In contrast, all of the other models show significant broadening, without a strong dependence on the planet's rotation rate because the faster winds in slower rotating models work to contribute to the broadening. The main notable difference between these spectra is in the relative depths of the spectral lines, which is a function of the vertical structure of these atmospheres, both thermal and as probed by the line opacities.

We can investigate the relative contributions of the thermal profile and changing opacities to the depth of the spectral lines by comparing the different chemical assumptions we use in the post-processing. Figure 2.7 shows the differences in spectra calculated under our assumptions of chemical equilibrium abundances or constant volume mixing ratios, both with and without water included as an opacity source, for our synchronous model. The spectral features from CO appear fairly consistent for all of our assumed chemistry conditions. Over the range of pressures and temperatures that contribute to our planet's dayside emitted spectra ($P \sim 0.1 - 100$ mbar, $T \sim 900 - 1700$ K, see Figures 2.1 and 2.4), local chemical equilibrium abundances for CO at solar composition are fairly constant, at a VMR of $\sim 4 \times 10^{-4}$, only slightly higher than the value we use for our constant VMR assumption.

In contrast, the assumption of local chemical equilibrium produces significantly different water abundances than the constant VMR value we use (the best-fit value from a previous 1-D analysis of these data; *Brogi et al.*, 2017). For the temperature and pressure conditions probed by these emission spectra, local chemical equilibrium

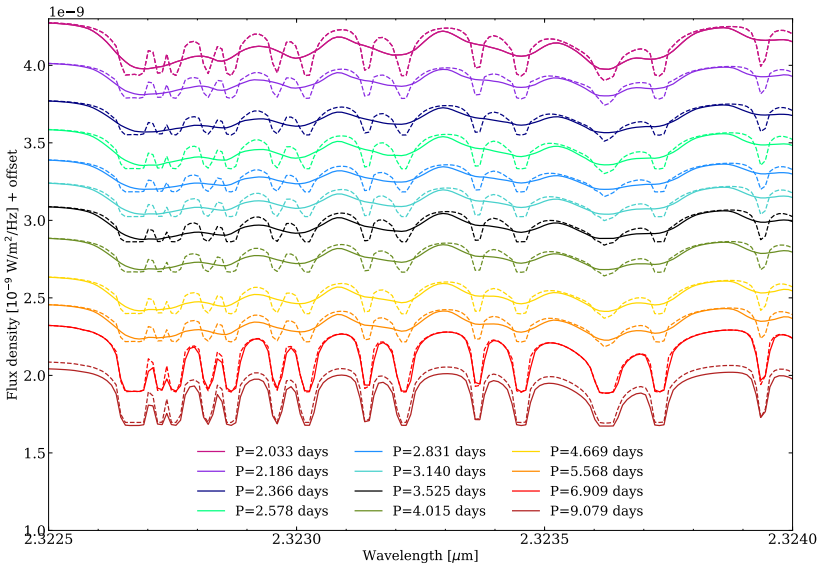

Figure 2.6 Simulated spectra from post-processing the atmospheric structures predicted by our GCM, color coded by the rotation rate assumed for each model (with the synchronous model in black). In these spectra we only include opacity from CO (not water; see Figure 2.7 for comparison) and assume local chemical equilibrium abundances. The dashed lines show spectra produced without the influence of Doppler effects while the solid lines account for shifts and broadening due to winds and rotation. The main result of the atmospheric motion is to produce significant line broadening; for most of the models the amount of broadening is similar, due to a trade-off between the contributions from winds and rotation. The two most slowly rotating models have very little broadening, due to the weak contribution from rotation, but also because of westward winds in these models.

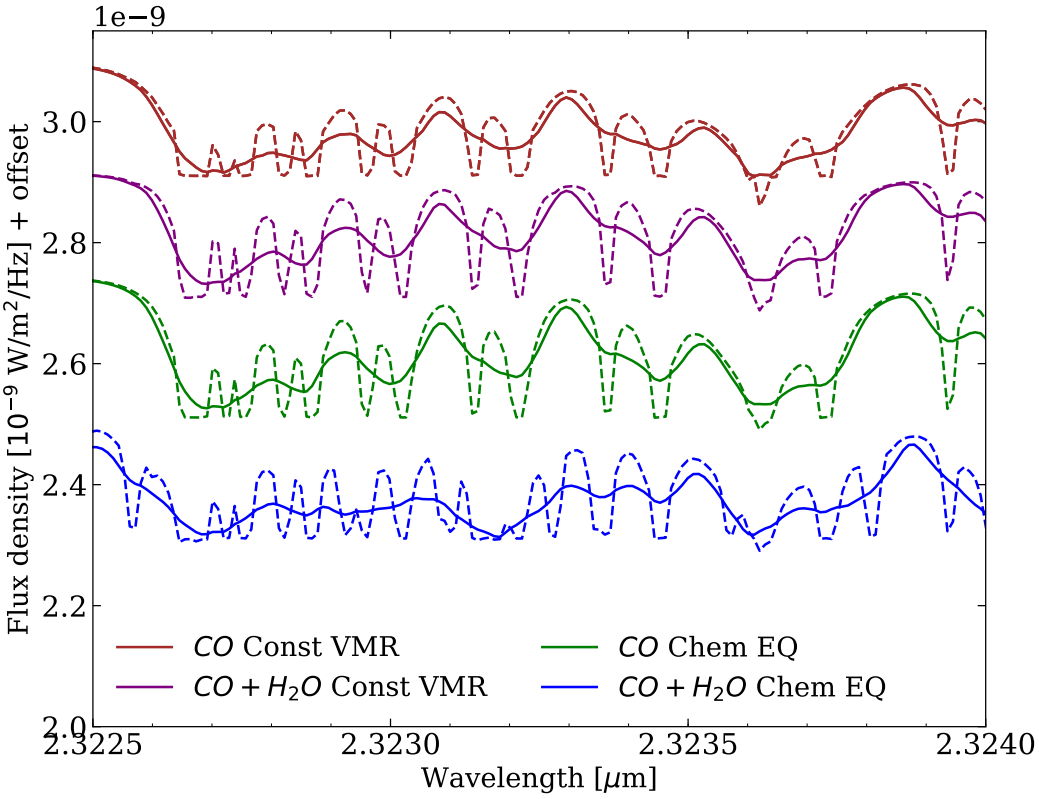

Figure 2.7 Simulated emission spectra, post-processed from our 3D atmospheric model, comparing the different assumptions used for the abundances of water and CO, the main sources of opacity at these wavelengths. These spectra are from the synchronously rotating model, over a fraction of the wavelength coverage of the observations; the solid and dashed spectra are produced with and without the Doppler effects of winds and rotation, respectively. The spectra produced assuming abundances determined by local chemical equilibrium and fixed to a constant value look very similar for the CO features. The assumption of local chemical equilibrium results in much more abundant water with much stronger spectral features in comparison to the constant value that best-matches previous observations.

abundances for water have VMR $\sim 10^{-3} - 10^{-4}$, with the hottest and lowest pressure regions dipping down to VMR $\sim 10^{-7}$. These abundances are mostly significantly higher than our constant VMR value (10^{-5}), leading to much more visually apparent spectral features in Figure 2.7. These differences will strongly influence the significance of detection in our data analysis, as discussed in Section 2.6.

One measure of the effect of Doppler shifting across the entire spectrum can be assessed by cross correlating each simulated emission spectrum with the non-Doppler shifted spectrum calculated from the same model, as shown in Figure 2.8, where we have plotted these cross correlation functions for each of our 12 rotation models. The dashed black line shows the spectrum from the synchronous model without Doppler effects cross correlated with itself, to characterize the intrinsic width of the cross-correlation function. The two slowest rotators have the least amount of broadening and the second slowest rotator actually has a cross-correlation function similar to the unshifted reference. All of the other rotation rates produce roughly similar levels of broadening, with only minimal net red- or blue-shifts (and no trend in the shift with rotation rate), in agreement with our previous findings in *Zhang et al.* (2017).

The similarity in Doppler broadening between all but the two most slowly rotating models is to be expected, from the discussions of circulation patterns above and from visual inspection of their spectra in Figure 2.6. As a more quantitative comparison, in Figure 2.9 we show the width of the cross correlation function, calculated at 80% of its maximum (shown in Figure 2.8) as a function of the rotation period of the simulated planet, normalized to the synchronous model. This width serves as a proxy to understand the degree of broadening caused by the differing sources of Doppler effects. The filled and unfilled circles correspond to spectra that have been broadened by both winds and rotation and only rotation, respectively. The scatter in the unfilled circles is a result of differences in temperature structure in the corresponding GCM. Aside from the two slowest rotating models—which exhibit westward

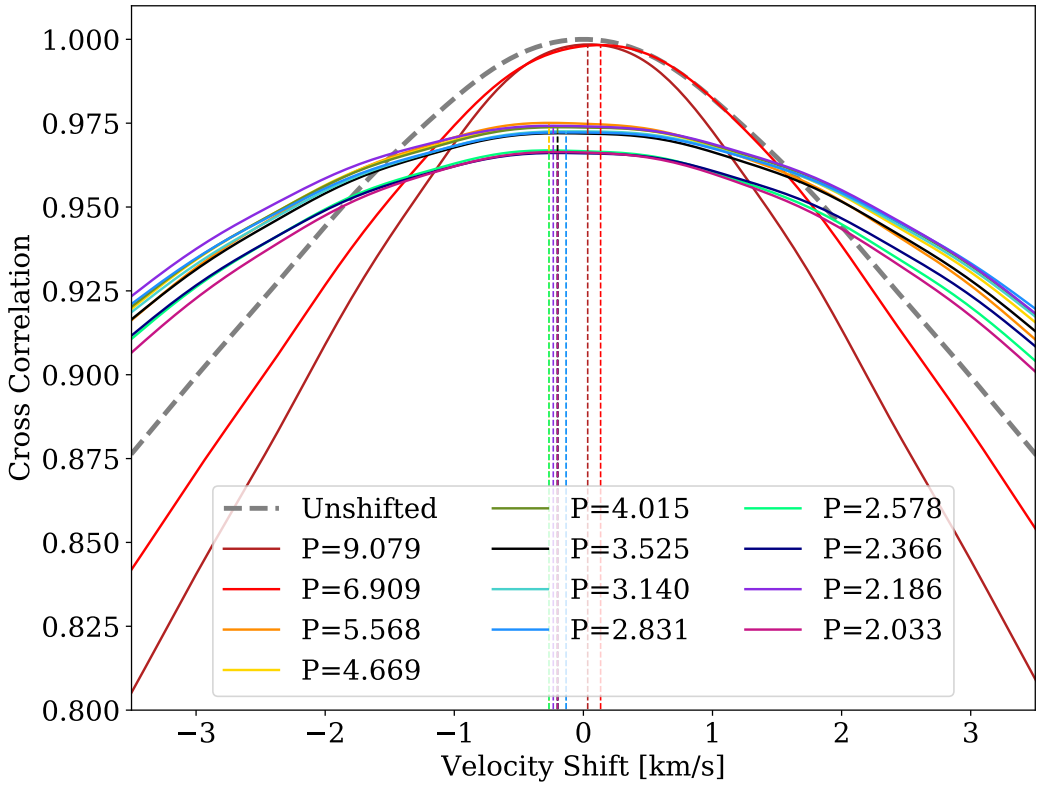

Figure 2.8 For each of our 12 models with different rotation rates, we cross-correlate two simulated spectra from the same model: one with Doppler effects included and one without. (The solid black line is the synchronous model.) The resulting cross correlation functions, plotted here, allow us to assess the contribution of the planet's winds and rotation to the overall Doppler shifting and broadening of the lines in the emission spectra. The gray dashed line shows the synchronous model's non-Doppler shifted spectrum, cross correlated with itself, to show the intrinsic broadening in the spectra. The dotted vertical lines mark the velocity at the peak of the cross correlation function for each model. All but the two most slowly rotating models show significant—and similar—broadening, while none of the models exhibit large net red- or blue-shifts. CRIRES allows us to fully resolve the shapes of these line profiles since its instrumental profile (approx $\sim$ 3 km/s) is smaller than the FWHM of these lines.

flow, opposite of the direction of rotation—allowing the spectra to also be broadened by the winds cause the width to increase. We show the result of a single temperature structure artificially broadened at the various rotation rates with the black dashed line. The unfilled circles lie both above and below this line, meaning that the amount of broadening in the lines themselves does not allow us to constrain the rotation rate strongly. Because the total broadening of the line is sensitive to temperature and wind structures in addition to rotation rate, we are unable to retrieve a rotation rate from the broadening width of the spectra alone.

2.4.5 1D Atmospheric Models

In addition to producing post-processed spectra from the 3-D GCM outputs, it is also instructive to compare our results against spectra produced from 1-D models of HD 209458b. We perform comparisons against a suite of previously published 1-D models (described in Section 2.6.1) and choose four representative T-P profiles to show in Figure 2.5. These four chosen representatives consist of the best fit 1-D model to the observations, two profiles that bound the temperatures produced in our GCM, and a model that approximately reproduces the average equatorial T-P profile produced by our GCM.

2.5 Observational Data of HD 209458b

The data we re-analyze in this paper were originally published in *Schwarz et al.* (2015), where the full details of the observations can be found. In brief, the star HD 209458 (K=6.31 mag) was observed for a total of 17.5 hours with the CRIRES instrument on the VLT as part of the ESO program 186.C-0289 in August and September 2011. The system was observed on three separate nights, always shortly after secondary eclipse. Here we utilize only the first two nights of data, which were observed in nodding mode. We discard the third night, because this was observed in

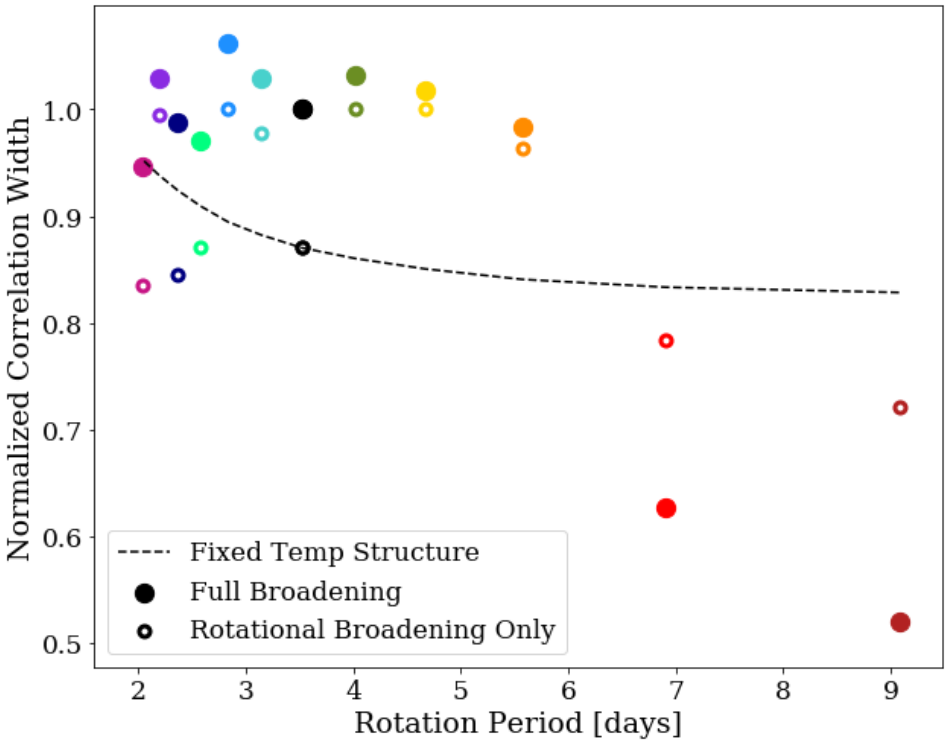

Figure 2.9 Width of the cross correlation function, calculated at at a height of 80% of its maximum (shown in Figure 2.8) as a function of the rotation period of the simulated planet, normalized to the synchronous model. The filled circles correspond to spectra that have been broadened from both wind and rotation and the open circles represent spectra that have been broadened only by rotation. To produce the black dotted line, we took the temperature structure of the synchronous model and calculated the resulting broadening for each rotation rate. For the two slowest rotating models, we find that the westward rotating winds cause the fully broadened spectra to have a smaller width than the spectra only broadened by rotation. For all of the other models, we see the addition of winds cause the resulting correlation width to increase. Because the total broadening of the line is sensitive to temperature and wind structures in addition to rotation rate, we are unable to retrieve a rotation rate from the broadening width of the spectra alone.

staring mode for testing purposes and shows a higher noise budget. As explained in *Schwarz et al.* (2015), the spectra were optimally extracted via the standard ESO pipeline and then re-calibrated in wavelength using the known position of telluric lines as a reference. Due to previously reported issues with the fourth detector of CRIRES, we chose to include only the first three detectors in our analysis. Extracting the planetary signal from the calibrated spectra poses a unique challenge due to the highly unequal flux ratio of the Hot Jupiter and the star. Furthermore, for ground based observations, spectral absorption lines formed in the Earth's atmosphere (telluric features) must be accounted for and are often so strong that parts of the data must be masked completely as they exhibit near-zero flux.

In order to decouple the planet's spectrum from the stellar and telluric lines, we utilize standard analysis algorithms (see (*Brogi and Line*, 2019, Section 3.2) for a detailed description for HRS. These are based on the principle that over the relatively short period of observations, the planetary lines are Doppler shifted by a varying amount due to the changing orbital motion of the exoplanet, while telluric and stellar lines are essentially stationary [2]. Thus, by removing the parts of our signal that do not shift with time, we are left with the planetary spectrum. We apply the latest iteration of the HRS analysis described in *Brogi and Line* (2019), to which we point the reader for a step-by-step description. In short, the algorithm determines a model for the time-dependent stellar and telluric spectrum empirically from the observations, and normalizes the data by dividing out such model. The resulting data product only contains the planet spectrum, deeply embedded in the stellar photon noise at this stage.

Similarly to previous studies of atmospheric circulation from transmission spectra (*Brogi et al.*, 2016), Flowers2019 we run two parallel versions of the analysis: one

[2]Stellar lines do shift by ~ 100 m s^{-1} per hour of observations due to the barycentric velocity of the observer and the stellar motion around the center of mass of the system, but these are negligible compared to the change in planet's radial velocity.

with the data as is (hereafter the *real* data), and one containing each model spectrum injected at a small level (hereafter the *injected* data), chosen to be $0.1\times$ the nominal value. Here the nominal value is the planet's emission spectrum in units of stellar flux, i.e. scaled by a blackbody at the stellar effective temperature and multiplied by the planet-to-star surface ratio (see system parameters in Table 4.4.1). The exact value of the scaling factor is not important for the outcome of the analysis, as long as it is significantly smaller than the nominal value. A small scaling factor is needed to realistically simulate the effects of the analysis on each model spectrum without sensibly changing the signal content of the data. In order to detect the planet's emission spectrum, buried in the stellar noise at this stage, we use the standard technique in high-resolution spectra, where we cross-correlate a template spectrum—or set of templates—for the planet with the data. If the template is a good representation of the planet's spectrum, there will be a maximum cross-correlation value at velocities corresponding to the planet's orbital radial velocity during the time of observation.

The significance of each tested model is determined as in previous work: we compute the difference between the CCF of the injected data and the CCF of the real data. This will remove the cross correlation noise and the correlation with the real planet signal, and provide us with the *model* cross correlation. Note that this is different from the CCF obtained by autocorrelating the spectra, because it contains any alterations that our data analysis necessarily introduces on the planet signal while removing telluric and stellar spectra. We then compare the model CCF and the real CCF via chi-square, and we assign a significance by discriminating against a non-detection, which in our case is a flat cross correlation function (i.e. a straight line). Finally, n-σ confidence intervals are determined by the region in the parameter space where the detection significance drops by $n\,\sigma$. For the full explanation of how the chi-square statistic is utilized, we refer the reader to *Brogi et al.* (2016) and *Flowers et al.* (2019).

2.6 Data Analysis Results

We apply the cross correlation and significance test explained in Section 2.5 to the spectra produced from our three-dimensional model, as well as to a suite of one-dimensional models for comparison. These one-dimensional models are taken from previous work and further information about them is provided in Section 2.6.1.

We find significant detection of the planet's signal over the range of template spectra tested, but our strongest detection came from the spectra produced by post-processing our three-dimensional model, as reported in Table 2.6. In particular, we found the highest significance of detection (at 6.8 sigma) for the model that was post-processed assuming uniform volume mixing ratios for CO and water, and that included the Doppler effects from winds and rotation. Figure 2.10 shows the significance of cross-correlation detection for this model, over the range of orbital and rest frame velocities included in the analysis. Note that these observations have a relatively small phase range and they are taken close to superior conjunction, where the planet's radial velocity curve can be approximated with a linear function of time at small signal to noise. This means that higher orbital velocities can be somewhat compensated for by allowing the planet to have a positive rest frame velocity (i.e., anomalous motion away from the observer), resulting in some inherent degeneracy between those parameters. Our detection agrees with a zero rest frame velocity for the planet and the orbital velocity reported in *Stassun et al.* (2017).

One of the main results from our analysis is this: *that template spectra from our 3-D model—calculated without any fine-tuning—outperform a large suite of template spectra from one-dimensional models* (a 6.8 sigma detection significance compared to 5.1; Table 2.6). This is evidence that the three-dimensional structure of this hot Jupiter's atmosphere leaves detectable signatures in the disk-integrated high-resolution emission spectrum of the planet. In the following sections we explore the various physical properties that could contribute to this enhanced detection and

Table 2.3. Highest significance detections for the model spectra tested in this work.

Dimensions	Abundances	Molecules Included	Doppler Effects On	Doppler Effects Off
3D	Chemical equilibrium	CO	6.49	6.40
	Chemical equilibrium	CO and H_2O	4.22	3.39
	Constant volume mixing ratio	CO	6.02	5.72
	Constant volume mixing ratio	CO and H_2O	6.87	6.37
1D	Constant volume mixing ratio	CO and H_2O	-	5.06

Note. — Highest significance detections for the model spectra tested in this work. The highest increase in detection significance came from using a 3D atmospheric model, compared to the 697 1D models tested. Note that the best fitting 1D model exhibits a non-physical, super-adiabatic lapse rate. For detections broken down by rotation rate, see Table 2.9 in the appendix.

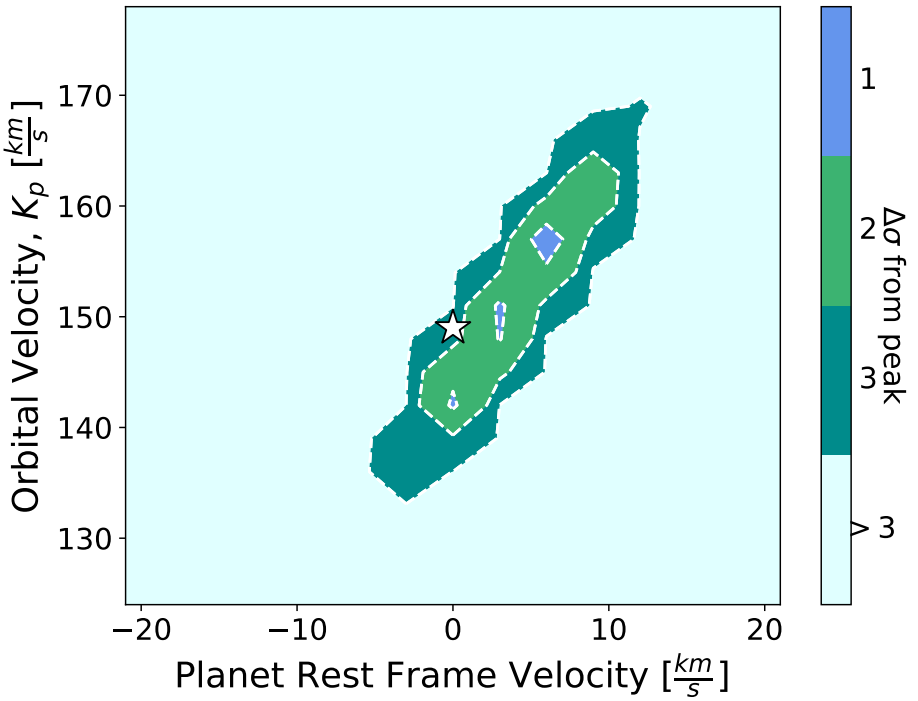

Figure 2.10 The significance of our detection of the planetary signal, showing 1-, 2-, and 3-σ confidence intervals from the peak detection (at 6.78 σ, for our spectra calculated using water and CO with constant abundances), over the velocity parameter space explored by the cross correlation fitting. The literature orbital velocity of the planet is shown as a white star, as is its expected rest frame velocity. Our analysis confidently detects the planet, at its expected velocity.

evaluate their influence.

2.6.1 Comparison to 1D Models

To compare our results with the modeling presented in past work, we estimated the significance of the cross correlation with two grids of models obtained with one-dimensional, plane-parallel radiative-transfer calculations. The first grid of models is described in *Schwarz et al.* (2015) and consists of 704 models describing a parametric $T-p$ profile with a region at constant lapse rate ($dT/d\log(p)$) sandwiched between two isothermal regions. Pressure and temperature at the upper and lower boundaries can be changed, thus exploring a wide range of lapse rates up to $d\log(T)/d\log(p) = 0.31$, which includes non-physical super-adiabatic lapse rates. Relative abundances of CO and H_2O are also varied in the range $\log(CO/H_2O)$ = 0-1.5. After excluding models with a thermal inversion layer (ruled out in *Schwarz et al.* (2015) we were left with 546 models to test. Since these models were not designed to explore high abundance ratios between CO and H_2O, we also tested a subset of the models described in *Brogi et al.* (2017) and sampled from the low-resolution posterior retrieved by *Line et al.* (2016). From that initial sample of 5,000 models we remove those models with thermal inversion and/or $\log(CO/H_2O) < 1.5$ (as low CO/H_2O models are already included in the grid from *Schwarz et al.*, 2015), resulting in 151 additional models, spanning abundance ratios up to $\log(CO/H_2O) = 3.0$. All these models have a sub-adiabatic lapse rate in the range $0.05 < d\log T/d\log p < 0.08$. The only broadening that has been applied to the 1-D model spectra arises from the pressure and thermal broadening components of the Voigt profile used to generate the spectral lines.

Of the 697 one-dimensional models tested, the highest measured significance is 5.06σ, with only 14 models reaching a significance value greater than 4σ. These are models with a steep lapse rate ($0.13 < d\log T/d\log p < 0.31$) and an abundance ratio of 10-30 between CO and H_2O. Thus, the vast majority of the 1-D models

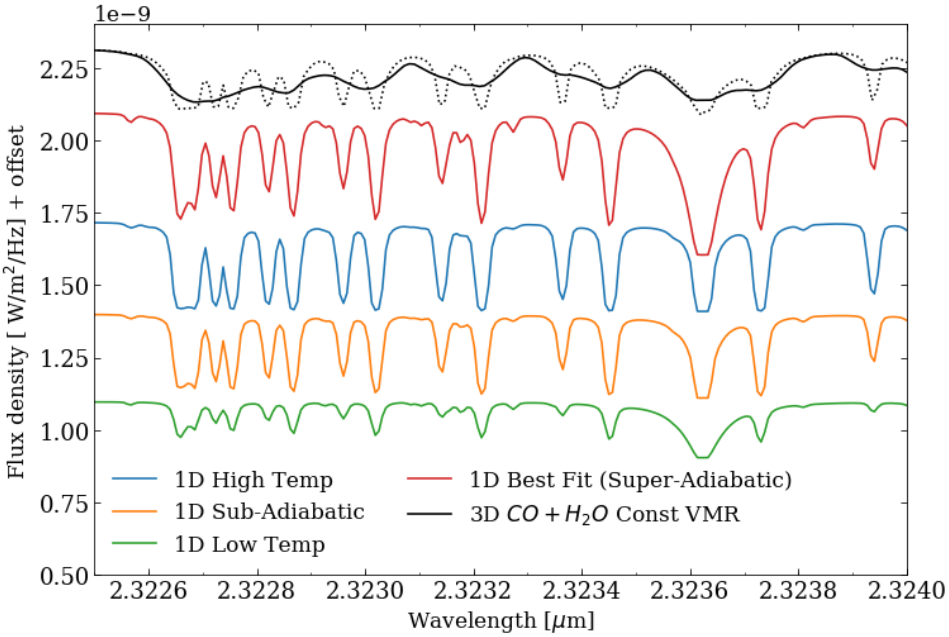

Figure 2.11 A comparison of the spectra produced from a 1D atmosphere with our best fitting 3D model (in black). The solid black spectrum has been broadened by Doppler effects arising from winds and rotation. These sources of broadening are not included in the dotted black spectrum or any of the 1D spectra. All of the models appear to show the same absorption lines but the relative depths of absorption, influenced by the underlying temperature structure and chemical abundances, changes with each model. These variances in relative depth and line shape result in a range of significance of detection when cross correlated with the data.

return a significance below the threshold of detection (usually set at 4σ for these HRS observations), and consistent with the tentative detection reported in *Schwarz et al.* (2015). We note that the temperature-pressure profiles explored in the set of 1-D models encompasses the range realized in our 3-D model (Figure 2.5). This implies that the deficiency in the 1-D models is not that they didn't include the *appropriate* physical conditions of the planet, but rather that those conditions are inherently, and observably, three-dimensional. In Figure 2.11, we show a subset of the spectra produced from the 1D models and spectra from our best fitting 3D model. All the spectra shown seem to show the same absorption lines, yet still result in a range of detection strengths. The subtleties in spectral line shapes and relative depths are not adequately captured by the 1D models.

2.6.2 Influence of Temperature Structure

As Table 2.6 hints at, and as we will discuss in subsequent sections, the improvement in detection from using the 3-D models over the 1-D models is not primarily due to the chemical or velocity structure of the atmosphere, as those influences on the spectrum only give marginal improvements in the significance of detection. Instead, we find that the contribution from multiple regions of the planet, with different thermal structures, is a much better match to the observed data than a representation of the planet with a single thermal profile. Whether the influence of spatial inhomogeneity is intrinsically within *all* HRS emission observations requires further study, but for this particular planet we find it to be the case. Recent complementary work by *Taylor et al.* (2020) predicts that James Webb Space Telescope observations may similarly contain inherent signatures of multiple thermal regions, although whether this inhomogeneity will be measurable or not depends on wavelength coverage and signal-to-noise.

2.6.3 Influence of Chemical Structure

Table 2.6 shows that for models with CO alone the assumption of abundances that follow local chemical equilibrium is slightly preferred over using the best-fit value from a previous analysis of these data (*Brogi et al.*, 2016) However, as discussed in Section 2.4.4, local chemical equilibrium does not predict strong variations in the abundance of CO throughout the atmosphere, meaning that the improvement of signal does not come from any significant chemical heterogeneity influencing the disk-integrated spectra, but rather from an abundance slightly closer to reality. It may be the case that by capturing the inherent *thermal* inhomogeneity of the atmosphere, we can more accurately find the correct chemical abundances (*Taylor et al.*, 2020).

In contrast to our results for CO, Table 2.6 shows a strong decrease in the significance of planet detection when using chemical equilibrium values for water. The data

prefer depleted abundances for water; Section 2.4.4 and the discussion surrounding Figure 2.7 demonstrate that water at equilibrium values would result in large spectral features that are not apparent in the data, according to our analysis. It is noteworthy that the data are not suggesting a complete lack of water; the very low water abundance used in calculating the spectra with constant VMR does improve the planet detection over the comparable CO-only model.

A full gridded analysis of varying chemical abundances is outside the scope of this work. Even without considering a full grid,these results show that the 3-D chemical structure of the atmosphere contributes to our enhanced detection, compared to 1-D models, insofar as it seems to slightly more robustly predict the abundance of CO in the atmosphere. Notably, we find that the data prefer a water abundance that is orders of magnitude depleted below chemical equilibrium values.

2.6.4 Influence of Atmospheric Doppler Effects

In addition to predicting the 3-D temperature structure of the planet's atmosphere, our GCM also predicts the wind vectors throughout, all of which are influenced by the rotation rate assumed for the planet. Here we examine how the Doppler shifts and broadening due to winds and rotation in our simulated spectra may contribute to our enhanced detection of the planet's signal over the 1-D models that do not include this additional physics, and whether the data can help to empirically constrain the planet's wind speeds and rotation rate (generally assumed to be synchronous with its orbit).

In Table 2.6 we report that including the spectral line shifting and broadening from winds and rotation does enhance our detection of the planet, but with only a minor increase in significance over the spectra without Doppler effects. As discussed and shown above in Figure 2.8, the main influence of the Doppler effects (for most of the models) is to broaden the spectral lines, since both winds and rotation contribute

similar symmetric velocity patterns. Thus we expect the main contribution to the increased detection is that the planet's actual spectrum does contain some significant broadening from winds and rotation.

Even with a symmetric velocity field, an uneven brightness pattern across the planet can result in the red- or blue-shifted side of the planet contributing more emission to the disk-integrated spectrum, resulting in a net Doppler shift (*Zhang et al.*, 2017). Figure 2.8 has small net Doppler shifts for the models. Depending on the precision of the data, this could result a small anomalous radial velocity of the planet if not included in the analysis. In order to test whether a net Doppler shift contributes in any significant way to our detection, in Figure 2.12 we plot the models' significance of detection in velocity space, comparing the spectra with and without the Doppler effects included. While we see an overall increase in detection significance with the Doppler effects included, there is no very noticeable shift in velocity space between the models with and without them. This agrees with our discussion above, that the main improvement in significance comes from the broadening of the lines, rather than any net Doppler shift.

2.6.4.1 Constraints on rotation and winds?

As part of this investigation, we wanted to see what constraint, if any, could be placed on the rotation rate or wind speeds for HD 209458b. In Figure 2.13 we show how the significance of detection depends on which rotation rate we use in our 3-D model of the planet (plotted here as the planet's equatorial velocity). The significance of detection is largely insensitive to the planet's rotation rate, aside from the two most slowly rotating models being slightly disfavored (and those are also inconsistent with thermal phase curve data; see Figure 2.3 and discussion). Our small improvement in detection from including Doppler effects, combined with the strong similarity in Doppler broadening for all but the slowest models (Figure 2.8), makes this result

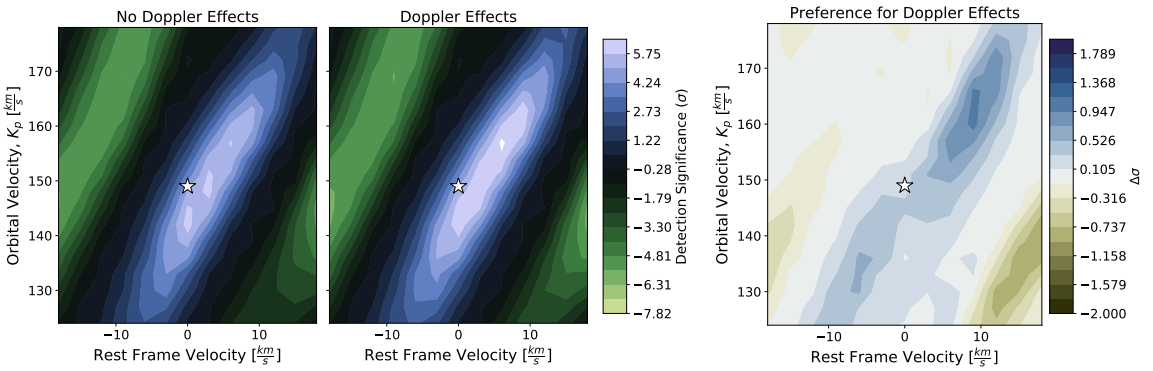

Figure 2.12 A comparison between our significance of planet detection with and without Doppler effects included in our best-fit simulated spectra (*left* and *middle* plots), shown as a function the planet's assumed orbital velocity and its rest frame velocity (which should be zero unless there is anomalous motion). The *right* plot shows the difference in significance caused by including the Doppler effects in our analysis. While there is a slight increase in detection significance, this does not correspond to any net shift in velocity space, indicating that it is largely due to the line broadening rather than any shifting.

unsurprising.

However, it is a valuable result to determine that the amount of Doppler broadening for models across a wide range of rotation rates is so similar (quantified in Figure 2.9). It indicates that we cannot constrain rotation rates as well as we might think from rotational broadening alone; the winds are faster in the more slowly rotating models and their predominantly eastward direction lets them compensate for the weaker rotational broadening. Although our particular analysis is only for observations around one particular orbital phase, the eastward wind pattern extends around the whole globe and so we expect the same behavior regardless of orbital phase. This is the same general behavior previously reported for high-resolution transmission spectra in *Flowers et al.* (2019); we have now shown that emission spectra are subject to this inherent physical uncertainty as well.

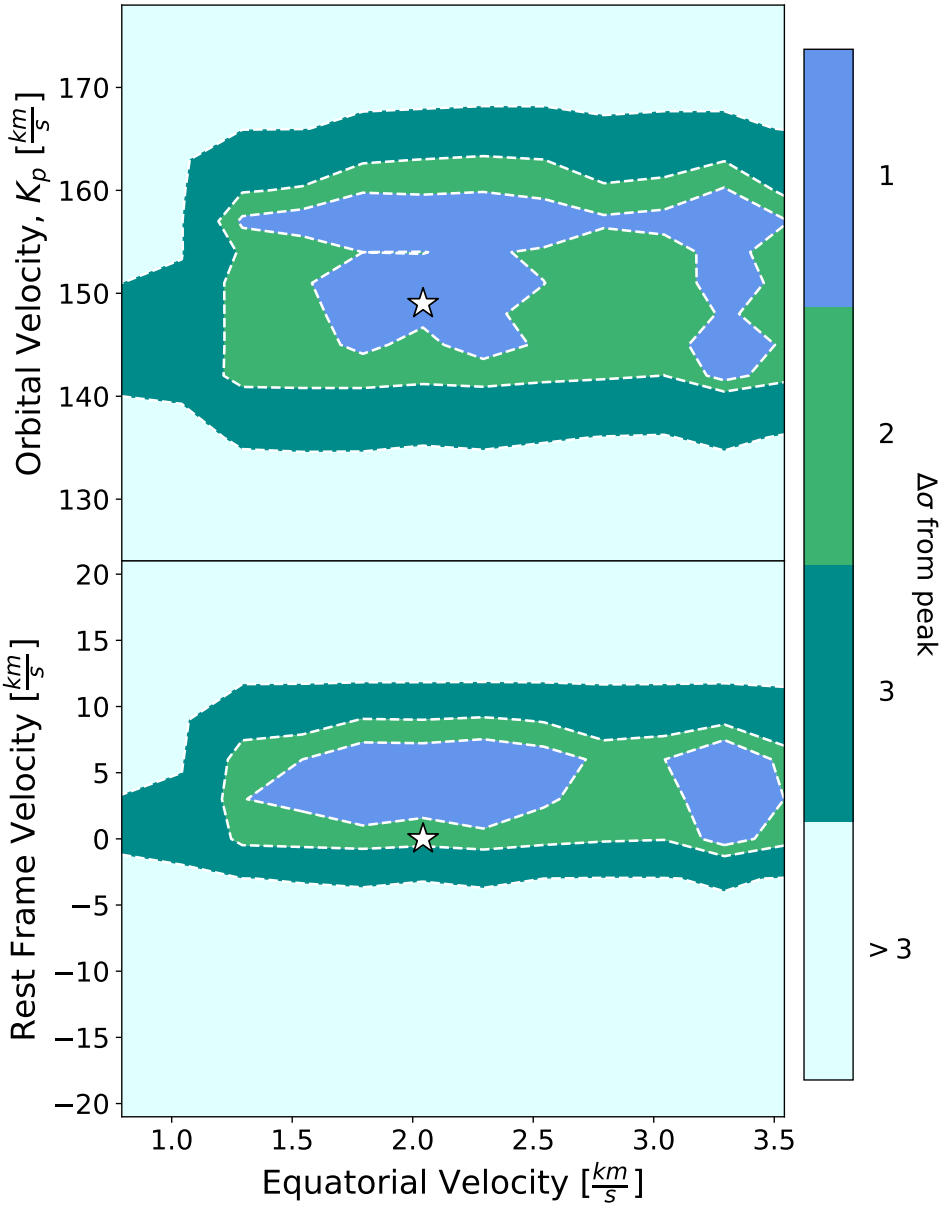

Figure 2.13 Confidence intervals from cross-correlation between the data and our 3D models with constant volume mixing ratios of CO and water, and Doppler effects included. Similar to Figure 2.10, the white star marks literature values and equatorial velocity for synchronous rotation. Here, the two plots show the 1-, 2-, and 3-σ confidence intervals for models with different rotation rates as a function of orbital velocity (*top*) and rest frame velocity (*bottom*). The data have a slight aversion to the two most slowly rotating models (low values of equatorial velocity), but otherwise the temperature structures and wind patterns of all other models are roughly equally well allowed by the data.

2.7 Conclusions and Summary

In this project, we combined state of the art observational and modeling techniques to obtain a higher significance detection than could be achieved with either of these techniques alone. We ran a 3D atmospheric model for the hot Jupiter, HD 209458b, for a range of rotation rates. We post-processed the resulting atmospheric structures in a geometrically correct way to generate template spectra. We then cross correlated the synthetic spectra with previously published data for this planet from CRIRES/VLT and detected the planet at a greater significance than a whole suite of 1D models. We explored why the 3D models were a strong improvement over the 1D models by looking at properties such as temperature and chemical structure and Doppler shifts from winds and rotation. Our main findings are summarized as follows:

- High resolution emission spectra are sensitive to the 3D structure of the atmosphere, at least for these data of this particular hot Jupiter.

- One dimensional models, despite covering the same range in temperature and pressure, returned detections that were at best $\sim 1.8\sigma$ lower than our best fit from 3D models.

- In terms of detection significance, the primary improvement is from the use of a 3D temperature structure, with secondary improvements related to the chemistry and Doppler effects.

- Doppler shifts are present in the high resolution spectra, but are unable to offer strong constraints for wind speed or rotation rate. We have shown that the widths of the spectral lines cannot be directly related to the planet's rotation rate alone.

- Our analysis detects water in these high resolution spectra of HD 209458b, but at a significantly depleted value compared to the solar chemical equilibrium

abundance.

High resolution spectroscopy enables detailed characterization of exoplanets. It is becoming increasingly clear that the three-dimensional nature of planets and their atmospheric dynamics influence high resolution spectra. Looking toward the upcoming era of high resolution spectrographs on Extremely Large Telescopes, we eagerly await what detailed atmospheric characterizations will be possible.

2.8 Acknowledgments

This research was supported in part by NASA Astrophysics Theory Program grant NNX17AG25G and the Heising-Simons Foundation. MB acknowledges support from the UK Science and Technology Facilities Council (STFC) research grant ST/S000631/1. We thank the referee for their constructive feedback which helped to improve the clarity of this paper.

2.9 Appendix

Here we present the GCM results for our 12 models of HD 209458b with different rotation rates, showing the temperature and wind structures of the model atmospheres.

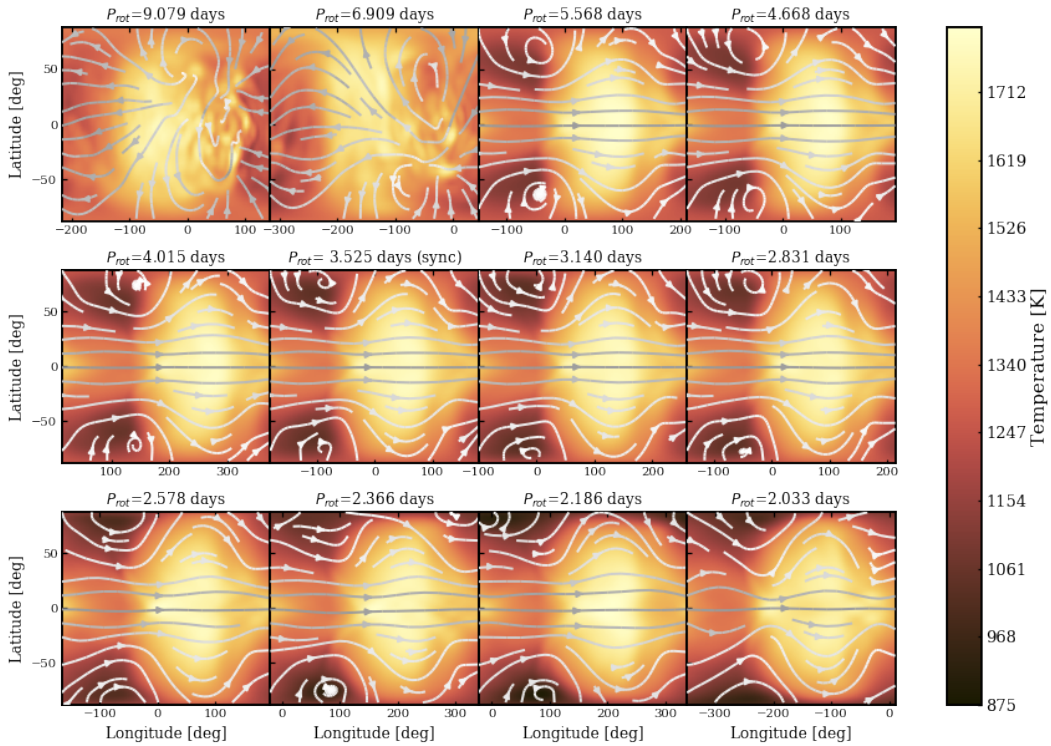

Figure 2.14 Temperature and wind structure at the infrared photosphere (P=65 mbar) for all 12 GCMs. In each case the orientation of the map is such that the substellar point is in the center of the plot. While most models show a temperature structure influenced by the standard hot Jupiter eastward equatorial jet, the two most slowly rotating models have disrupted circulation patterns and instead have their hottest regions shifted slightly westward of the substellar point.

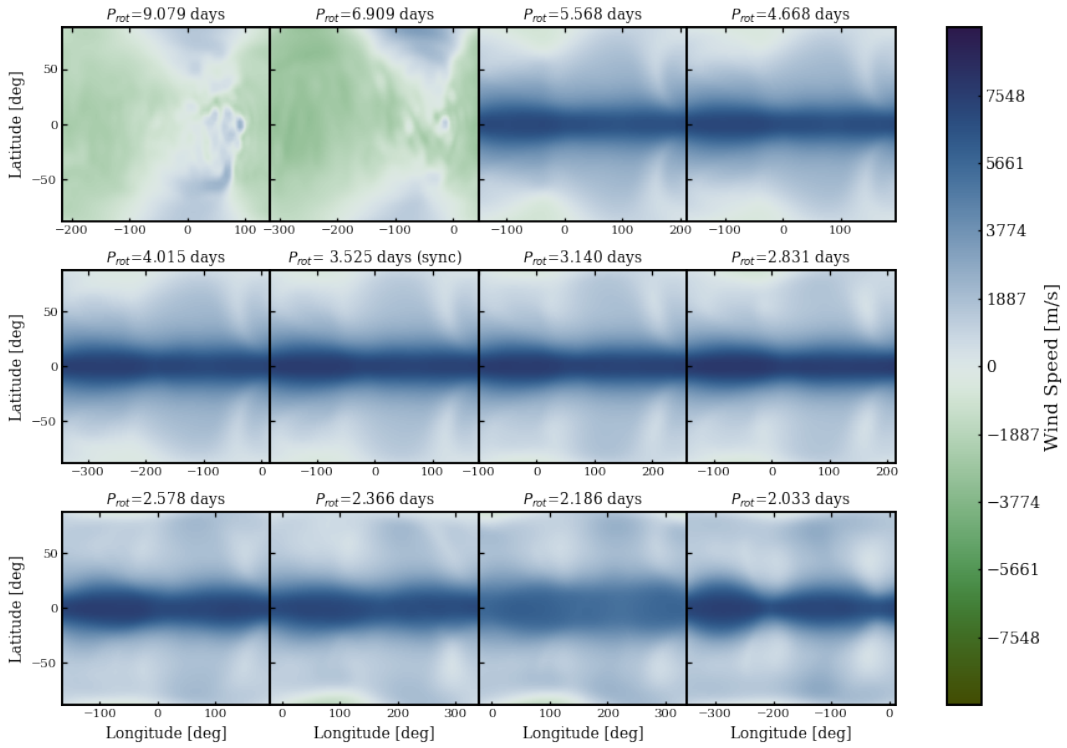

Figure 2.15 Maps of the winds in the east-west direction (with eastward defined as positive values) at the infrared photosphere (P=65 mbar) of the planet, for our full suite of General Circulation Models. Each map is oriented to be centered on the substellar point. Most models show the standard eastward equatorial jet, but the two most slowly rotating models have no coherent equatorial jet and instead have westward flow near the substellar point and across most of the planet.

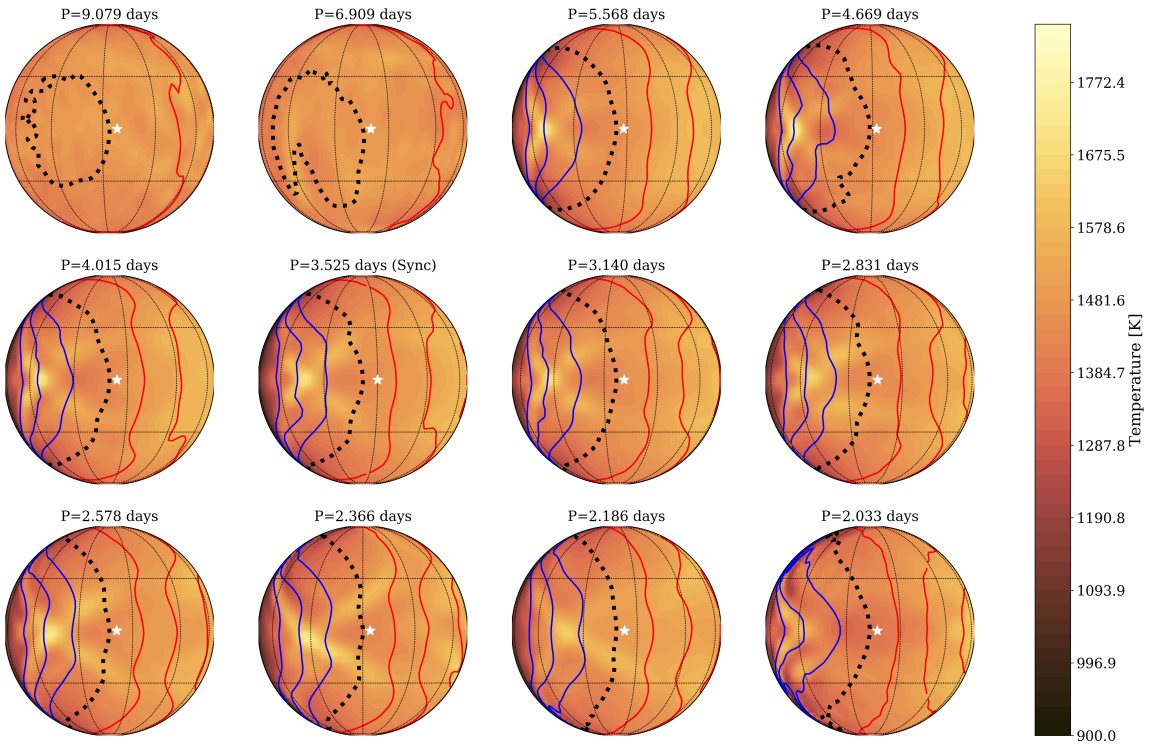

Figure 2.16 Orthographic projections of the temperature structure for 12 different rotation rates shown at the atmospheric level responsible for the the strongest absorption lines in the post-processed spectra, orientated such that the subobserver point is centered. Red and blue contours show constant line of sight velocities at 2, 4, and 6 km/s. The black dotted contour shows 0 km/s line of sight and the white star shows the substellar point. Aside from the models experiencing a disrupted flow pattern—corresponding to the slowest two rotation rates—the temperature structure and circulation pattern are fairly similar over different rotation rates. Even though the rotation rate of the planet is increasing, the winds are decreasing in strength in such as way that results in similar line of sight velocity patterns across the models. We also see that these line of sight velocity patterns are not symmetric and are influenced by the underlying wind structure.

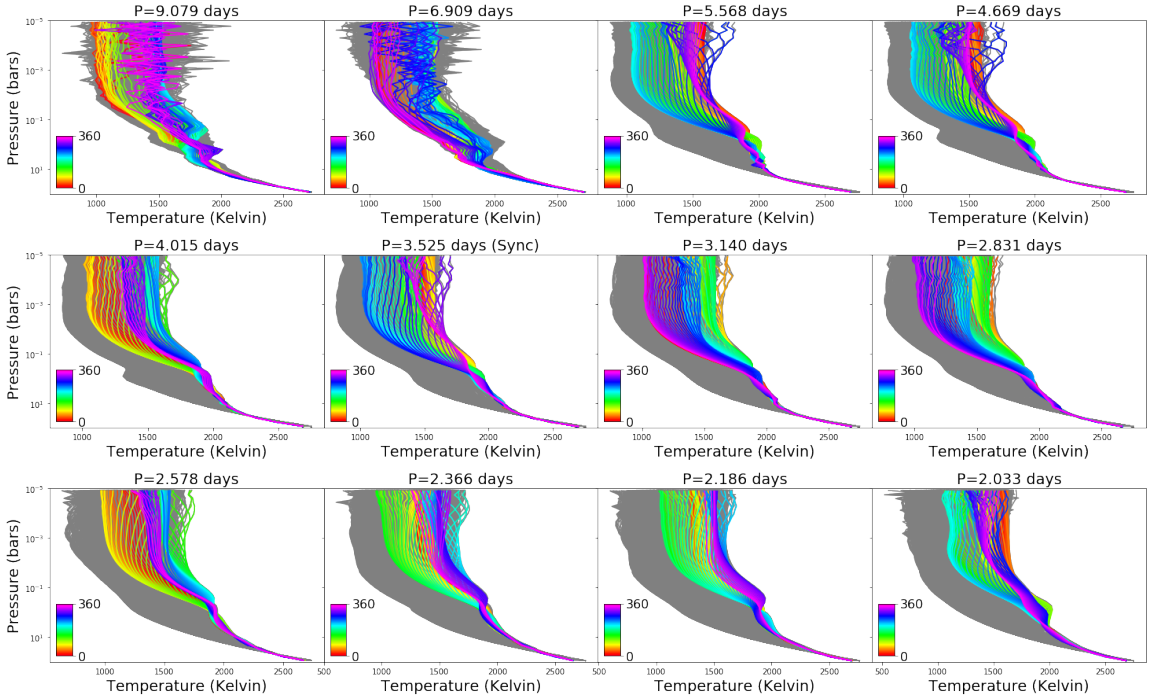

Figure 2.17 Temperature pressure profiles for the suite of models examined. Similar to Figure 5, the grey profiles are from the entire planet. The rainbow lines show equatorial profiles. Since these rotation rates are not equal to the period, the subobserver and substellar longitudes are not constant. We report the subobserver longitudes, starting with the slowest rotator as: [210, 140, 320, 330, 170, 350, 100, 70, 170, 240, 260, 310] degrees. The numerical noise, seen most prominently in the upper atmospheres of the two slowest rotators, has little effect on the resulting spectra.

Table 2.4. Peak Detections for All Rotation Rates

	Chem EQ		Constant VMR	
Period (days)	CO only	CO and H_2O	CO only	CO and H_2O
9.079	5.57/5.57	3.01/2.95	5.51/5.51	5.31/5.29
6.909	5.74/5.70	3.00/2.92	5.54/5.50	5.54/5.47
5.568	6.03/5.97	3.93/3.28	5.37/5.29	6.50/6.23
4.669	6.05/6.02	3.91/3.26	5.20/5.13	6.59/6.28
4.015	6.01/6.00	3.92/3.16	5.33/5.12	6.73/6.23
3.525 (sync)	6.19/6.04	4.02/3.24	5.40/5.20	6.74/6.15
3.140	6.16/6.04	4.04/3.27	5.39/5.09	6.77/6.21
2.831	6.01/5.95	4.05/3.33	5.25/4.96	6.72/6.15
2.578	6.12/6.00	**4.22**/3.37	5.46/5.25	6.55/6.02
2.336	6.10/5.89	4.21/3.31	5.51/5.17	6.62/5.88
2.186	**6.49**/**6.40**	4.19/**3.39**	5.47/5.43	**6.87**/**6.37**
2.033	6.43/6.05	4.18/3.18	**6.03**/**5.72**	6.54/5.81

Note. — Peak detection for every 3D model examined with Doppler effects considered (first entry) and without (second entry). The highest detection for each chemistry and Doppler setting across all rotation rates is bolded and reported in Table 2.6. While the highest significance detections come from the more quickly rotating models, these values are only minimally above those for the synchronous model.

CHAPTER III

Exploring the Effects of Active Magnetic Drag in a General Circulation Model of the Ultrahot Jupiter WASP-76b (Beltz et al 2022a)

"We're all born naked and the rest is drag"

– RuPaul

3.1 Preface

Results in this chapter were published in: *Beltz, H., Rauscher, E., Roman, M., and Guillot, A., 2022a. Exploring the Effects of Active Magnetic Drag in a General Circulation Model of the Ultrahot Jupiter WASP-76b. The Astronomical Journal, 163, 35* and are reproduced here with minor style revisions by permission of the American Astronomical Society under the non-exclusive right of republication granted to authors.

3.2 Abstract

Ultra-hot Jupiters represent an exciting avenue for testing extreme physics and observing atmospheric circulation regimes not found in our solar system. Their high temperatures result in thermally ionized particles embedded in atmospheric winds interacting with the planet's interior magnetic field by generating current and experiencing bulk Lorentz force drag. Previous treatments of magnetic drag in 3D General Circulation Models (GCMs) of ultra-hot Jupiters have mostly been uniform drag timescales applied evenly throughout the planet, which neglects the strong spatial dependence of these magnetic effects. In this work, we apply our locally calculated active magnetic drag treatment in a GCM of the planet WASP-76b. We find the effects of this treatment to be most pronounced in the planet's upper atmosphere, where strong differences between the day and night side circulation are present. These circulation effects alter the resulting phase curves by reducing the hotspot offset and increasing the day-night flux contrast. We compare our models to *Spitzer* phase curves which imply a magnetic field of at least 3 G for the planet. We additionally contrast our results to uniform drag timescale models. This work highlights the need for more careful treatment of magnetic effects in atmospheric models of hot gas giants.

3.3 Introduction

Gas giant planets orbiting extremely close to their host stars make excellent targets for observers due to their favorable planet-star flux ratios and offer avenues for testing prescriptions of high-temperature physical processes in theoretical models. The quintessential category of these planets is ultra-hot Jupiters (UHJs), which orbit so close to their host star that their equilibrium temperatures exceed $\sim$2200 K. The extreme temperatures of these planets warrant a careful consideration of the relevant physical processes included in the models, as the increased irradiation results in differ-

ent dominant mechanisms than those of their cooler cousins, "normal" hot Jupiters. While magnetic effects may begin to alter the circulation patterns of gas giant planets that reach temperatures $\approx$ 1500 K (*Menou*, 2012; *Rogers and Komacek*, 2014), it is not until planets reach an equilibrium temperature $\gtrsim$ 2000 K that non-ideal MHD effects are predicted to become very strong due to the coupling between the circulation and atmospheric magnetic field, potentially resulting in effects such as hot spot reversals (*Hindle et al.*, 2021b). Since no solar system analogue exists for these planets, intricate multi-dimensional atmospheric modeling is critical for understanding and interpreting observations of their atmospheres.

The consequences of magnetism manifest themselves on hot gas giants in a multitude of ways. The interior of the planet is expected to host a magnetic field of comparable or even greater strength than solar system Jovian planets (*Yadav and Thorngren*, 2017). In the planet's upper atmosphere, high energy stellar photons can photo-ionize species and drive evaporative winds, whose outflow can be shaped by the planet's magnetic field (*Owen and Adams*, 2014). Here, we focus on the atmospheric effects of thermal ionization of species near the planet's photosphere interacting with the planet's magnetic field. Due to the extreme temperatures on the daysides of these planets, species undergo thermal ionization while remaining embedded in the mostly neutral atmosphere; these ions then are advected around the planet via strong winds. The currents generated by this interaction could travel into the planet's interior and deposit heat there via Ohmic dissipation, perhaps explaining the inflated radii of many hot Jupiters (*Batygin and Stevenson*, 2010; *Perna et al.*, 2010b; *Thorngren and Fortney*, 2018). The coupling between the ions and the mostly neutral winds results in a bulk Lorentz force drag, potentially reducing circulation efficiencies and increasing the day-night contrast (*Perna et al.*, 2010a; *Menou*, 2012; *Batygin et al.*, 2013; *Rauscher and Menou*, 2013; *Rogers and Showman*, 2014). Current treatment of magnetic effects in 3D atmospheric models vary in complexity, from computationally

expensive non-ideal MHD simulations to the use of a universal drag timescale applied throughout the planetary atmosphere, with this range in modeling complexity serving a variety of purposes.

Perna et al. (2010a) introduced the idea of parameterizing the effects of the bulk Lorentz force on atmospheric winds with a drag timescale. The formulation of this timescale was derived from order of magnitude approximations of the terms in the non-ideal MHD induction equation in the hot Jupiter regime, thus effectively operating as a "kinematic" MHD model. This timescale was used in *Rauscher and Menou* (2013) in their models of two different hot Jupiters. This work found that for the hotter planet modeled, (HD 209458b, $T_{\rm eq} \approx 1500$ K), the drag prescription resulted in slower wind speeds and a reduction in the strength of the equatorial jet often seen in hot Jupiter atmospheric models.

One simpler treatment for magnetic drag is applying a uniform drag timescale to the entire modeled atmosphere. *Komacek and Showman* (2016) explored the use of various uniform values for their model of a HD 209458b-like hot Jupiter to approximate the effect of Lorentz forces. So long at the drag timescale was short enough ($\lesssim 10^4$s), the zonal jet was eliminated and day-night temperature differences were large. Additionally, they noted that their drag timescale had only a secondary effect on the day-night temperature contrast when it was longer than the rotation rate of the planet. Uniform drag timescales are found in many works involving GCMs of hot (or ultra hot) Jupiters (*Komacek et al.*, 2017; *Koll and Komacek*, 2018; *Kreidberg et al.*, 2018; *Mansfield et al.*, 2018; *Arcangeli et al.*, 2019). These universal drag timescales can be converted to global magnetic field strengths with order-of-magnitude estimates, such as in *Kreidberg et al.* (2018), which estimated a magnetic field stronger than ~ 1 Gauss for the UHJ WASP-103b. This uniform drag treatment will also have an effect on the predicted phase curves of the planet, as shown in *Tan and Komacek* (2019). The resulting phase curves of their modeled planets had

smaller offsets and larger amplitudes when the atmospheric drag was stronger. This means that increasing the strength of the drag resulted in hotter daysides and cooler nightsides on the planet as well as reduced the eastward shift of the planet's hotspot, as should be expected.

A limitation of universal drag timescales is that they do not allow for spatial variation in drag strength between the hot day and cold nightside of the planet: given the hundreds of Kelvin temperature contrasts, the magnetic resistivity should vary by many orders of magnitude, so we should expect effective magnetic timescales to also vary by orders of magnitude for a single pressure level (*Rauscher and Menou*, 2013). Uniform drag timescales also do not account for the directional dependence of magnetic drag: assuming the planet's deep-seated magnetic field is a dipole, only winds in the east-west direction should experience Lorentz drag(*Perna et al.*, 2010a).

The most complex treatments of magnetism in the atmosphere of a hot gas giant involve the use of magnetohydrodynamic (MHD) models. *Rogers and Showman* (2014) introduced the first non-ideal MHD simulation of a hot Jupiter. The authors compared the Lorentz force from their MHD simulations to the active magnetic drag timescale prescription from *Rauscher and Menou* (2013). Their Lorentz force peak value was within an order of magnitude of the timescale prescription, but the spatial extent of their Lorentz force was more localized. In a follow up paper, *Rogers and Komacek* (2014) ran a grid of MHD hot Jupiter models and found that time variability becomes important at the higher temperatures modeled (1400-1800 K) pointing to the intrinsic importance of feedback between magnetism and the planet's thermal structure. In the UHJ regime, *Rogers* (2017) offers the closest instance of a physically consistent non-ideal magnetohydrodynamic treatment of an UHJ. This work, focused on HAT-P-7b, highlighted the complexity of dynamic magnetic field lines and estimated the minimum global magnetic field strength of the planet to be 6 Gauss, based on comparison to observed phase curve variability for this planet (*Armstrong et al.*,

2016). This minimum field strength of 6 Gauss is also inferred from shallow-water magnetohydrodynamic models from *Hindle et al.* (2019).

Magnetism is not the only high-temperature physical process of note in these planets. If high enough temperatures are reached on the dayside of UHJs, H_2 is expected to dissociate, which results in a local cooling effect as dissociation requires an input of energy. As winds transport the gas to the nightside of the planet, the temperatures can drop enough that recombination occurs, locally heating the atmosphere and reducing the day-night temperature contrast (*Bell and Cowan*, 2018). In *Tan and Komacek* (2019), the authors investigated the effects of molecular hydrogen dissociation and recombination, in addition to the presence of uniform drag, across a range of planetary equilibrium temperatures. Their work found that beginning near $T_{eq} = 2200$ K, the dissociation and recombination of hydrogen begins to play a significant role in the circulation of the atmosphere. Including hydrogen dissociation decreased the strength of the equatorial jet, which disappeared at the highest equilibrium temperature examined ($T_{eq} = 3600$). Overall, including molecular hydrogen dissociation and recombination reduced the day-night temperature contrast, reducing the predicted phase curve amplitude.

Beyond H_2, there are other molecular species whose dissociation has significant impact on the atmospheric structure of UHJs by changing the main sources of opacity. *Parmentier et al.* (2018) describes the influence of thermal dissociation and ionization of a variety of species including H_2O and H^- on the thermal and spectral properties of UHJs, using four UHJ models made from SPARC/MITgcm. (The only main molecular opacity source that did not dissociate anywhere in the UHJ atmospheres was CO.) These models showed stark differences between day and nightside temperatures and abundances. They found dissociation of water and presence of H^- opacity may result in muted of spectral features. Additionally, when included as an opacity source, H^- increases the optical depth across all wavelengths, causing the photosphere to move

to a lower pressure (*Lothringer et al.*, 2018).

Many UHJs exhibit what are known as temperature inversions—portions of the atmosphere that increase in temperature with decreasing pressure, opposite to standard behavior. These hot upper atmosphere inversions are likely due to high altitude optical/UV absorbers, such as TiO/VO (*Hubeny et al.*, 2003; *Fortney et al.*, 2008) or Fe, SiO, and metal hydrides (*Lothringer et al.*, 2018; *Gibson et al.*, 2020), but high C/O ratios (*Mollière et al.*, 2015) or inefficient IR cooling (*Gandhi and Madhusudhan*, 2019) could also play a role. The strength of this inversion may also scale with stellar host type (*Baxter et al.*, 2020). Additionally, temperature inversions on UHJs are spatially inhomogeneous, as the stratospheric heating on the dayside will be absent from the shadowed nightside (*Kreidberg et al.*, 2018).

Due to the high temperatures of the daysides of UHJs, clouds are expected to be mostly constrained to the nightside of the planets. Recently, *Roman et al.* (2021) explored cloud effects in our GCM for a variety of irradiation temperatures, including UHJs. This work found that in the UHJ regime ($T_{irr} > 3250K$),[1] clouds were restricted to the nightside at high latitudes and were absent near the equator globally. Using a more complex cloud microphysics model, the GCM from *Mansfield et al.* (2018) was post-processed in *Helling et al.* (2019b), which concluded that some clouds would exist on the nightside of the UHJ HAT-P-7b and the dayside could host some very optically thin clouds, away from the equator. Their similar analysis of WASP-18b in *Helling et al.* (2019a) also found a cloud-free dayside and heterogeneous clouds on the nightside. As far as hazes are concerned, *Helling et al.* (2020) showed that the dayside of all UHJs are too hot for hydrocarbon hazes to be stable and that these hazes should play no role in the aerosol opacities on the nightside and terminator region.

One particularly interesting UHJ is WASP-76b. First detected by *West et al.*

[1] A planet's irradiation temperature is related to its (zero-albedo) equilibrium temperature as: $T_{\rm irr} = 4^{1/4} T_{\rm eq}$.

(2016), WASP-76b is an inflated ultra-hot Jupiter orbiting every 1.81 days with an equilibrium temperature just over 2200 K. Since its detection, a broadened sodium feature was detected in transmission spectra by *Seidel et al.* (2019), hinting at the super-rotation of the upper atmosphere. The sodium detection was confirmed shortly after in *Žák et al.* (2019). *Ehrenreich et al.* (2020) detected Fe absorption in transmission spectra from one side of the planet's terminator but not the other, which was interpreted as evidence for nightside condensation of the species. This detection was later confirmed by *Kesseli and Snellen* (2021a). Recent work from *Wardenier et al.* (2021) suggests that this differential absorption could instead be explained by a strong temperature difference on the trailing and leading limb of the planet, without needing to invoke iron condensation. *Fu et al.* (2020) additionally detected TiO and H_2O in transmission spectra form *HST* and *Spitzer*. From the emission spectra of the planet, CO emission features are present and their models suggested a temperature inversion of $\sim 500K$. HST emission and transmission spectra also suggests the presence of TiO, H_2O, and thermal inversions (*Edwards et al.*, 2020). Tentative detections (4σ) of VO also exist (*Tsiaras et al.*, 2018).

Perhaps due to their difficulty to model, (as a result of their extremely short radiative and dynamic timescales, in addition to the complicating physics discussed above) only a handful of GCMs for UHJs have been published. Because atmospheric dynamics will manifest in observables, 3D GCMs are useful in interpreting the spectra, (such as HAT-P-7b in *Mansfield et al.*, 2018) phase curves, (such as the case of WASP-103b in *Kreidberg et al.*, 2018) or both (see WASP-18b from *Arcangeli et al.*, 2019). A common theme that arises from these works is that the GCM had difficulty reproducing UHJs with very low heat redistribution, which could potentially be due to an underestimation of magnetic drag strength, uncertainties surrounding dissociation effects, or warming from nightside clouds. When additional sources of drag are included, the resulting phase curves produced by the GCM in the works referenced

above are a better match to observed values.

In this work, we explore the effects of active magnetic drag in our GCM of the UHJ, WASP-76b. Although all of the physical processes mentioned above are no doubt present to some degree on WASP-76b, we choose to not include clouds or H_2 dissociation effects at this time to focus solely on the influence of active magnetic drag in the planet's atmosphere. Future work is necessary to characterize the mutual interactions between these physical processes for UHJs. Based on observational constraints on the strength of the temperature inversion in this planet's atmosphere (*Fu et al.*, 2020), we set up our model to include this stratosphere. In Section 3.4, we describe our GCM and the active magnetic drag treatment. In Section 3.5, we examine the atmospheric structures of our models with and without the active magnetic drag treatment. We additionally compute models featuring a universal drag timescale and compare the atmospheric effects of the two different treatments of magnetic drag. In Section 3.6, we contextualize our results and discuss the limitations of our models. Finally, in Section 3.7 we summarize the main points of this work.

3.4 Methods

General Circulation Models (GCMs) are three-dimensional numerical tools that simulate the underlying physics and circulation patterns of planetary atmospheres. To do this, GCMs solve the simplified set of fluid dynamics equations known as the primitive equations of meteorology. We use the GCM from *Rauscher and Menou* (2012) with the updated radiative transfer scheme in *Roman and Rauscher* (2017) (based on *Toon et al.*, 1989). Our GCM solves the radiative transfer with a double-gray treatment, meaning that two absorption coefficients are used: one in the visible wavelength regime to account for absorption from the host star and one in the infrared regime for the planet's thermal emission. The nuances of atmospheric implications for doubley-gray radiative transfer versus more complex treatments, such as correlated-

k or picket fence methods, are beyond the scope of this work. Interested readers are directed to the recent paper from *Lee et al.* (2021) that explores in depth the consequences of these different radiative transfer schemes. We modeled the planet with 65 vertical layers evenly spaced in log pressure over 7 orders of magnitude from the bottom boundary of 100 bars, at a horizontal spectral T31 resolution (roughly 4 degrees at the equator) and the parameters listed in Table 4.4.1. Our absorption coefficients were informed by *Fu et al.* (2020); by changing the ratio of the infrared and visible coefficients, our resultant atmosphere will have an inverted temperature profile at locations that are highly irradiated.

Due to the increased difficulty of modeling planets in the ultra-hot regime, where heating rates are stronger and winds can be faster, we added sponge layers to the top three layers of all the models presented for numerical stability purposes. Sponge layers act as a damping mechanism in the top of atmospheric models to reduce the buildup of artificial noise brought about by atmospheric waves reflecting off of the top boundary of the model (*Forget et al.*, 1999; *Wills and Schneider*, 2016). The strength of these sponge layers decreases with height, with the strongest drag being applied in the top layer and then linearly decreasing with log pressure. By restricting the sponge layers to the top few levels, we leave the rest of the atmosphere unaffected. In our initial investigations, we found that after 1000 orbits were completed, the overall kinetic energy in the sponge layers was decreased by a factor of a few percent, and below the sponge layers, the change was even smaller. This is the first time sponge layers have been used in our GCM, but sponge layers are relatively common and have been implemented in other exoplanet GCMs (see *Mayne et al.*, 2014; *Deitrick et al.*, 2020; *Wang and Wordsworth*, 2020, for examples).

Table 3.1. WASP-76b Model Parameters

Parameter	Value
Planet radius, R_p	1.31×10^8 m
Gravitational acceleration, g	6.825 m s^{-2}
Orbital Period	1.81 days
Orbital revolution rate, $\omega_{\rm orb}$	4.018×10^{-5} s^{-1}
Substellar irradiation, $F_{\rm irr}$	5.14×10^6 W m^{-2}
Planet internal heat flux, $F_{\rm int}$	3500 W m^{-2}
Optical absorption coefficient, κ_{vis}	2.4×10^{-2} cm^2 g^{-1}
Infrared absorption coefficient, κ_{IR}	1×10^{-2} cm ^{2} g^{-1}
Specific gas constant, R	3523 J kg^{-1} K^{-1}
Ratio of gas constant to heat capacity, R/c_p	0.286

3.4.1 Our Magnetic Drag Treatment

Our model's implementation of magnetic drag is unique among GCMs as it is calculated based on local atmospheric conditions and applied in a geometrically and energetically consistent way. The physical origin of this drag comes from thermally ionized particles interacting with the planet's magnetic field due to strong (mostly neutral) winds advecting the particles across the planet. From the atmosphere's perspective, the wind feels a bulk Lorentz drag force. We choose to model the case of a dipole field aligned with the planet's rotation axis as a simplifying assumption, because detailed information about the shape of exoplanet's magnetic field lines is not currently known. Additionally, we fix the shape of the magnetic field lines and assume the local field strength does not vary as a function of radius in the model. Our prescription for magnetism stands out from other GCMs because we use an active magnetic drag timescale; that is, one that is locally calculated and updated throughout the simulation to model the effects of magnetism in the planet's atmosphere. We can refer to this framework as a "kinematic" MHD framework. The critical assumption with this treatment is that we are assuming the dipolar magnetic field, generated

in the planet's interior, is much stronger than any field induced in the atmosphere. As a result of this assumption, we apply the drag only in the zonal (east-west) direction. This assumption remains reasonable when the magnetic Reynolds number is less than 1 (*Menou*, 2012; *Hindle et al.*, 2021b,a). The magnetic Reynolds number can be approximated with $R_m \approx \frac{UH}{\eta}$(*Hindle et al.*, 2021a) where U is the zonal wind speed, H is the pressure scale height, and η is the magnetic resistivity. In this work, we calculate resistivity in the same way as *Menou* (2012):

$$\eta = 230\sqrt{T}/x_e \text{ cm}^2 \text{ s}^{-1}. \tag{3.1}$$

We calculate the ionization fraction, x_e, using the Saha equation, taking into account the first ionization potential of all elements from hydrogen to nickel (as in *Rauscher and Menou*, 2013). As shown on the left in Figure 3.1, $R_m < 1$ for the majority of temperatures and pressures found in our model, implying that our assumptions are reasonable for much of the atmosphere, although we may be missing more complex behavior in the hottest dayside regions of the upper atmosphere. Although this is a simplification of non-ideal atmospheric MHD effects, it nevertheless represents a reasonable starting point for exploring the effects of active magnetic drag and is more complex than the uniform drag timescales applied in other GCMs.

Our model also has unique advantages compared to current non-ideal MHD simulations in the low magnetic Reynolds number regime. In models such as those found in *Rogers and Komacek* (2014), magnetic resistivity is calculated from a static, horizontally homogenous (no latitude or longitude dependence) initial temperature profile. Other work, such as *Rogers* (2017), calculates resistivity based on a static temperature profile with horizontal variations, but does not change as the simulation runs and local temperature conditions change. Our GCM calculates this resitivity locally and often, allowing the resitivity to evolve temporally in a more self consis-

tent manner. By doing this, our resistivity varies by many orders of magnitude from the dayside to the nightside for a single pressure level and updates as the model progress, allowing for feedback with the atmospheric thermal structure. Additionally, our model is coupled with double-gray radiative transfer equations. Current non-ideal MHD models lack this radiative transfer coupling and instead employ a Newtonian relaxation for radiative forcing, a simplified scheme where the temperatures relax toward a prescribed profile at a chosen timescale (*Rogers and Showman*, 2014; *Rogers and Komacek*, 2014). Finally, our model's dynamical core does not have any explicit viscosity in the momentum equations, as atmospheres are generally highly inviscid. Because current non-ideal MHD models such as those discussed above have heritage in dynamo/interior models with explicit viscosity in the solved equations, their resulting wind speeds are up to an order of magnitude weaker than expected from inviscid GCMs in the hot Jupiter regime.

As described in detail in *Rauscher and Menou* (2013) and shown in Equation 5.1, the magnetic drag is applied by subtracting U/τ_{mag} from the east-west momentum equation, where the magnetic timescale is calculated locally as:

$$\tau_{mag}(B, \rho, T, \phi) = \frac{4\pi\rho\ \eta(\rho, T)}{B^2|sin(\phi)|} \tag{3.2}$$

where B is the chosen global magnetic field strength, ϕ is the latitude, ρ is the density. The kinetic energy lost as a result of this drag is then returned to the atmosphere as localized ohmic heating in the energy equation as $\frac{U^2}{\tau_{mag}}$, for both the active drag discussed here and uniform drag models discussed below. This local treatment of magnetic drag allows the magnetic timescale to vary by many orders of magnitude throughout the entire planet without being as computationally expensive as solving the full non-ideal MHD equations. Additionally, this treatment updates the timescales as the model progresses, allowing feedback between the magnetic effects

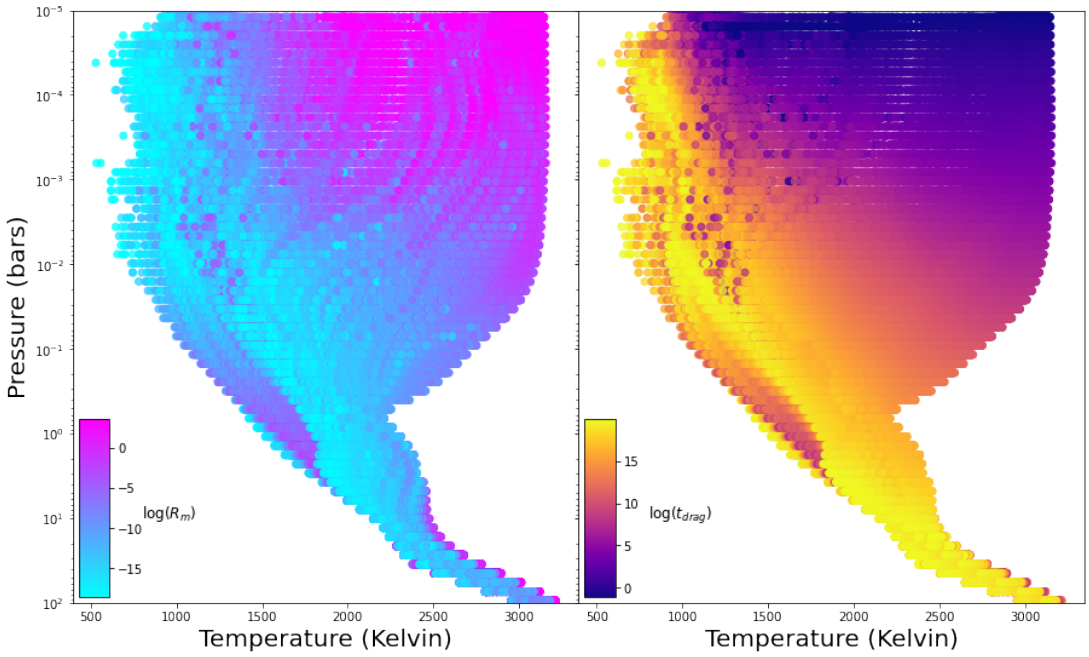

Figure 3.1 Magnetic Reynolds number for the 3 G model of WASP-76b *(left)* and the magnetic drag timescales *(right)* based on the atmospheric structure at the end our simulation. Our kinematic MHD framework is appropriate where $R_m < 1$, which is the case for the majority of the atmosphere. The hottest regions on the dayside upper atmosphere, where R_m is the largest, is where atmospheric circulation can induce a magnetic field component comparable to the global field strength. On the right, we show the range in values for our active drag timescale. Across a single pressure level, the magnetic drag timescale can vary by many orders of magnitude. Since our magnetic drag varies with latitude, a single temperature and pressure will have a range of timescales which explains the non-monotonic behavior in portions of the plot.

and the atmosphere's thermal structure. Figure 3.1 (right) shows the magnetic drag timescales across the atmosphere's temperature and pressure space from our 3 G model of WASP-76b. Across a single pressure level in the upper atmosphere, our magnetic drag timescale can vary by nearly 15 orders of magnitude. The shortest magnetic timescales are located on the dayside of the upper atmosphere, due to the high temperatures and low densities. Deeper in the atmosphere, where the density is greater, the timescales are longer and the effect of our magnetic drag on the circulation pattern will be smaller. This large variation in magnetic drag strength highlights the versatility of our active, locally calculated drag treatment.

Both τ_{mag} and R_m^{-1} scale linearly with the magnetic resistivity and so in Figure 3.1 we see some correlation between the two. However, the other physical variables that factor into the magnetic Reynolds number and drag timescale mean that they do not trace each other exactly. For example, almost all of the regions with $R_m > 1$ also have $\tau_{mag} < 10^5$ s, but there are locations with $\tau_{mag} = 10^5$ s that have R_m values as low as 10^{-10}. Even the shortest drag timescales, $\tau_{mag} \sim 1$ s, can exist in regions with $R_m \sim 10^{-2}$, although generally those timescales are found in regions with $R_m \geq 1$.

We ran our model of WASP-76b for variety of different magnetic field strengths: 0 G, 0.3 G, 3 G, and 30 G to encompass the field strengths measured in our solar system and to explore the range of effects our magnetic treatment will have on our modeled atmospheres. We additionally ran two instances of a uniform drag with timescales equal to 10^4 and 10^7 seconds following the GCMs in *Tan and Komacek* (2019). All of these models were calculated for 2000 orbits, to allow the atmosphere enough time for winds to accelerate (starting from rest) and reach a steady state.

3.5 Results

3.5.1 The Base Case: No Magnetic Effects

To understand the effects of magnetic drag on our models of WASP-76b, we begin by examining the "base" case atmosphere, free of magnetic drag through a snapshot of the atmospheric structure taken from the end of the simulation. Also, since this is the first planet with a forced inverted temperature profile we have published with this GCM, we will examine the extent and effects of the temperature inversion. Overall, our model of WASP-76b exhibits the typically expected hot Jupiter flow patterns seen in our previous works (e.g., *Rauscher and Menou*, 2013; *Beltz et al.*, 2021; *Roman et al.*, 2021). These features include a strong, eastward equatorial jet present in the deeper atmosphere (Figure 3.4) and an eastward advected hotspot. Figure 3.2 shows

the temperature-pressure profiles for the planet as well as the 1-D profile we use globally to initialize the simulation and theoretical 1-D averages (based on *Guillot*, 2010). From this figure, a few things are apparent. First, our model shows a large (>1500 K) day-to-night temperature contrast along the equator. This is in broad agreement with the $\sim$ 1440K brightness temperature contrast measured from *Spitzer* phase curves at 4.5 μm (*May et al.*, 2021).

Second, while the temperature inversion must disappear on the nightside, as there is no stellar flux to be absorbed at high altitude, the east and west terminators are markedly different in the temperature inversions at those locations (roughly yellow and blue lines in Figure 3.2, respectively). Because low pressures heat and cool rapidly, the upper atmosphere temperatures are more similar at each terminator. The dominant eastward direction of the winds means that at deeper pressures the east terminator remains warm from gas heated on the dayside, while the west terminator has colder air advected around from the nightside.

Aside from the inverted temperature profile itself, another notable difference between this model and previous models with our GCM of non-inverted hot Jupiters is the decreased frequency and strength of chevron-shaped temperature features. These features are a result of vertical motions caused by converging winds, which heats the atmosphere in the chevron-shaped pattern (e.g., *Rauscher and Menou*, 2010) and can can result in the hottest spot on particular pressure levels to be east *or west* of the substellar point (e.g., *Beltz et al.*, 2021). In our model of WASP-76b however, these chevron features are weak enough that the hottest point stays east of the substellar point at all pressures (Figure 3.3) and the chevron features are less prominent than in our non-inverted models.

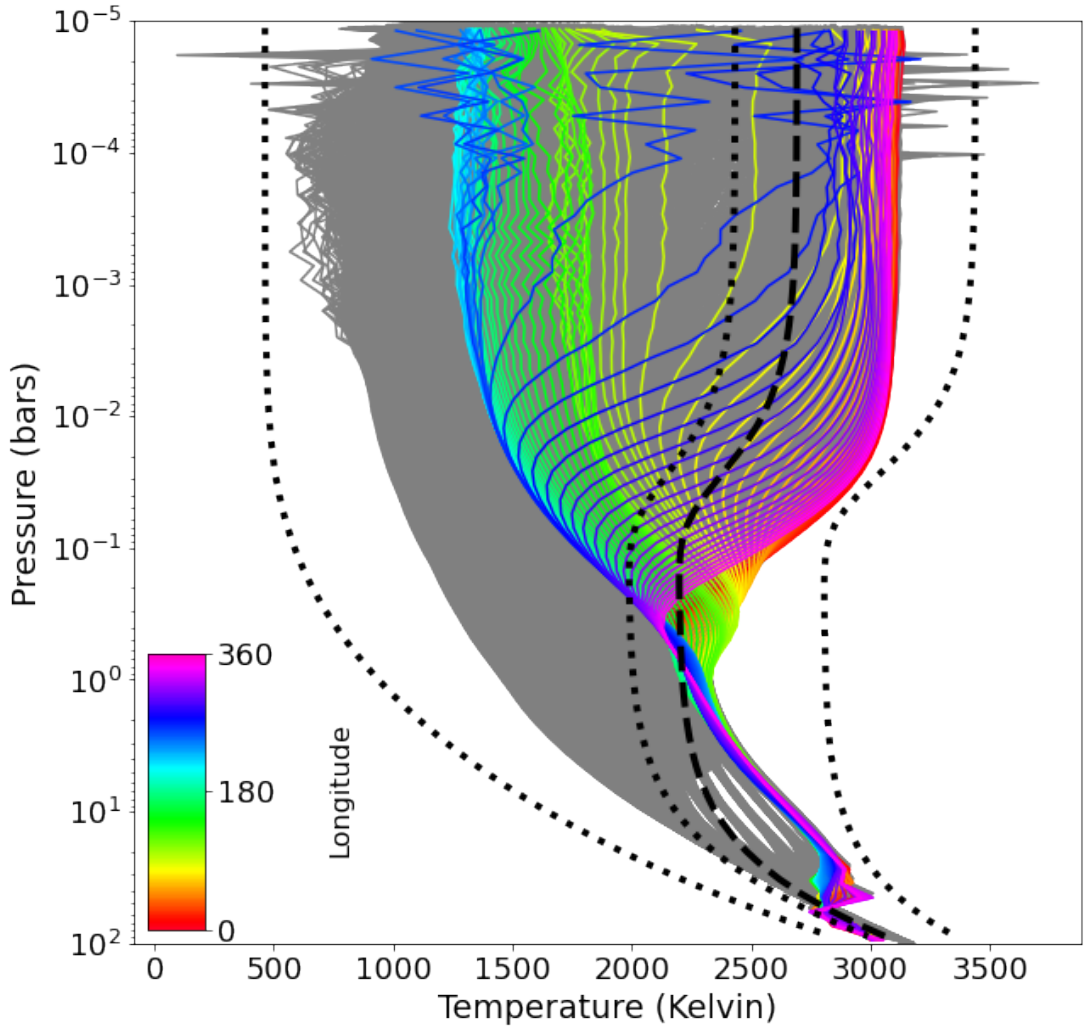

Figure 3.2 Temperature-pressure profiles for the non-magnetic model of WASP-76b. The rainbow lines show equatorial profiles (with longitude measured from the sub-stellar point) while the gray curves show profiles from the entire planet. From right to left, the black dotted curves show the substellar, global, and nightside averaged analytic 1D profiles calculated via *Guillot* (2010). The dashed black line is the profile used to initialize conditions globally. A strong temperature inversion is present on the day side, which becomes non-existent on the un-illuminated nightside. The large day-to-night temperature contrast is also apparent.

3.5.2 The Magnetic Models

We can now begin to look at the differences between our active magnetic drag models and our drag-free models. Figure 3.3 shows horizontal temperature maps for these scenarios at various depths in the atmosphere. The wind fields are overlaid in white stream lines. The differences between the non-magnetic models and magnetic models are most stark at the lowest pressures. The wind fields on the dayside of the magnetic models only flow in the north-south direction. This is because our magnetic drag is applied *only* to the east-west momentum equation (see Section 3.4.1). At this low pressure and high temperature regime, the magnetic timescales are very short, even for the smallest magnetic field strength tested. This causes the elimination of east-west momentum, leaving only the weaker north-south wind vectors. As the pressure increases and we get deeper into the atmosphere, the choice of magnetic field strength results in more disparate atmospheric structures. At the second pressure level shown, P $\sim$ 1 mbar, the drag timescales become slightly longer, due to the increase in density. At this level, the weakest magnetic field, 0.3 G, shows some wind flowing in the east-west direction, but a majority of the flow remains in the north-south direction. The two strongest magnetic field cases on the other hand still show exclusively north-south flow.

Going deeper into the atmosphere still, this pattern continues. At $P \sim 0.01$ bar, the 0 G and 0.3 G cases are very similar because the magnetic timescales at this pressure level have become so large that there is only a weak influence on the flow. In the 0 G case, the equatorial jet is slightly stronger and broader. Additionally, the night-side vortices near $\pm 50^{\circ}$ latitude are more pronounced than the 0.3 G model. The 3 G and 30 G cases still predominately have north-south winds on their dayside because the increased field strength allows the timescales to remain short enough to strongly affect the flow. At $P \sim 0.1$ bar, the magnetic timescales become so long that only the strongest magnetic field tested shows a substantially different flow pattern than the

Table 3.2. Maximum Wind Speeds (km/s)

	0.1 mbar	1 mbar	0.01 bar	0.1 bar	1 bar
Active Drag Models					
0 G	11.72	9.92	9.13	7.81	6.21
0.3 G	12.44	8.96	6.66	5.65	4.30
3 G	*7.21*	*7.10*	5.82	4.14	2.71
30 G	6.52	4.89	4.47	2.72	0.86
Uniform Drag Models					
10^7s	12.83	9.19	6.74	4.40	1.68
10^4s	12.21	*7.97*	4.62	2.09	0.24

[a]Values in italics correspond to when the fastest winds are in the North-South direction. For all other models, the East-West winds are faster.

non-magnetic case. At this pressure level, the 0 G case hosts the strongest equatorial jet, which becomes weaker as the magnetic field strength increases. Increasing the magnetic field strength from 3G to 30 G switches the atmospheric circulation pattern from a global equatorial super-rotation found in all models $<$ 30 G, to a dayside dominated by day-night flow and nightside eastward equatorial flow. It is interesting that this eastward flow is maintained on the nightside, even though there is no longer eastward flow on the directly forced dayside. While we leave a detailed analysis of this flow pattern to future work, it is worth noting that such behavior is not found in models with uniform drag timescales.

The equatorial jet is also affected by the magnetic drag, as seen in Figure 3.4. The non-magnetic case has the strongest and deepest jet. When active drag is present, the jet is weakened, especially at low pressures. This can be explained by the low pressures hosting the shortest drag timescales, which inhibit east-west flow and instead directs day-to-night flow meridionally up and over the poles. The stronger the magnetic field, the weaker the corresponding jet. In the strongest magnetic field we tested, the jet

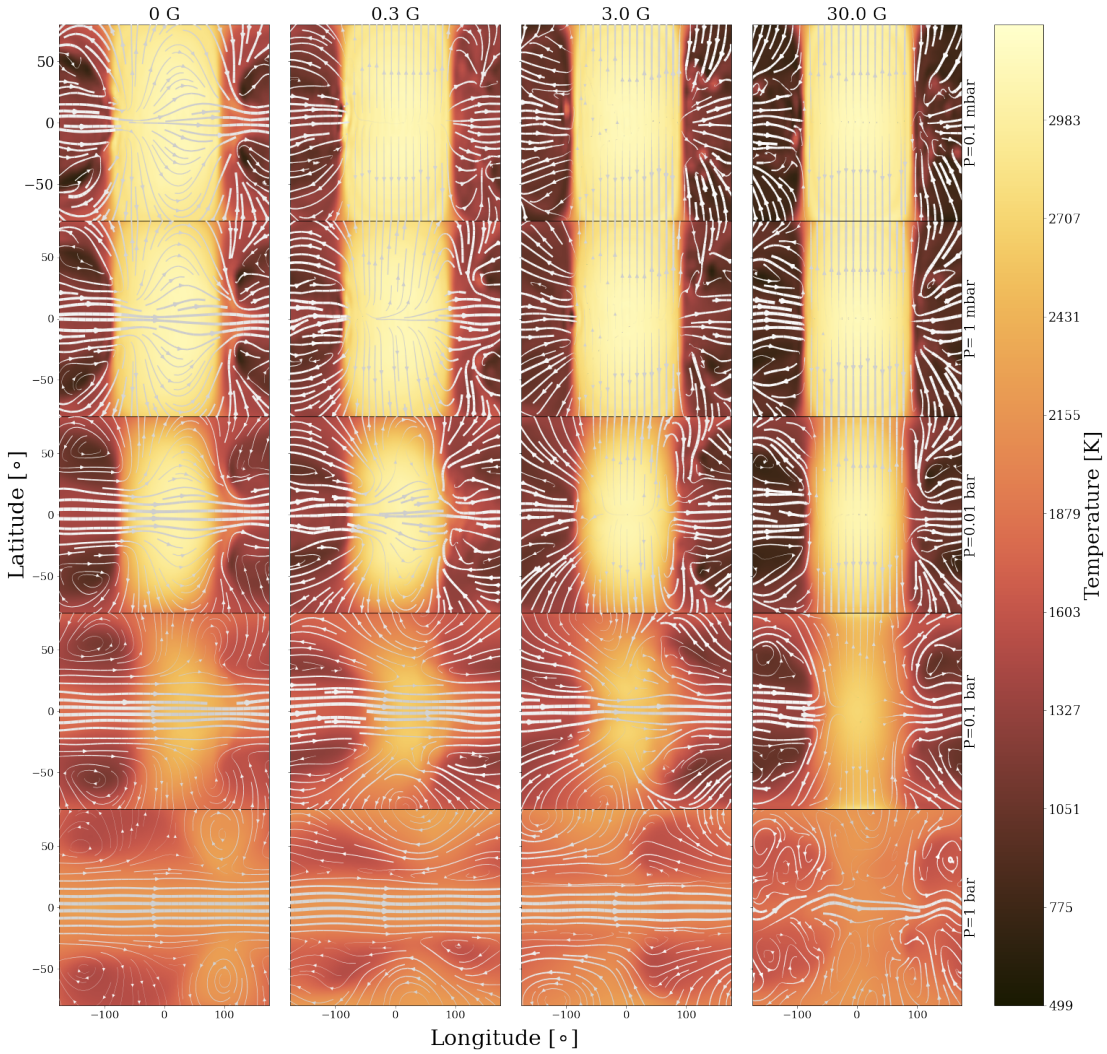

Figure 3.3 Maps of temperature and wind structure at several pressure levels (top to bottom: lowest to highest pressure) for each of the active magnetic drag cases studied (from left to right: increasing magnetic field strength). Each plot has the substellar point centered and the thickness of the wind vectors scale with the relative wind speeds; maximum wind speeds for each map are reported in Table 3.5.2. The effects of our active magnetic drag are most readily seen at the lowest pressure, where all the magnetic cases show exclusively north-south flow on the dayside, as the magnetic treatment has removed all the east-west momentum. As the pressure increases, the magnetic drag timescale also increases, reducing its effects. The stronger magnetic fields will have the shortest timescales and thus have the effects of magnetic drag present in deeper levels.

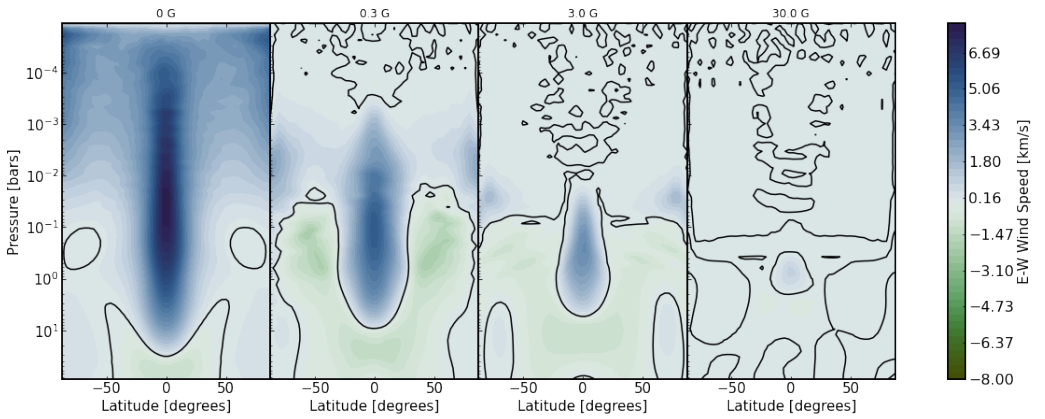

Figure 3.4 Longitudinally averaged east-west winds for the active magnetic drag cases studied. The black contours denote the boundary between positive (eastward) and negative (westward) winds. When the active magnetic drag is incorporated, the jet strength immediately diminishes, especially in the upper atmosphere. The stronger the magnetic field strength, the weaker the jet and the more it is constrained only to deeper pressure levels.

almost completely disappears. The reduction of the equatorial jet will result in less of an eastward shift of the planet's hotspot, meaning that the resulting phase curves will experience a smaller peak offset.

In Figure 3.5, we show the temperature-pressure profiles for all of our active magnetic drag models. To first order, these profiles share many properties: the hottest parts of the dayside exceed 3000K, temperature inversions occur on the dayside but not the nightside, and the inversion varies in strength between the two extremes, most notably near the terminators. We can see the influence of the active magnetic drag in the nightside equatorial profiles; as we increase the strength of the magnetic field, these profiles become colder. The models with magnetic drag also show more similarity between their east and west terminator profiles, in constrast to the non- or weakly-magnetic models where there is still significant eastward advection of hot gas on the dayside and cool gas from the nightside, leading to a warmer east terminator and cooler west side. Additionally, we see that at higher magnetic field strengths, the

temperature profiles in the lower atmosphere become more uniform. We note that the increase in magnetic field strength also increases the amount of large temperature jumps between layers (zig-zag like behavior). This may be due to variability in heating and cooling at smaller spatial/temporal scales thann our model resolves could result from the numerical dissipation being too weak in these uppermost layers (*Heng et al.*, 2011), although since the best numerical dissipation strength to use should likely vary over the conditions throughout the atmosphere (*Thrastarson and Cho*, 2011), increasing the dissipation in these upper layers would likely overdamp the higher pressure regions. This variability is especially present with the dark blue curves, corresponding to near the terminator west of the substellar region. Given the fact that this region lies at the boundary between stellar irradiation and no irradiation, it is not surprising that these profiles exhibit these characteristics, nor are they particularly worrisome.

3.5.3 Uniform Timescale Drag Cases

We additionally wanted to compare the effects of our active magnetic drag treatment with uniform drag timescale models. Following *Tan and Komacek* (2019), we ran our model of WASP-76b with uniform drag of timescales 10^4 and 10^7 seconds. As in our active magnetic drag models, we included sponge layers for the top three layers in these models for numerical stability. The resulting temperature-pressure profiles for uniform drag are shown in Figure 3.6. Overall, these profiles are relatively similar to each other, especially in the upper atmosphere. The lower atmosphere (below ~ 1 bar) becomes increasingly uniform in temperature for shorter drag timescales. In fact, due to the uniform application of magnetic drag, the shortest drag model is essentially a single temperature at each pressure level below $\sim$10 bars. We saw a similar effect in our active magnetic models, but to a lesser degree. Notably, for the model with the shorter uniform drag timescale (10^4 s), the thermal inversion is slightly stronger

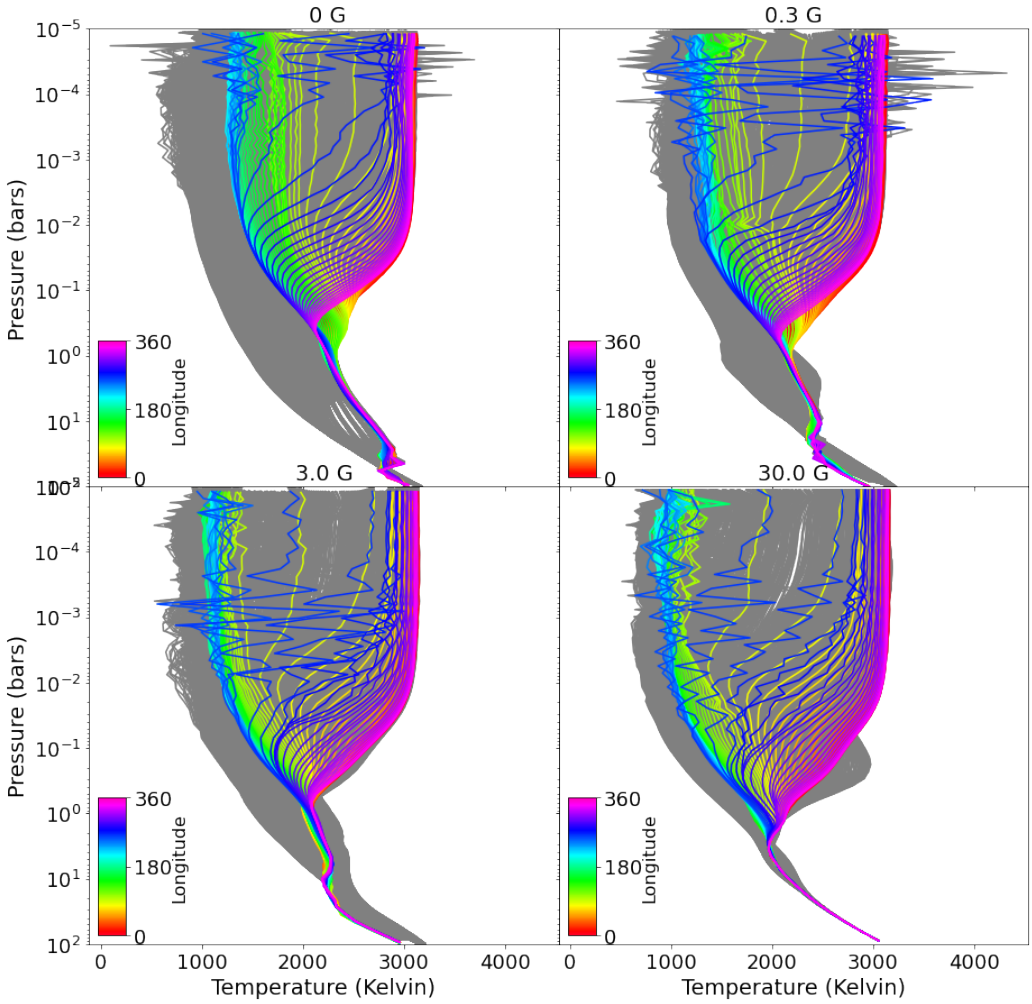

Figure 3.5 Temperature-Pressure profiles for our active magnetic models. The rainbow hues denote equatorial profiles, while the grey curves show profiles for the rest of the planet. All models show strong day-night contrasts and and temperature inversions on the daysides. The increase in magnetic field strength causes the nightside temperatures to decrease and the lower atmospheres to become more uniform.

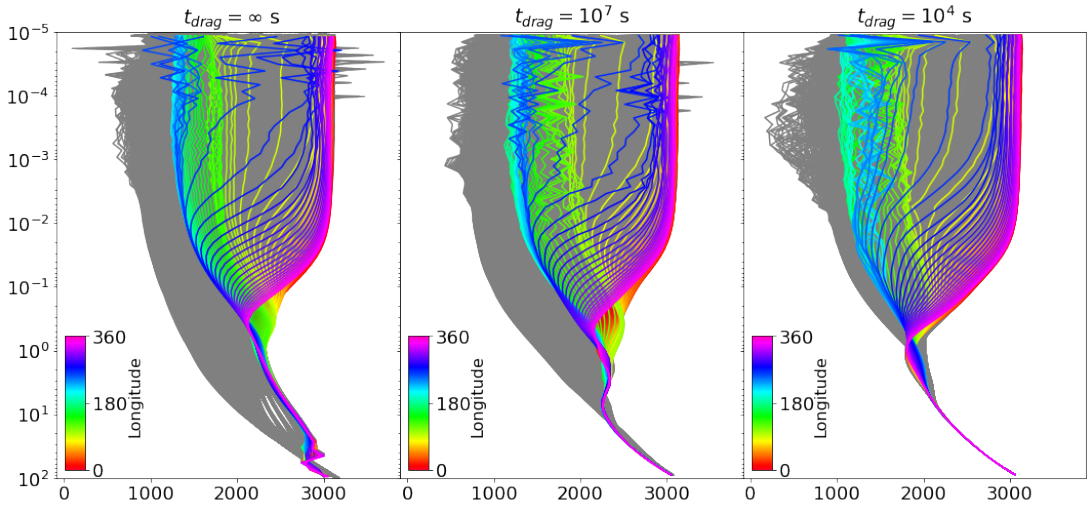

Figure 3.6 Temperature-Pressure profiles for different uniform drag timescales. The shortest uniform drag timescale case (10^4 s) exhibits a stronger thermal inversion ending deeper in the atmosphere and a more uniform lower atmosphere compared to the drag-free case. Additionally, the shortest uniform drag timescale causes cooler nightside temperatures, as it diminishes all of the temperature-homogenizing flow instead of just the east-west component, as in our active magnetic drag models. The 10^7 s uniform drag timescale case shows these same effects, but to a lesser degree.

and extends deeper in the atmosphere. The longer uniform timescale (10^7 s) exhibits these effects to a smaller degree. This effect was not seen with our active magnetic drag models, where the timescales increase with increasing pressure.

In Figure 3.7, we show a similar plot to Figure 3.3, but for the case of uniform drag timescale. The differences between the drag-free model and the uniform drag models are more subtle than for our active magnetic drag models with different assumed field strengths. Because the uniform drag is applied evenly throughout the atmosphere, the resulting wind structure is similar in shape but weaker in strength than the drag-free case for the longer timescale. For the shorter timescale, the flow pattern west of the substellar point actually shows some westward motion at nearly all latitudes at and above 0.1 bar. This behavior is seen in other GCMs with uniform drag and is a result of the frictional drag becoming the dominant term in the momentum equation (*Komacek and Showman*, 2016; *May et al.*, 2021).

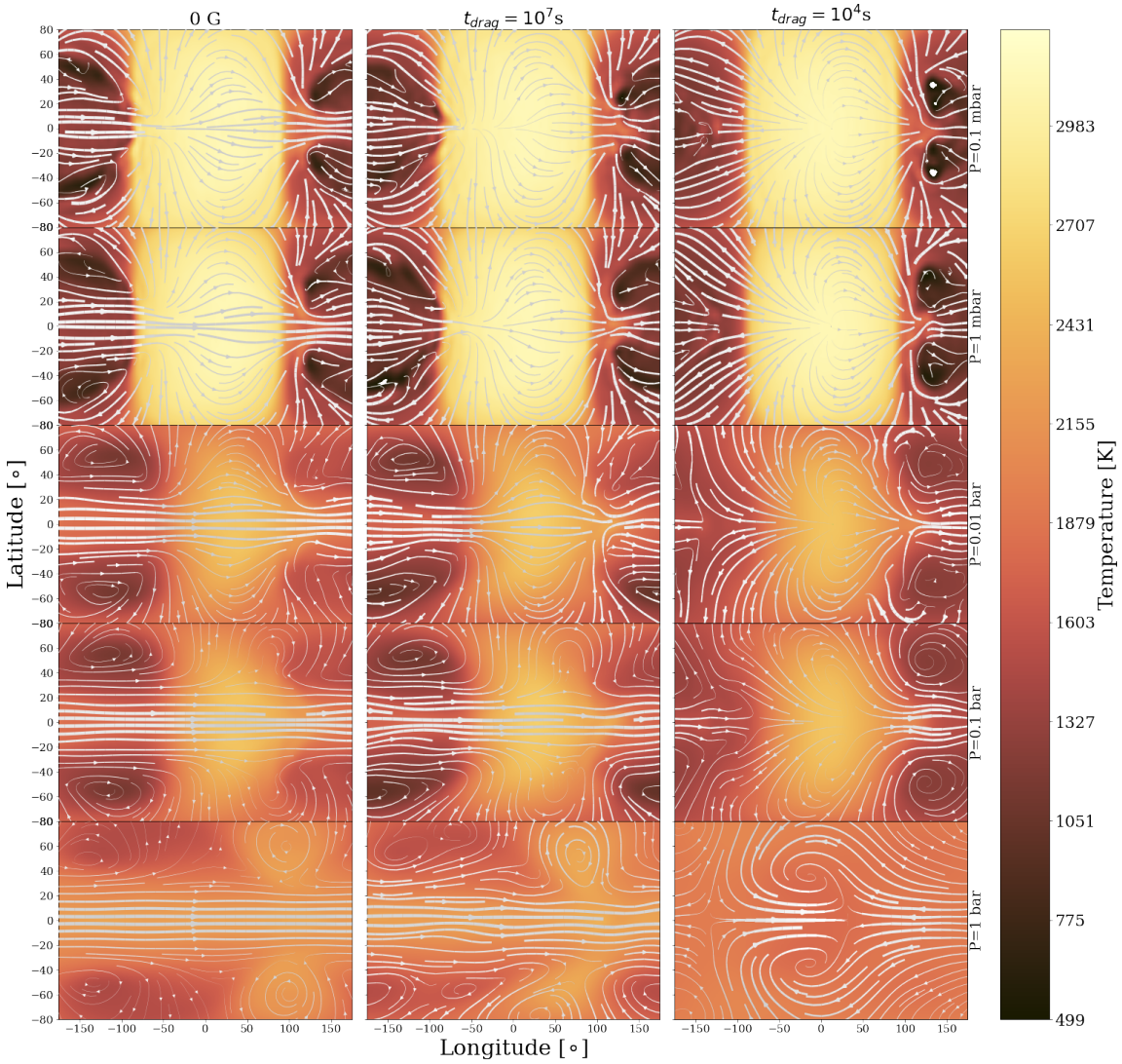

Figure 3.7 Maps of temperature and wind structure at the same pressure levels as Figure 3.3, but comparing the uniform drag timescale cases. The differences in atmospheric circulation caused by the uniform drag timescale are more subtle but most prominently seen in the weakening of the equatorial jet in the lower atmosphere.

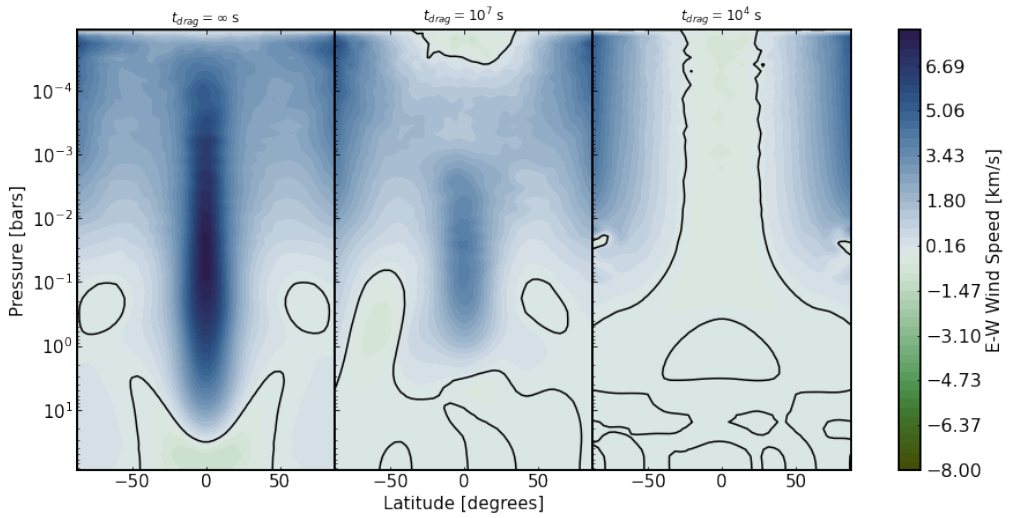

Figure 3.8 Longitudinally averaged east-west wind speeds for the uniform drag timescale cases. The 10^7 s uniform drag timescale weakens the equatorial jet, while the shorter, 10^4 s timescale completely eliminates it. In this shorter timescale we see instead weaker, higher latitude jets, which also begin to appear in the 10^7 s drag timescale case.

Figure 3.8 shows the longitudinally averaged east-west winds (akin to Figure 3.4) for the uniform drag timescale cases. We can see that the uniform drag timescale prescription destroyed the equatorial jet for the shortest, 10^4 s timescale. Interestingly, some weaker, higher latitude eastward jets are present for most of atmosphere($P \lesssim 1$ bar). For the longer uniform drag timescale, we see that the jet has been weakened to a point where there is actually a slight net westward flow at very low pressures ($P \lesssim 0.1$ mbar). However, from examining Figure 3.7, we see that the wind structure contains both significant east and westward flow, largely canceling each other out in the zonal average.

We can make a more direct comparison of our uniform drag timescale models to the "cold interior" models of WASP-76b in *May et al.* (2021). For the weak drag timescale (10^7 s), the flow patterns and temperature structures between our two works (our Figure 3.7 and their Figure 5) are very similar. One difference to

note is that our upper atmospheres tend to be hotter and our lower atmospheres are colder than those in *May et al.* (2021), likely due to their inclusion of hydrogen dissociation and recombination. We also note that the longitudinally averaged east-west wind speeds (our Figure 3.8 and their Figure 7) are broadly similar in overall wind pattern in the case of weak drag. Both models exhibit a strong equatorial jet of similar strength that extends to $\sim$ 1 bar. The model in *May et al.* (2021) exhibits westward flow at high latitudes on order of a few km/s that are not present in our model. Comparing the strong drag cases shows larger differences between our models. Although both models display the disruption of the equatorial jet at all pressure levels modeled, our model shows the emergence of net eastward flow at high latitudes extending to the top of the modeled atmosphere. The corresponding models in *May et al.* (2021) show westward flow for high latitudes at the top of the atmosphere ($P < 10^{-2}$bars) and eastward flow of a smaller magnitude at pressures lower than this.The general qualitative agreement between these uniform drag models (which differ in other parameter choices) suggests that the differences we find between our active and uniform drag models may be contextualized within the broader work of the community, where uniform drag timescales have been more commonly used.

3.5.4 Observable Consequences: Phase Curves

Figure 3.9 shows our calculated phase curves from all of the models. As we increase the magnetic field strength in our active magnetic drag models, the peak of the phase curve shifts nearer to 0.5 (secondary eclipse) and the amplitude is increased. This is the expected result of our magnetic drag disrupting the eastward advection of hot gas away from the substellar point and generally reducing the transport of heat to the nightside. The difference in the phase of peak flux between our 3 G and 30 G models is small, as in both cases the hot spot is essentially unmoved from the substellar point. The larger amplitude of the 30 G case can be attributed to a cooler nightside and

a stronger suppression of eastward flow in the upper atmosphere. A similar pattern exists for the uniform drag timescale models. The longer uniform drag timescale peaks at a similar phase to our model with no magnetic (or other) drag applied, meaning that its hot spot is still efficiently advected east of the substellar point despite the drag applied. The phase curve for the shorter uniform drag timescale model peaks between the curves for our 0.3 and 3 G models, reflective of the increased ability of the drag to prevent advection of the hot spot. Because phase curves integrate flux over the entire visible hemisphere, many of the differences between our active magnetic cases and uniform are lost in this integration. Published *Spitzer* 4.5 micron phase curves of this planet show a very small hotspot offset (< 0.003 in orbital phase from 0.5, *May et al.* (2021)), making our 3 G and 30 G models most consistent with the data. Given the double-grey nature of our GCM, comparing our bolometric phase curve amplitudes and the *Spitzer* amplitudes in parts per million of the stellar flux is not trivial and imprecise, as it relies on the use of multiple assumptions. Thus, we refrain from those comparisons here. We do note however that our equatorial day-night contrasts are in broad agreement with the 1440K brightness temperature contrast reported in *May et al.* (2021).

3.6 Discussion

Compared to the less complex treatment of magnetism as a uniform drag, our active magnetic drag has some advantages. First, we are able to see clearly the difference in the magnitude of magnetic effects on the dayside vs the nightside. The uniform drag scenario forces all sides of the planet to be treated equally, despite the large difference in temperature around the planet. Many of the small scale atmospheric effects of our active magnetic drag disappear when the drag becomes uniformly applied. Similarly to *Kreidberg et al.* (2018), we can roughly estimate the magnetic field strength that corresponds to uniform drag timescales used in this work. Because

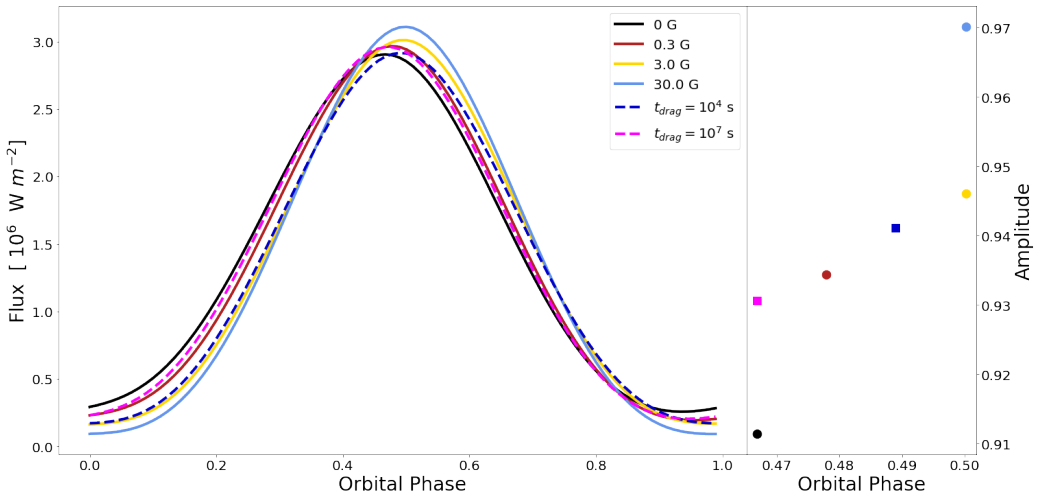

Figure 3.9 Left: orbital phase curves of total (bolometric) thermal emission for all of the models from this paper. Right: the amplitude $((F_{\max} - F_{\min})/F_{\max})$ and phase of peak flux for each model's phase curve. For our active magnetic drag cases, increasing the magnetic field strength increases the amplitude of the phase curve and causes it to peak closer to a phase of 0.5 (which is secondary eclipse, not shown). This reflects the diminished day-night heat transport and disrupted eastward flow, due to the influence of the drag. The uniform drag timescale cases show similar behavior. The longer uniform drag timescale case has a similar hot spot shift to our non-dragged, 0 G case but an amplitude more similar to our 0.3 G model, while the shorter drag timescale has a phase curve amplitude and peak between the 0.3 and 3 G active drag models.

the same timescale is applied to the atmosphere regardless of temperature, the corresponding field strength on the dayside and the nightside will differ dramatically. Based on equation 12 from *Perna et al.* (2010a), we estimate that our shorter drag timescale (10^4 s) would correspond to a field strength of ∼6 G on the dayside equator and nearly 300 G on the nightside equator.[2] For the longer uniform drag timescale (10^7 s) we estimate the corresponding field strengths to be ∼0.2 G and ∼10 G on the dayside and nightside respectively. Physically, we do not expect the nightside field strength to be nearly two orders of magnitude stronger than the dayside. Allowing our magnetic resistivity to vary spatially and temporally is also an improvement to treatments found in current non-ideal MHD models which employ temporally fixed resistivity. Because our active magnetic drag treatment allows the drag strength to vary as a function of temperature and pressure, we are able to model magnetic resistivity in a more physically consistent fashion.

Second, it is important that our active magnetic drag is only applied to the east-west momentum equation as we are assuming a planetary dipole field. As a result, there is a fundamental change in the direction of atmospheric circulation. Our dayside flow patterns were very distinct from the 0 G model in the upper atmosphere, as shown in Figure 3.3. Uniform drag timescales, on the other hand, are applied to east-west *and* north-south momentum equations. When the uniform drag timescale is long enough that equatorial super-rotation is still present, the corresponding flow patterns are similar in shape to the drag-free models but lower in strength. The shorter uniform drag model was able to disrupt this superrotation in a way that can produce slight net westward flow near the equator. Our active magnetic drag prescription is able to produce distinct differences in flow patterns that a uniform drag timescale is not.

Many hot and ultra-hot Jupiters have inflated radii, which is likely due to energy deposited in the internal adiabat of the planet (*Batygin et al.*, 2011; *Laughlin et al.*,

[2]For this calculation we used a pressure of 0.11 bar and temperatures of 2500K on the dayside and 1500K on the nightside.

2011; *Lopez and Fortney*, 2016; *Komacek and Youdin*, 2017; *Thorngren et al.*, 2021). Energy dissipation due to currents flowing in a resistive atmosphere has been theorized as a potential mechanism to deposit this energy (*Batygin and Stevenson*, 2010; *Perna et al.*, 2010b; *Rogers and Showman*, 2014; *Thorngren and Fortney*, 2018). In our models, we return the kinetic energy lost from our magnetic drag timescales in the energy equation as u^2/t_{mag}, mimicking local Ohmic dissipation. Notably, the deepest pressure modeled in this work is only 100 bars, so we cannot self-consistently predict the amount of heating that would be deposited deeper. However, using results from 1D global models of Ohmic dissipation profiles (*Huang and Cumming*, 2012; *Wu and Lithwick*, 2013) as guidance, we might expect the Ohmic dissipation in the convective interior to be around 1% that of the Ohmic dissipation at the base of our dynamically active atmosphere. For each of global fields tested (0.3 G, 3.0 G, and 30 G) this approximates to 10^{18} W, 10^{20} W, amd 10^{19} W respectively deposited in the interior, which correspond to a maximum value of $\sim 0.01\%$ of the stellar irradiation for the 3G model. The internal heating needed to inflate a planet will be dependent on model assumptions and evolutionary history, but using the general estimate from *Komacek and Youdin* (2017), which suggests that internal heating rates $\lesssim 1\%$ of stellar irradiation at a minimum depth of 100 bars can explain inflated hot Jupiter radii, we cannot conclude that our model's Ohmic heating could explain the inflated radius of WASP-76b. Future studies, particularly those that model deeper pressures than the ones presented here, will be needed to explore this issue more thoroughly and self-consistently.

In order to first focus on the effects of our active magnetic drag treatment, we have chosen to omit molecular hydrogen dissociation/recombination, thermal ionization, and clouds. All of these processes should be present on WASP-76b, so further work is necessary to better understand the interactions of these processes with our active magnetic drag. Although we did not include these effects in our models, we can

estimate how they would alter our model based on results from other GCMs. One of the main effects expected from molecular hydrogen dissociation and recombination is a reduction of the day/night temperature contrast (*Bell and Cowan*, 2018; *Tan and Komacek*, 2019). Cooling the dayside and warming the nightside would likely work to reduce some of the effects of magnetism on the upper atmosphere daysides of our models. By increasing the length of our magnetic timescale on the dayside of the planet, we would expect the day flow pattern of only north-south winds to not persist as deep in the atmosphere. The pressure at which east-west flows emerge again on the dayside will likely still be determined to first order by the strength of the global magnetic field.

Based on the condensation curves from *Roman et al.* (2021), clouds would likely be confined entirely to the nightside, particularly at upper latitudes of the planet due to the high temperature of the dayside These clouds could work to blanket part of the nightside, trapping heat and warming the area by a couple hundred Kelvin below the cloud. This would decrease the magnetic drag timescales on these nightside pressure regions, but seeing that these timescales are already many orders of magnitude longer than the dayside timescales, the effects of our magnetic drag would still be predominately on the dayside of the planet. Furthermore, above the clouds, we can expect a similar amount of cooling, which would decrease the likelihood of the overall nightside flow patterns being significantly altered from the cloud-free models we present here.

Though we did not include clouds in these models, we can use the temperature profiles from Figure 3.2 and the condensations curves from *Roman et al.* (2021) to speculate what potential cloud species could exist on the nightside of the planet. Based on the temperature structure, KCl, ZnS, and MnS clouds are only possible at high latitudes in the upper atmosphere, at pressures lower than above $\sim 10^{-2}$ bars or so. The condensation curves of Cr_2O_3, SiO_2, VO, and Mg_2SiO_4 show that these species could exist as condensates on the nightside equator at pressures near above

$\sim 10^{-1}$ bars and at high latitudes for lower pressures. Ni, Fe, Ca_2SiO_4, $CaTiO_3$, and Al_2O_3 are also potentially present at nearly all pressures modeled, but would be confined to the nightside of the planet.

Our active magnetic drag treatment makes simplifying assumptions regarding the shape of the planet's magnetic field (a dipole), its orientation (aligned with the rotation axis), and that it lacks any time variability. To more accurately represent the magnetic field of this planet, one potential route forward would be to incorporate non-ideal MHD equations, which are extremely computationally expensive in a 3D atmosphere. Work done at this level of complexity highlights the expected variability and asymmetry of the induced magnetic field lines and strength (*Rogers and Komacek*, 2014; *Rogers and McElwaine*, 2017), and westward advection of the hot spot (*Rogers*, 2017; *Hindle et al.*, 2021b)However, it is important to note that non-ideal MHD has never been coupled to a dynamical solver without explicit viscosity. Models with explicit viscosity return wind speeds significantly reduced compared to those found in primitive equation GCMs like the one presented here, even in the purely hydrodynamic case (*Rogers and Showman*, 2014; *Rogers and Komacek*, 2014). Additonally, current non-ideal MHD models do not currently incorporate the large day-night magnetic resistivity variations presented in our model. A useful path forward could involve improvements to our kinematic MHD model by relaxing our strict dipole assumption and accounting for the toroidal component of the field. This would increase the validity of our model in the regions where the magnetic Reynolds number exceeds 1.

3.7 Conclusion

In this work we presented GCMs of the ultra hot Jupiter WASP-76b, focusing on the role of magnetic drag in shaping this planet's atmospheric structure. We used the "active magnetic drag" treatment from *Rauscher and Menou* (2013), which calculates

a drag timescales based on local conditions throughout the atmosphere and updates these values as the simulation runs. Our main results are as follows:

- The influence of our active magnetic drag was most strongly seen in the upper atmosphere dayside of the planet, where the drag timescales were the shortest. The winds here were solely in the north-south direction, such that hot gas from the dayside mainly flowed to the nightside over the poles, as our magnetic drag reduces momentum in the east-west direction.

- The stronger the global magnetic field strength, the deeper in the atmosphere the effects of our magnetic drag were seen. Our drag treatment can dramatically disrupt the equatorial jet seen in hot Jupiter models, reducing its strength and causing it to be confined to the lower atmosphere, where the magnetic timescales become longer. At the strongest case we examined, 30 G, the equatorial jet was reduced significantly and the atmosphere no longer displayed superrotation.

- We calculated bolometric thermal emission phase curves from our GCMs and found that the models with active magnetic drag had larger amplitudes (due to less efficient day-night heat transport) and peaked nearer to secondary eclipse. In comparison to Spitzer phase curve observations of this planet (*May et al.*, 2021), our models would imply a magnetic field strength of at least 3 G for WASP-76b. We do note, however, that other important physical processes are missing from these models (hydrogen dissociation and clouds) and a full comparison with the data requires modeling all of these processes together.

- We also looked at the effects of using a uniform drag timescale as an estimate for magnetic drag. Unlike our active drag timescale, the uniform treatment applied the same drag timescale globally in the east-west and north-south momentum equations. The circulation patterns in the upper atmosphere of the uniform case differed significantly from our active magnetic drag treatment, especially on the

dayside.The corresponding phase curves put the longer timescale (10^7 s) model between our drag-free and 0.3 G active model and the short timescale (10^4 s) between our 0.3 G and 3.0 G active models. Order of magnitude estimates based on local conditions of the dayside and nightside of the planet indicate field strengths from ∼6-300 G and ∼0.2-10 G for the short and long timescale respectively. We have shown that our active magnetic drag case does a better job of reproducing the expected physics of UHJs.

Our active magnetic drag prescription is an improvement over the use of uniform drag timescales to model the interaction between partially thermally ionized winds and a deep-seated planetary magnetic field, in that it captures more of the physical behavior we expect. However, we re-emphasize that the physically correct solution will require complex and computationally expensive full non-ideal MHD treatments in regions where the magnetic Reynolds number is greater than 1. In this regime, the induced atmospheric field becomes comparable or larger than the dipolar field. As a result of this feedback in atmospheric circulation, hot spot reversal and time-variability can occur (*Rogers and Komacek*, 2014; *Hindle et al.*, 2019, 2021b) Future changes to our model should improve on our kinematic MHD framework and incorporate the effects of the toroidal field on meridional winds to replicate these steady state features in the high Reynolds number regime. . Given the high observational interest for UHJs, our community should invest in further development and use of those models especially for UHJs with strong thermal ionization such as WASP-76b, HAT-P-7b, WASP-18b, and KELT-9b.

With future work, we will more carefully examine the influence of active magnetic drag on various types of atmospheric characterization measurements, beyond just the bolometric phase curves shown here. In particular, high-resoultion spectroscopy may be a promising avenue for empirically constraining wind speed and drag mechanisms (*Miller-Ricci Kempton and Rauscher*, 2012; *Flowers et al.*, 2019; *Beltz et al.*, 2021)

3.8 Acknowledgements

We would like to thank the reviewer for their detailed and incredibly helpful comments which greatly improved the quality of this paper. This work was generously supported by the Heising-Simons Foundation.

CHAPTER IV

Magnetic Drag and 3D Effects in Theoretical High-resolution Emission Spectra of Ultrahot Jupiters: the Case of WASP-76b (Beltz et al 2022b)

"Poets are always taking the weather so personally. They're always sticking their emotions in things that have no emotions"

– J D Salinger

4.1 Preface

Results in this chapter were published in: *Beltz, H., Rasucher, E., Kempton, E., Malsky, I., Ochs, G., Arora, M., and Savel, A., 2022b. Magnetic Drag and 3D Effects in Theoretical High-resolution Emission Spectra of Ultrahot Jupiters: the Case of WASP-76bb. The Astronomical Journal, 164, 140* and are reproduced here with minor style revisions by permission of the American Astronomical Society under the non-exclusive right of republication granted to authors.

4.2 Abstract

Ultrahot Jupiters are ideal candidates to explore with high-resolution emission spectra. Detailed theoretical studies are necessary to investigate the range of spectra we can expect to see from these objects throughout their orbit, because of the extreme temperature and chemical longitudinal gradients that exist across day and nightside regions. Using previously published 3D GCM models of WASP-76b with different treatments of magnetic drag, we post-process the 3D atmospheres to generate high-resolution emission spectra for two wavelength ranges and throughout the planet's orbit. We find that the high-resolution emission spectra vary strongly as a function of phase, at times showing emission features, absorption features, or both, which are a direct result of the 3D structure of the planet. At phases exhibiting both emission and absorption features, the Doppler shift differs in direction between the two spectral features, making them differentiable instead of canceling each other out. Through the use of cross-correlation, we find different patterns in net Doppler shift for models with different treatments of drag: the nightside spectra show opposite signs in their Doppler shift, while the dayside phases have a reversal in the trend of net shift with phase. Finally, we caution researchers from using a single spectral template throughout the planet's orbit; this can bias the corresponding net Doppler shift returned, as it can pick up on a bright region on the edge of the planet disk that is highly red- or blue-shifted.

4.3 Introduction

High-Resolution Spectroscopy (HRS) ($R \gtrsim 15,000$) has opened up exciting new pathways into exoplanet atmospheres. By taking advantage of the tens of thousands of spectral lines separable at this higher resolution, astronomers are able to detect scores of atmospheric species, despite the orders of magnitude flux contrasts between

the planet and the star. In order to unlock this information, the HRS method uses a template spectrum for the planet and cross-correlates this across wavelengths (which is equivalent to varying the Doppler velocity shift of the spectrum) with the data to search for a peak signal. The planet's orbital motion will cause its signal to shift with wavelength during an observation. Since the orbital motion of the planet is known, this method can reject spurious low-significance signals and reliably pinpoint the planet's atmospheric signature. The atmospheric conditions used to calculate the template spectrum can be adjusted until they most closely match reality, producing the largest detected signal. HRS can also be used to detect atmospheric motion on the planet in the form of net redshifts or blueshifts (such as the first-ever HRS detection from *Snellen et al.*, 2010) as well as constrain rotational velocities from Doppler broadening (*Snellen et al.*, 2014; *Brogi et al.*, 2016; *Schwarz et al.*, 2016; *Flowers et al.*, 2019) and even obliquity (*Bryan et al.*, 2020). Recently, the most precise C/O ratio in a hot Jupiter was measured with HRS techniques (*Line et al.*, 2021) using the framework described in *Brogi and Line* (2019). An excellent review of HRS techniques can be found in *Birkby* (2018); *Brogi and Birkby* (2021).

Crucial to the successful use of this method is having a template spectrum to use in the cross-correlation that accurately matches the planet's true spectrum. For this work, we will focus on the two classes of model spectra: those generated from 1D atmospheric models and those generated from more physically consistent 3D models, each of which have their advantages and disadvantages. On one hand, 1D models are feasible to compute over large parameter spaces in a reasonable amount of computing time. They have also been used with high-resolution emission spectra to detect a variety of species including (but certainly not limited to) Fe, Ti, Mg, TiO, CO, OH, H_2O,CH_4 (see *Brogi et al.*, 2014; *Gandhi and Madhusudhan*, 2018; *Guilluy et al.*, 2019; *Nugroho et al.*, 2020; *Giacobbe et al.*, 2021; *Kasper et al.*, 2021; *Nugroho et al.*, 2021; *Pelletier et al.*, 2021, for some recent examples). However, planets are 3D

objects, and using a 1D template can lead to unintended consequences. At low and medium resolution, using a 1D model can bias interpretations such as incorrectly constraining abundances and temperature structures (*Feng et al.*, 2016; *Blecic et al.*, 2017; *Caldas et al.*, 2019a; *Pluriel et al.*, 2020; *Taylor et al.*, 2020). These biases should become more pronounced when planetary properties vary strongly as a function of longitude. In HRS observations, spectral liens are more fully resolved, allowing the 3D atmospheric structure to directly impact the shapes of the observed lines, calling into question the applicability of the 1D assumption.

3D models, on the other hand, are much more computationally expensive to calculate (generally requiring at least a few weeks to run to completion). 3D models are also by nature more complicated to calculate simulated spectra from as the geometry and radiative transfer calculations are more complex than the 1D case (*Zhang et al.*, 2017). (However, recent open-source tools such as the ones presented in *Lee et al.* (2021) are making this barrier less steep.) Importantly, if the 3D model better matches reality, its spectrum will produce a stronger cross-correlation signal with the high-resolution data. In *Beltz et al.* (2022b), we found that our 3D hot Jupiter model outpreformed hundreds of 1D models when used in the analysis of high-resolution emission spectra. 3D models are also able to capitalize on the 3D effects present in HRS such as Doppler shifting of lines, temperature gradients, and chemical inhomogenieties (*Flowers et al.*, 2019; *MacDonald and Lewis*, 2021; *Prinoth et al.*, 2021). Other recent work has also been investigating other routes to retrieve 3D structure from high-resolution emission spectra (*Herman et al.*, 2022; *van Sluijs et al.*, 2022).

3D models are especially necessary for ultrahot Jupiters (UHJs), given the large spatial variations across these planets due to their extreme irradiation regime. These planets, with equilibrium temperatures that exceed ~ 2200 K, orbit so close to their host star that they are expected to have tidally-synchronized rotation states (*Showman and Guillot*, 2002). This means that these planets have a constant dayside that

is continually bombarded by stellar irradiation and a permanent nightside. An emerging ubiquitous property of UHJ atmospheres is that they exhibit dayside temperature inversions—that is, regions of decreasing temperature with increasing pressure—in contrast to their cooler hot Jupiter cousins (*Baxter et al.*, 2020; *Mansfield et al.*, 2021). The exact cause of these inversions is still debated, but high-altitude optical and UV absorbers such as TiO or VO (*Hubeny et al.*, 2003; *Fortney et al.*, 2008) or Fe, SiO, and metal hydrides (*Lothringer et al.*, 2018; *Gibson et al.*, 2020; *Lothringer et al.*, 2022) are likely candidates. Alternative potential causes for the inversions include high C/O ratios (*Mollière et al.*, 2015) or inefficient IR cooling (*Gandhi and Madhusudhan*, 2019). These temperature inversions manifest themselves in the emitted spectra of the planet, where dayside spectra show emission features. The nightsides of these planets, due to their mostly monotonic temperature structure, will only show absorption features.

Due to the extreme irradiation received, the daysides of UHJs are hot enough for the thermal dissociation of important molecules. This can significantly change the main opacity sources (e.g., removing water and adding H^-, such that spectral features become more muted; *Parmentier et al.*, 2018) or in the most extreme cases change the dominant atmospheric gas from molecular to atomic hydrogen (*Bell and Cowan*, 2018). The dissociation of molecular hydrogen on the dayside and its recombination on the nightside should decrease the temperature gradient across the planet and decrease the expected wind speeds (*Tan and Komacek*, 2019).

For this work, we focus our investigation on magnetism and its role in UHJ atmospheres. Magnetic field generation strength still holds uncertainties, but work from *Christensen et al.* (2009) predicts that given a sufficient rotation rate (like that of tidally locked UHJs) magnetic field strength of planets may scale with energy flux. For the most inflated HJs, *Yadav and Thorngren* (2017) estimates maximum surface field strengths to be between 50-100 G, with more massive planets having the po-

tential for even stronger fields. While there have been no direct measurements of exoplanet magnetic field strength yet, several indirect methods can offer constraints for particular planets. Recently, *Ben-Jaffel et al.* (2021) detected the magnetosphere of the warm Neptune HAT-P-11b and estimate the equatorial magnetic field strength to be between 1–5 G. Magnetic planet star interactions, specifically Calcium II K emission, have also been used to indirectly estimate surface magnetic field of hot Jupiters in the range of 10-100 G (*Cauley et al.*, 2019). Variability in hot spot location has been found in 3D non-ideal MHD models, leading *Rogers* (2017) to estimate a minimum magnetic field strength of 6 Gauss for the UHJ HAP-P-7b, in order to explain observed variability on that planet (it should be noted however that recent work from *Lally and Vanderburg*, 2022, find that that the observed variation could be due to non-atmospheric sources). In our previous work, *Beltz et al.* (2022b), we were able to estimate a minimum field strength of 3G for WASP-76b based on comparisons with phase curves published by *May et al.* (2021).

In our modeling, we remain agnostic to the intricacies of the planet's internal dynamo and instead assume a deep-seated global magnetic field of some magnitude exists, in order to focus on the effects of magnetic drag in the atmosphere of the representative UHJ WASP-76b and how that drag influences its emission spectra. Notably, our magnetic drag treatment does not solve the full non-ideal MHD equations that, due to their added computational complexity, require other simplifying assumptions (see the discussion of this in *Beltz et al.*, 2022b). Instead, we use a parameterized approximation of magnetic drag first introduced in *Perna et al.* (2010a). A physical explanation of this parameterization can be thought of as follows: due to the partial thermal ionization of species on the dayside of UHJs, the strong winds on the planet will blow these charged particles (embedded in a mostly neutral flow) around the planet, crossing magnetic field lines and generating current. These currents, should they travel into the planet's interior and deposit heat in a process known as Ohmic

dissipation, could play a role in inflated radii of many hot Jupiters (*Batygin and Stevenson*, 2010; *Perna et al.*, 2010b; *Thorngren and Fortney*, 2018). In the atmosphere, the bulk Lorentz force that ionized particles experience can reduce circulation efficiencies and therefore increase the day-night contrast (*Perna et al.*, 2010a; *Menou*, 2012; *Batygin et al.*, 2013; *Rogers and Showman*, 2014). Previous work showed this in models of the hot Jupiters HD209458 b and HD189733 b (*Rauscher and Menou*, 2013) and for the case of the ultrahot Jupiter WASP-76b (*Beltz et al.*, 2022b). Now, in this work, we take the models from *Beltz et al.* (2022b) and post-process their results to study the resulting high resolution emission spectra.

Our models are all based on parameters from the UHJ WASP-76b, an inflated planet orbiting its host star every 1.81 days. This planet has been the target of many high-resolution transit analyses, and a multitude of different species have been detected in its atmosphere, including Fe I, Na, Li I, Ca II (*Seidel et al.*, 2019; *Deibert et al.*, 2021; *Casasayas-Barris et al.*, 2021; *Kawauchi et al.*, 2021; *Tabernero et al.*, 2021),and recently molecules like OH (*Landman et al.*, 2021).Analyses of high resolution emission spectra have yet to be published. The work by *Kesseli and Snellen* (2021a) explores an entire atomic spectral survey of the atoms and ions that have been detected on this UHJ and finds evidence for temperature and chemical gradients on the planet. This planet has also garnered interest from astronomers due to an asymmetric detection of iron in its transmission spectrum throughout transit, first found by *Ehrenreich et al.* (2020) and later confirmed by *Kesseli and Snellen* (2021b). *Ehrenreich et al.* (2020) proposed this asymmetric absorption signal is a result of iron condensing on the nightside of the planet. Other proposed mechanisms for this absorption signal include temperature asymmetry between the trailing and leading limbs (*Wardenier et al.*, 2021) or clouds (*Savel et al.*, 2022a). 3D atmospheric models of this planet have also been published in *May et al.* (2021); *Savel et al.* (2022a); *Wardenier et al.* (2021); *Beltz et al.* (2022b).

In this work, we generate high-resolution emission spectra from previously published models of the UHJ WASP-76b to explore how different magnetic drag treatments affect the resulting spectra and how these differences change as a function of phase. This particular planet is of high observational interest but also provides a route to make predictions regarding emission spectra from UHJs more generally. The structure of this paper is as follows: In section 5.4, we briefly describe the models used in this work, the variety of drag treatments in our models, and the process of post-processing our model output to create simulated high-resolution emission spectra. In section 5.5, we explore the features that show up in our 3D emission spectra and how they differ between our models. In section 5.6 we discuss important caveats to our models and assumptions. Finally, we summarize our main findings in section 5.7.

4.4 Methods

4.4.1 General Circulation Model

In this work, we use a subset of the models produced and described in *Beltz et al.* (2022b), and will briefly summarize the details here. General Circulation Models (GCMs) solve the primitive equations of meteorology in three dimensions to simulate the physics and circulation patterns of planetary atmospheres. We use the GCM from *Rauscher and Menou* (2012) which underwent a radiative transfer upgrade in *Roman and Rauscher* (2017) (based on *Toon et al.*, 1989). The absorption coefficients for the WASP-76b models were informed by the 1D temperature-pressure profiles modeled in *Fu et al.* (2021), chosen such that the double-gray analytic profile *Guillot* (2010) roughly matched those results. Every model was run with 65 vertical layers spread out evenly in log space over 7 orders of magnitude in pressure from 100 to 10^{-5} bar and with a horizontal spectral resolution of T31, corresponding to ~ 4 degrees at the

Table 4.1. WASP-76b Model Parameters

Parameter	Value
Planet radius, R_p	1.31×10^8 m
Gravitational acceleration, g	6.825 m s^{-2}
Orbital Period	1.81 days
Rotation rate [a], $\omega_{\rm orb}$	4.018×10^{-5} s^{-1}
Substellar irradiation, $F_{\rm irr}$	5.14×10^6 W m^{-2}
Planet internal heat flux, $F_{\rm int}$	3500 W m^{-2}
Optical absorption coefficient, κ_{vis}	2.4×10^{-2} cm^2 g^{-1}
Infrared absorption coefficient, κ_{IR}	1×10^{-2} cm ^{2} g^{-1}
Specific gas constant, R	3523 J kg^{-1} K^{-1}
Ratio of gas constant to heat capacity, R/c_p	0.286

[a]Assumed to be in a synchronous rotation state.

equator. Each simulation was calculated for a total of 2000 planetary days. Relevant global parameters are shown in Table 4.4.1.

Other commonalities of the models include the addition of "sponge layers" in the top three layers of the model. These layers apply extra drag near the top boundary of our model to reduce the buildup of artificial numerical noise. These layers have little effect on the atmospheric flow below them and can be found in many GCMs (see *Mayne et al.*, 2014; *Deitrick et al.*, 2020; *Wang and Wordsworth*, 2020, for examples).

4.4.2 Drag treatment in our three models

The three models of WASP-76b from which we have chosen to generate emission spectra have different treatments of drag: Drag-free/0G, Uniform/10^4s, and Active/3G. Here, we will summarize the main distinctions of these treatments. For further information about the detailed differences in circulation patterns that result from these drag treatments, see *Beltz et al.* (2022b). We review the main observable differences in Section 4.5.1.

- Drag-free/0G: This model serves as a base comparison to the other two models as there is no additional sources of drag aside from the sponge layers restricted to the top three layers and the numerical hyperdissipation that prevents the build up of noise on the smallest scales (*Thrastarson and Cho*, 2011). Both of these artificial sources of drag also exist in the other models and are standard features of many GCMs.

- Uniform/10^4s: This model uses a simplified treatment of drag in which the same drag timescale (in this case, 10^4 s) is applied globally at every level to remove momentum from the east-west and north-south components. When serving as a proxy for magnetic effects however, this method has the unfortunate implication of assuming a stronger surface magnetic field (or stronger coupling) on the nightside of the planet than the dayside, contrary to what is expected physically (*Beltz et al.*, 2022b). Uniform drag is used in many GCMs and can also be used to model the effects of other large-scale atmospheric events like hydrodynamic shocks or turbulence (*Li and Goodman*, 2010; *Perez-Becker and Showman*, 2013).

- Active Drag/3G: This treatment of drag is the more physically consistent than the uniform model and falls under the "kinematic" MHD umbrella. Instead of using a single global timescale, we locally calculate our active drag timescale based on the following expression from *Perna et al.* (2010a):

$$\tau_{mag}(B, \rho, T, \phi) = \frac{4\pi\rho\ \eta(\rho, T)}{B^2 |sin(\phi)|} \tag{4.1}$$

  where B is the chosen global magnetic field strength (in this case 3 G), ϕ is the latitude, ρ is the density, and the magnetic resistivity (η) is calculated in the

same way as *Menou* (2012):

$$\eta = 230\sqrt{T}/x_e \text{ cm}^2 \text{ s}^{-1} \tag{4.2}$$

where the ionization fraction, x_e, is calculated from the Saha equation, taking into account the first ionization potential of all elements from hydrogen to nickel (as in *Rauscher and Menou*, 2013). The derivation of this timescale assumes that the planet's interior generates a dipole field, aligned with the planetary rotation axis, that is significantly stronger than any induced magnetic field in the modeled atmosphere (*Perna et al.*, 2010a). As a result, the active drag is only applied in the east-west direction. This active drag timescale was first used in GCMs of the hot Jupiters HD 189733b and HD 209458b (*Rauscher and Menou*, 2013). In the ultrahot Jupiter regime, this timescale was used in *Beltz et al.* (2022b) where we showed that the strong day-night temperature contrast of WASP-76b would result in the timescale varying by many orders of magnitude. For example, at the 10^{-3} bar level, the timescale varies from $\sim 10^{18}$ s on the cold nightside to $\sim 10^{3}$ s on the dayside (see the right panel of Figure 1 in *Beltz et al.* (2022b) for the global distribution of timescales for our 3G model.) This timescale is the most complex treatment of magnetic drag of the models presented here but still does not reach the complexity of implementing the full set of non-ideal MHD equations.

4.4.3 Generating Emission Spectra from the GCM

In order to determine how different magnetic drag parameterizations in our GCM of the UHJ WASP-76b manifest themselves in the high-resolution emission spectra we take our model output and post-process it with a detailed radiative transfer code. First, we regrid the GCM's 65 vertical layers in pressure to 250 layers at constant

altitude, by assuming vertical hydrostatic equilibrium, consistent with the GCM.[1] This is necessary in order to calculate line-of-sight columns and to increase the spatial resolution of the radiative transfer simulations. Based on resolution tests performed by *Malsky et al.* (2021), this number of altitude layers should be sufficient to accurately calculate the emergent spectra.

We perform the radiative transfer calculations for the post-processed spectra following the methods in *Zhang et al.* (2017). We implement the two-stream approximation for inhomogeneous multiple scattering atmospheres from *Toon et al.* (1989). The 3D planet model is divided into 1-D line-of-sight columns (48 latitude and 96 longitude points) and the outgoing intensity from each column is calculated independently. For each column we calculate the total optical depth of each of the 250 layers. The model has the capabilities of simulating different cloud species (e.g. *Harada et al.*, 2021), but no clouds were included in this work. Therefore, the total optical depth at each wavelength is simply

$$\tau_\lambda = \int \kappa_{gas}\, dl \tag{4.3}$$

where κ_{gas} is the local gas opacity at each point along the line-of-sight path. The opacities are evaluated at their Doppler-shifted wavelengths, according to the line-of-sight velocity at each location:

$$\begin{aligned} v_{\mathrm{LOS}} = {} & u \sin\theta + v \cos\theta \sin\phi - w \cos\theta \cos\phi \\ & + \Omega(R_p + z) \sin\theta \cos\phi \end{aligned} \tag{4.4}$$

where ϕ and θ correspond to the latitude and longitude, respectively, Ω is the plane-

[1]Because of the difference in scale heights the dayside vs the nightside, this results in some "empty" grid cells near the top of the nightside of the planet. By setting the temperature, winds, and opacity of these cells to 0, they are essentially ignored in our calculation

tary rotation rate, and u, v, and w are the wind speeds in the east-west, north-south, and vertical directions, respectively.

In calculating our spectra, we assumed Local Chemical Equilibrium (LCE) and solar elemental abundances, which results in the amount of any particular molecular species varying as a function of temperature and pressure. In Figure 4.1, we show the abundance contours for water and CO (the two main sources of opacity at the wavelength ranges presented in this work) as well as equatorial dayside and nightside temperature-pressure profiles. Because of the strong temperature difference between the two hemispheres, we also expect a strong chemical gradient as well for some species. We can see from Figure 4.1 that the water abundances differ more strongly between the day and night side compared to CO. These differences in abundances will have implications for the line strengths in the corresponding emission spectra.

For this work, we calculated spectra at two different wavelength ranges. The first of these spans from 1.14 μm to 1.35 μm, which is inside the wavelength range covered by the upcoming WINERED instrument (*Ikeda et al.*, 2016). This wavelength range has features from H_2O, TiO, VO, K, and Na and most of the spectra and results we show here are from this wavelength range. The other wavelength range we explored was 2.3 to 2.35 μm, which contains opacities from CO, H_2O, and TiO and sits inside the range covered by IGRINS (*Yuk et al.*, 2010; *Park et al.*, 2014b; *Mace et al.*, 2016), CRIRES, and CRIRES+ (*Kaeufl et al.*, 2004; *Follert et al.*, 2014). We explore the differences between these two wavelength ranges in Section 4.5.4. Spectra were calculated from planetary snapshots at phases of every 11.25 degrees for the entire orbit. We use the GCM outputs for the cases of 0 G, 3 G, and the shortest uniform drag timescale (10^4 seconds) from *Beltz et al.* (2022b). We calculate the spectra for two different conditions: one in which the spectral lines are broadened and shifted due to winds and rotation ("Doppler on" spectra) and one without these effects ("Doppler off"). All spectra were calculated at a resolution of R=125,000.

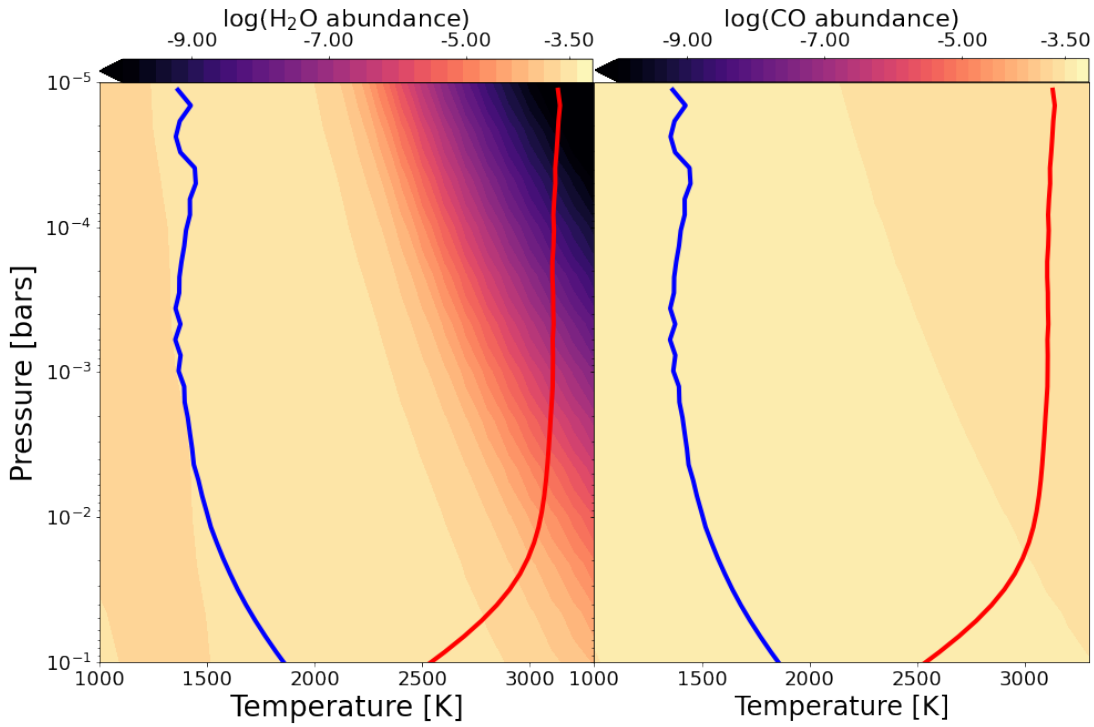

Figure 4.1 Abundance contours of water (*left*) and CO (*right*) as a function of temperature and pressure, used to generate emission spectra, with dayside (red) and nightside (blue) equatorial profiles overplotted. The strong temperature difference between the day and nightside profiles results in a large difference in water abundances. CO, on the other hand, varies less as a function of temperature and thus the CO abundances for the day and night side are similar.

4.5 Results

4.5.1 3-D Atmospheric Structure

Before diving into the spectra, we will briefly summarize the atmospheric structures of our models, as the temperature and wind structure will play a dominant role in shaping the resulting emission spectra. In Figure 4.2 we show the temperature and wind structures on the hemisphere facing an observer, at four phases throughout the planet's orbit and for each of the three models examined in this work. The temperature and wind maps (shown at 10^{-4} bars, around where spectral line cores form) help to visualize the differences in circulation patterns between the three models. The maps of where strong temperature inversions exist (calculated as per *Harada et al.*, 2021) and the line of sight velocities (from winds and rotation) help to visualize which parts of the planet will emit spectra with emission or absorption features, and the net Doppler shift of those features.

Differences in temperature structures and atmospheric flow patterns between these models are discussed in detail in *Beltz et al.* (2022b). The main changes we saw once our active magnetic drag was turned on was an increase in the day-night temperature contrast, a decrease in the hotspot offset, and a change in the flow pattern. Under this active drag treatment, the dayside flow pattern switches from a day-to-night flow over most of the terminator to a flow that is channeled over the poles. Some interesting features not discussed previously are found in the line of sight velocities for our active magnetic drag model. Especially at the phase of 0.25, one can see red-shifted regions near the terminator on the dayside blow up and over the pole, appearing as blue-shifted regions on the nightside. In the uniform drag model we see that significant changes to the circulation over the terminator to the west of the substellar point results in some changes in the line-of-sight velocity patterns, particularly at phases of 0 and 0.75.

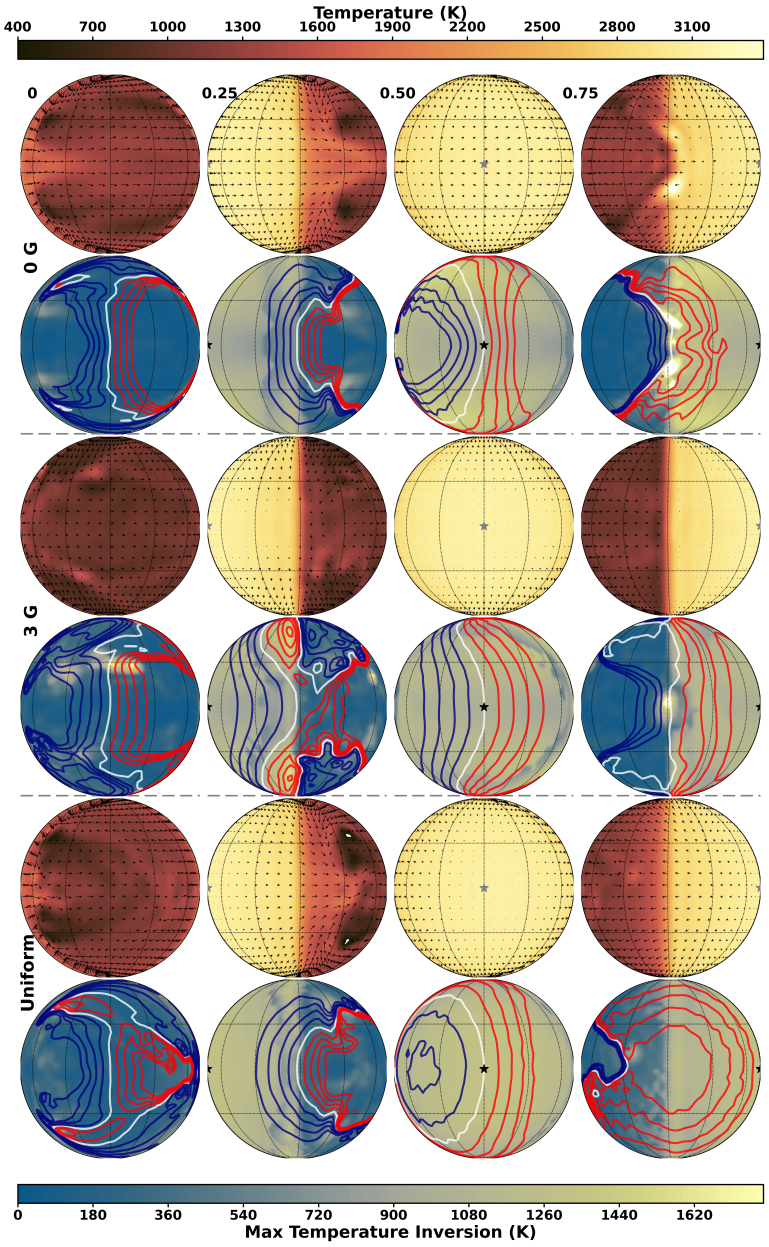

Figure 4.2 Orthographic projections for the 3 models presented in this paper (pairs of rows, top to bottom: 0 G, 3 G, and uniform) at 4 orbital phases (from left to right: 0, 0.25, 0.50, and 0.75; transit would be at 0). The first row of each model shows the temperature structure at 10^{-4} bars (within the region probed by spectral line cores) with wind directions plotted as arrows. The second row for each model shows the maximum vertical temperature inversion at each location. The blue and red contours show constant line of sight velocities in increments of ± 2 km/s at the same pressure level as the temperature plot immediately above it. The differences in temperature structure and wind patterns will influence the high-resolution emission spectra generated from these models.

4.5.2 Spectra as a Function of Orbital Phase

In Figure 4.3, we compare spectra from our 3 different models at three orbital phases: 0 (where the observer only sees the nightside of the planet), 0.25 (first quadrature, where part of dayside and part of the nightside is in view), and 0.50 (where the viewer sees only the dayside of the planet). Due to the higher temperature of the dayside, the spectra corresponding to a phase of 0.50 have a much higher continuum flux than the nightside spectra. The continuum flux level for each model is set by the disk-integrated photospheric brightness temperature at each phase. We can see the largest day–night temperature difference in the 3 G model, followed by the uniform model, and the 0 G model, consistent with the simulated orbital phase curves from these models (*Beltz et al.*, 2022b). Similarly, the 0 G model has a higher continuum flux at an orbital phase of 0.25, compared to the dragged models, since it more efficiently advects hot gas from the dayside toward the eastern terminator, which is the region in view at this phase.

In Figure 4.4, we show spectra from our 3 G model at a variety of phases, both with and without the Doppler effects from winds and rotation. [2] The spectra show an obvious switch between absorption features and emission features as different parts of the planet come into view. While the spectral lines begin in absorption when the nightside of the planet faces us, (at a phase of 0) by a phase of 0.375, enough of the dayside has come into view that the feature switches to emission, as there are temperature inversions found throughout the dayside in our model. Eventually, the features switch back to absorption at a phase of 0.875, as the enough of the nightside comes back into view. Another interesting feature occurs at a phases of 0.25 and 0.75

[2]Throughout this work we show the summed component of winds and rotation. For this planet, the rotational velocity at the equator is ~ 5.2 km s^{-1}, which is slightly below the maximum speed of the equatorial jet from the 0 G model (see Figure 4 in *Beltz et al.*, 2022b). Previous work (*Zhang et al.*, 2017; *Beltz et al.*, 2021) has studied the relative contributions of winds and rotation in high resolution emission spectra and found that the resulting broadening is more nuanced than just a sum of these velocities and is inherently 3D. Since they have comparable contributions to the line-of-sight velocities, it is important to include both.

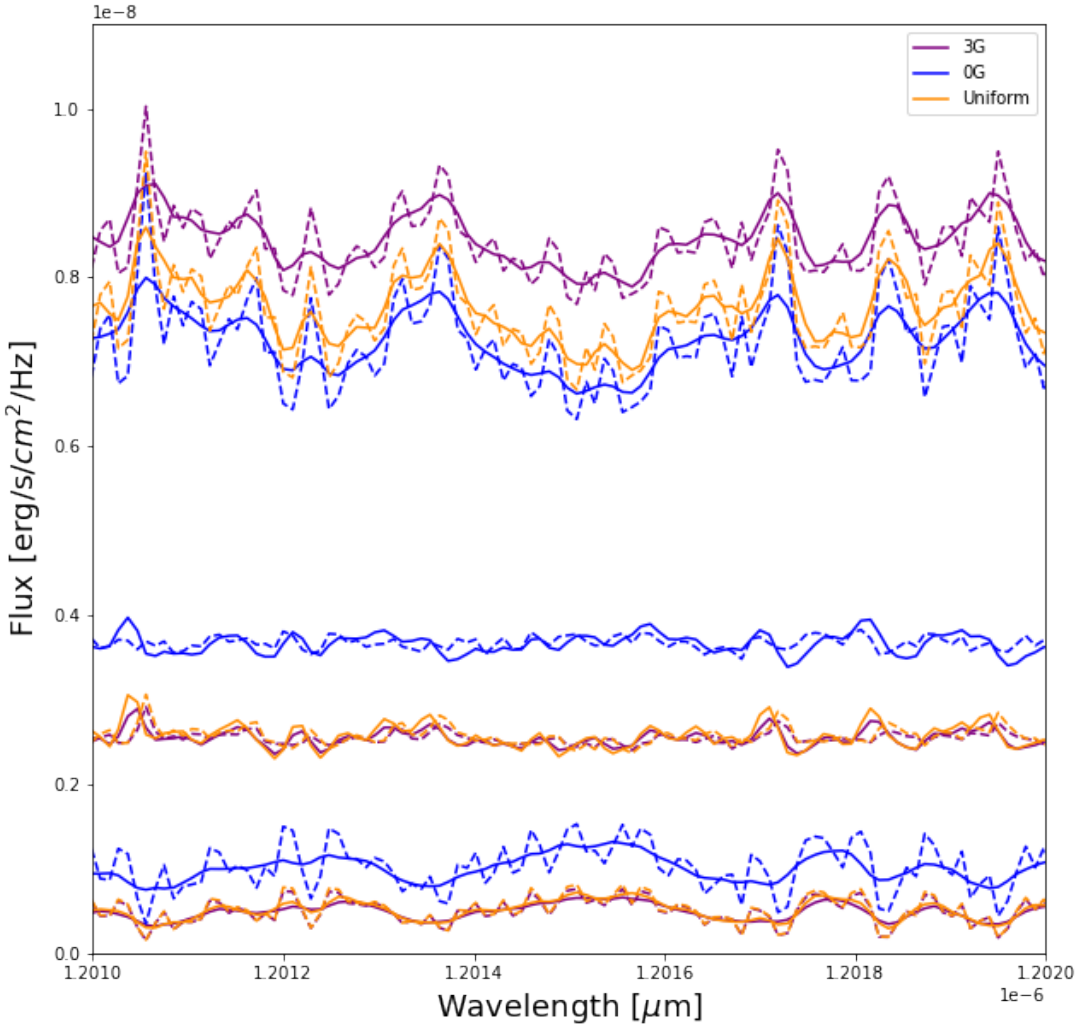

Figure 4.3 Spectra from our 3 models at an orbital phase of 0 degrees (bottom three spectra, when the nightside of the planet is in view), 0.25 (middle 3 spectra, when the day and night are both half in view), and 0.50 (top three spectra, when the dayside is in view). The solid lines show spectra that have been Doppler shifted by winds and rotation while the dashed lines are the spectra without this broadening. By comparing the relative fluxes of these spectra, we can see that the 3G model has the hottest dayside and coldest nightside of all the models shown here.

where both absorption and emission features are present. Additionally, the emission features are blueshifted and the absorption features are redshifted at the orbital phase of 0.25, with the opposite direction in the shifts at 0.75.

We can understand this behavior by looking at Figure 4.2 and animated Figure 4.5, which highlights the spectra and corresponding temperature map at each phase. When looking at the line of sight velocities at a phase of 0.25 for example, we see both redshifted and blueshifted components near the limbs which results in the emission features possessing a different net shift than the absorption features coming from the opposite limb. This effect would only be present in spectra of sufficient spectral resolution as lower resolutions could result in flat, featureless spectra at these phases. We can roughly estimate the minimum spectral resolution needed to detect both the absorption and emission components by using $R \sim \frac{\lambda}{\Delta\lambda}$ where λ is the line center of the non-Doppler shifted spectra and $\Delta\lambda$ is the difference between the peak of the emission feature and the trough of the absorption feature. When applied to the feature shown in Figure 4.4, this roughly corresponds to a minimum resolution of $\sim 50,000$. Note that in the spectra calculated without Doppler shifts, the absorption and emission features almost balance out, resulting in largely featureless spectra. By taking Doppler shifts at sufficient resolution into account, we do not lose the spectral line information. The high-resolution emission spectra we present have inherently three-dimensional effects which would not be produced from a one-dimensional model. These effects are especially important and become more computationally complex when considering non-transiting planets (as shown in *Malsky et al.*, 2021). In non-transiting cases, even at phase of 0.5, part of the nightside hemisphere will be visible which influences the resulting high-resolution spectra. As more high-resolution observations are taken, it will be critical to take into account multi-dimensional effects.

While Figures 4.3 and 4.4 allow us to view by eye the change in absorption features to emission features as a function of phase, it is helpful to examine this trend quan-

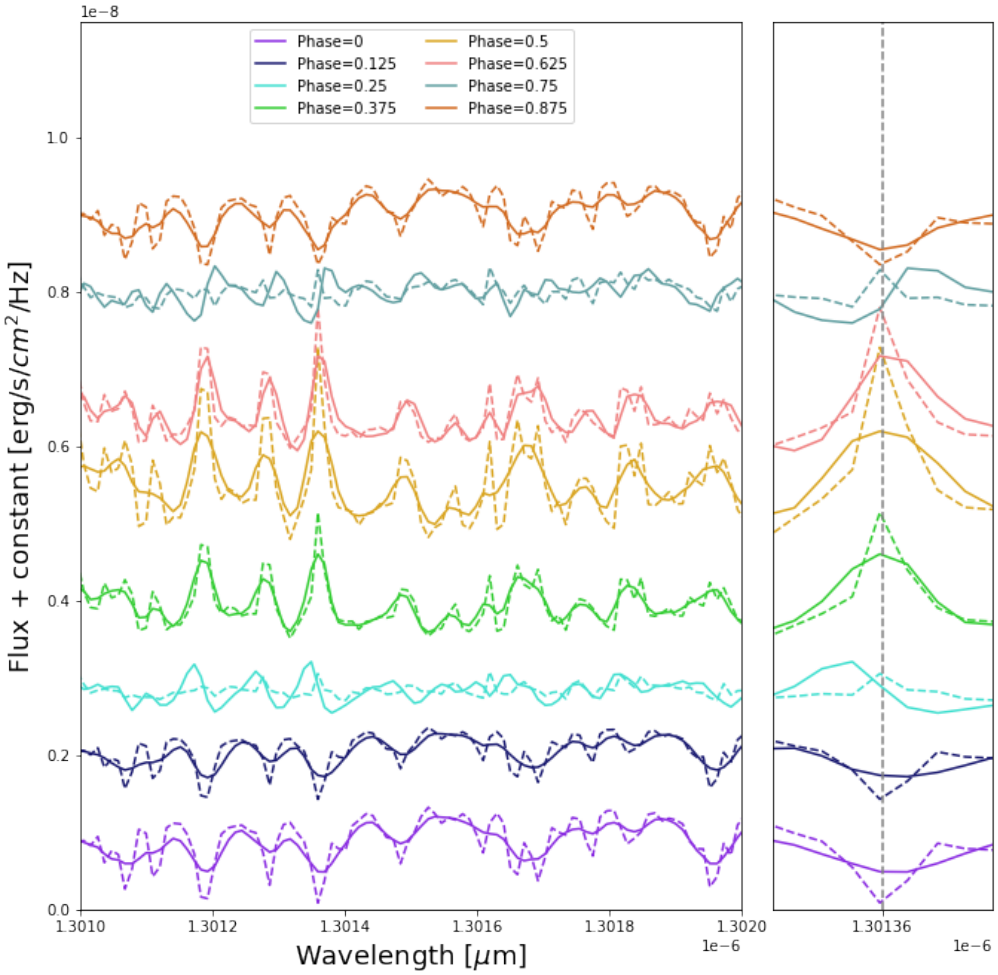

Figure 4.4 Emission spectra generated throughout the orbit of our 3G model planet. The solid lines show spectra that have been calculated including Doppler shifting from winds and rotation, while the dashed spectra do not include those effects. The bottom of the plot starts with the spectrum at a phase 0 (corresponding to transit, when the nightside of the planet faces us) and moving up the y-axis moves forward with time (including arbitrary offsets in flux to separate the spectra). On the side panel on the right, a single feature is isolated with a grey vertical dashed line showing line center for the Doppler off case. The feature begins as absorption at phase 0, due to the fact we are viewing entirely the nightside of the planet. Moving forward with time (increasing orbital phase), we can see the feature switch to emission as parts of the planet with temperature inversions come into view (with full dayside at a phase of 0.50) and then back to absorption again. Additionally, the line center is redshifted and blueshifted slightly throughout the orbit due to line-of-sight velocities from the planetary winds and rotation.

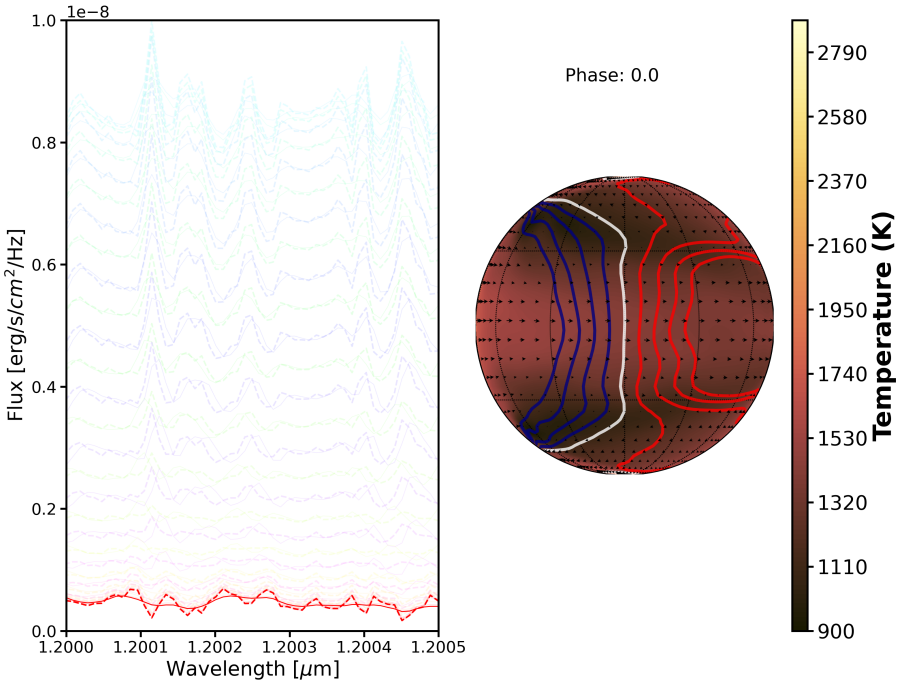

Figure 4.5 A comparison between the temperature and line-of-sight velocity structure visible on the planet (*right*) and the disk-integrated emission spectrum (*highlighted, left*) at each phase from our 3 G model. As the planet rotates and different regions come into view, the corresponding spectra will vary accordingly. Spectra with emission features are emitted from the hot dayside regions, where temperature inversions exist, while the cooler nightside regions emit spectra with absorption features. The line-of-sight velocities, due to winds and rotation, modulate the net Doppler shift of these different spectral components. This figure is available as an animation in the HTML version of the final article. The 10 second animation shows the planet rotating from a phase of 0 (shown in the static image) throughout its entire orbit. As the planet rotates, the temperature and wind fields change and the corresponding emission spectra is highlighted on the left. During the first half of the animation, the hotter dayside comes into view, increasing the continuum level of the emission spectra. At a phase near 0.5, the dayside of the planet is in view and the corresponding emission spectrum has the highest flux continuum level. Additionally, as the dayside of the planet comes into view the spectral features switch from absorption lines to emission lines. From phases 0.5 to 1.0, more of the nightside starts to come into view and the continuum level of the flux decreases and the spectral features switch back to absorption lines.

titatively. By generating spectra with and without water, we can subtract one from the other to isolate the water features, both in emission (positive) and absorption (negative). Using numerical integration, the absorption and emission components are summed at each phase. Spectra without Doppler effects were used to generate this plot, so all differences are a result of differing temperature structures between the models. In Figure 4.6, we show the integrated line flux (positive for emission, negative for absorption) for water features (the most prominent source of opacity within the 1.14 μm to 1.35 μm wavelength range) from our 3 models. The shape of all three curves match basic predictions: emission peaks at an orbital phase of 0.50 and absorption peaks at a phase of 0. Interestingly, the uniform drag model consistently shows the strongest integrated emission while the 0 G has the strongest integrated absorption. Another detail to note from this figure is that the models do not transition from emission-dominated to absorption-dominated at the same phase. These differences in the intensity and orbital phase dependence of spectral features are a result of complexities in the models' corresponding temperature structures, which vary based on the strength and type of magnetic drag applied.

4.5.3 Cross-Correlation Results

Another way to combine information from multiple lines within the planet spectra is to use cross-correlation to effectively integrate over all spectral lines, which is typically how signals are extracted from HRS observations. As described previously, two types of spectra are generated at each phase: Doppler on (which contains broadening and line shifting from winds and planetary rotation) and Doppler off (which contains none of this broadening). By cross-correlating the Doppler on version of the spectrum with the Doppler off version (in velocity space), the peak of the cross-correlation function (CCF) will tell us the net Doppler shift of the signal, while the width of the cross-correlation function quantifies the total amount of broadening in the spectrum

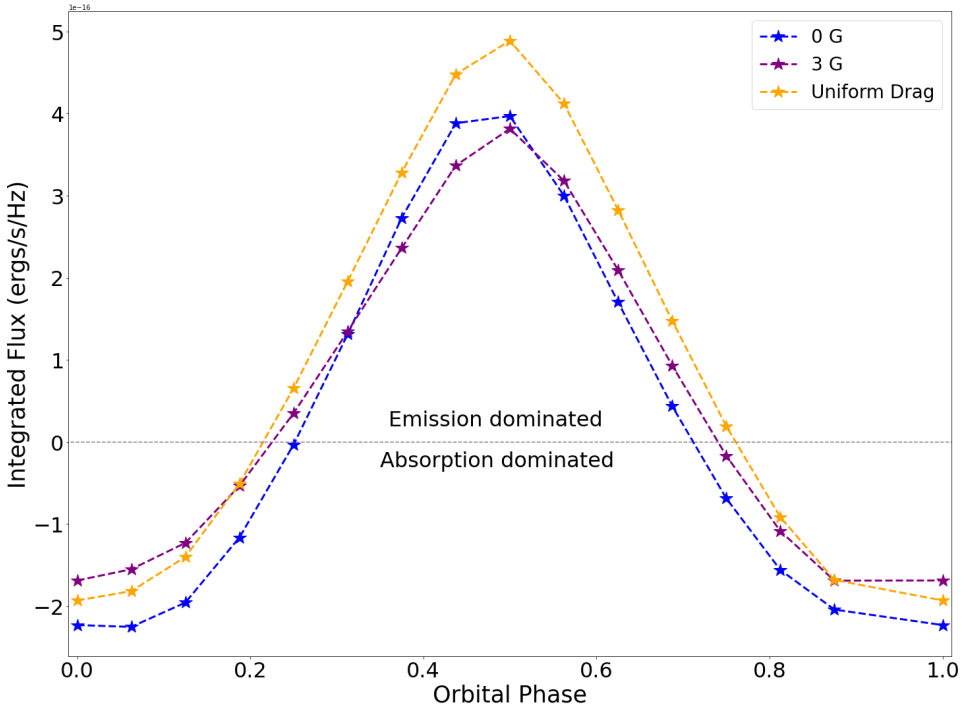

Figure 4.6 The integrated line flux for the three models in this paper, as a function of orbital phase. From this plot, we see that the emission lines from the uniform drag models are consistently the strongest in the emission dominated regime and the 0 G model has the strongest absorption features. Another interesting aspect is that the model spectra switch between being dominated by emission vs absorption lines at different orbital phases.

(see Figure 9 in *Beltz et al.*, 2022b, for example).

Figure 4.7 shows a series of cross-correlation functions from each of our 3 GCMs. At each phase, different parts of the planet's temperature and velocity fields are within the observable hemisphere, which influences the broadening and net shift of the spectra. *Zhang et al.* (2017) first calculated simulated high-resolution emission spectra from 3-D models of three hot Jupiters (without any added drag) and found some similarities in the patterns of net Doppler shift versus orbital phase between those planets (their Figure 7). We see that our Doppler shifts reach higher absolute values, likely due to the more extreme winds and faster rotation of our UHJ; our 0 G model is the most similar to their results for WASP-43b, the fastest rotator (and one of the more highly irradiated) of their set. Similarly to *Zhang et al.* (2017), the net Doppler shift varies in sign and magnitude throughout orbit, as different parts of the planet rotate into view. However, the spectra presented here have their peak redshifts slightly later in phase (~ 0.75) compared to the ones from *Zhang et al.* (2017) which peak in redshift closer to a phase near 0.61.

These net Doppler shifts are informed by the temperature structure of the planet, which we see in Figure 4.2 and animated Figure 4.5. For example, looking at a phase of 0, we see that the the drag-free model has a warmer, brighter region on the left because the equatorial jet has advected that gas around from the dayside, which aligns with the blueshifted velocity structure, resulting in a net blueshifted CCF value at this phase. In contrast, the temperature pattern on the nightsides of the dragged models is more complex, with cooler regions somewhat associated with blueshifted structure, ultimately resulting in net redshifts. At phases where much of the dayside is in view ($\sim$0.25-0.75), the spectra from drag-free and uniform drag models show similar behavior in their net Doppler shifts, with a slow trend of increasing net shift with orbital phase (i.e., the spectra move from blue- to red-shifted). Our active drag model, however, displays more complex behavior, where this overall trend is disrupted

by a superimposed net redshift to blueshift pattern right around 0.50. At phases where much of the nightside is in view (< 0.25 and> 0.75) the drag-free model shows opposite net shifts than the 3 G and uniform model. This is a significant result: The net Doppler shift in nightside spectra may be indicative of the presence of magnetic drag (if redshifted) or not (if blueshifted). A thorough analysis of velocity precision for HRS emission spectra has yet to be done, but theoretical work on simulated CRIRES data in *Brogi and Line* (2019) constrain water and CO's corresponding velocity with errors as small as ± 0.93 km s^{-1} and ± 0.26 km s^{-1}, respectively. At this level of precision, the differences between the Doppler shifts of our models would be feasible to detect. However, we do caution that there may be some wavelength-dependence to these predictions (see Section 4.5.4). This is complementary to evidence for magnetic drag that could appear in net Doppler shift versus line strength trends in transmission spectra (*Miller-Ricci Kempton and Rauscher*, 2012).

Figure 4.8 highlights the danger of ignoring the multidimensionality of planets, as expressed in their emission spectra. The teal curve, which reproduces the peak location of the CCF at each phase, as shown in Figure 4.7, shows the "true" function of peak velocity shift as a function of orbital phase. The orange curve was generated by cross-correlating a single dayside template spectrum—calculated from the 3D model at a phase of 0.50—with the spectra from our 3D model at each phase. The purple curve similarly does this with a single nightside spectrum—corresponding to a phase of 0. At phases near the template spectrum's origin phase, the peak velocity shifts match well with the blue curve. However, the farther away from the origin phase the single template is used, the larger the discrepancy from the true peak velocity. Most notably, at particular phases such as 0.25 and 0.75, the day and nightside templates return net velocity shifts of different signs and at very high net velocity, as these template spectra are just picking out the most red- or blue-shifted component of the observed hemisphere, as the day- or nightside region rotates in or out of view (see

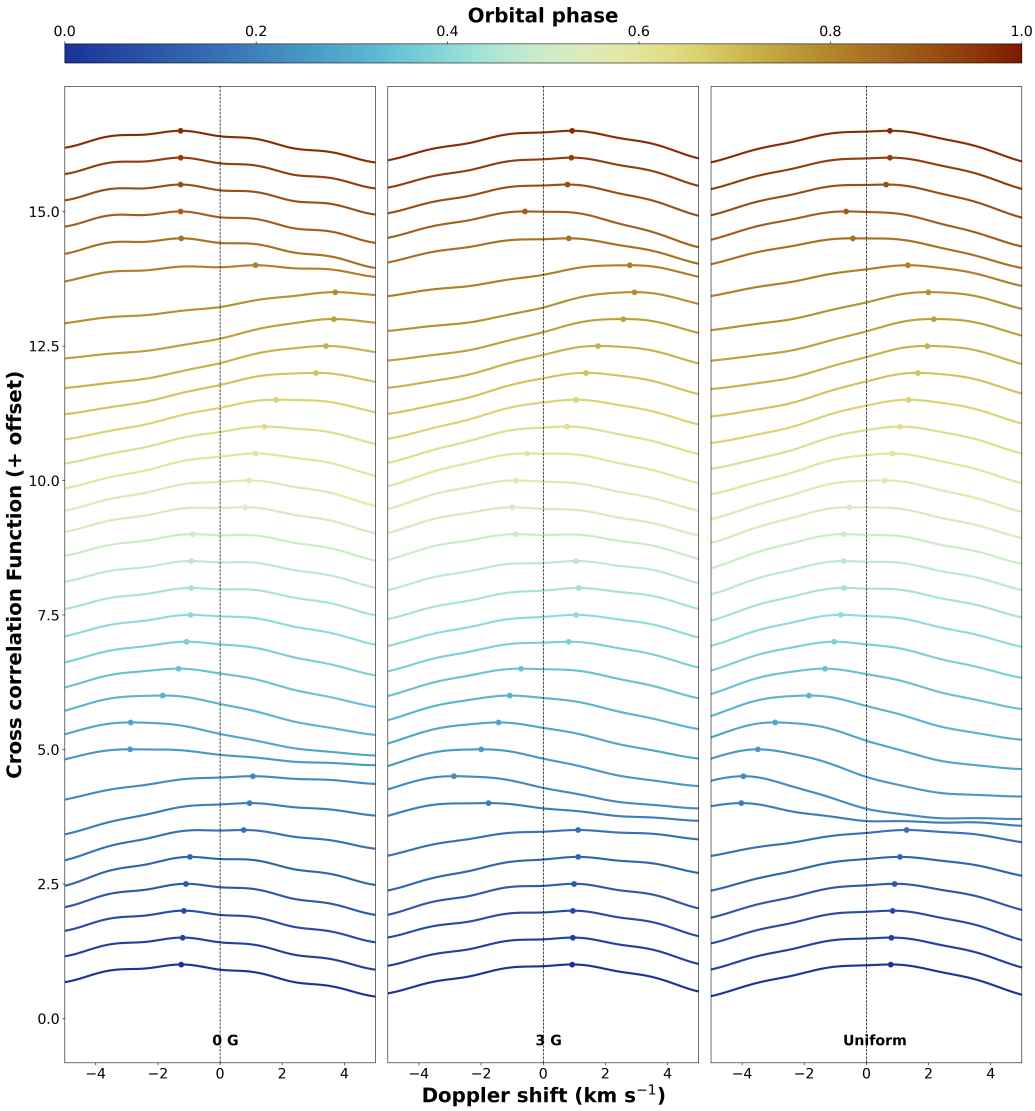

Figure 4.7 Cross-correlation functions of the spectra from our 3 different models throughout the planet's orbit. Each Doppler-shifted spectrum was cross-correlated with its unbroadened counterpoint, with the peak cross correlation value denoted by the colored points. The peak of the cross correlation function quantifies the net shift of that particular spectrum. When different parts of the planet are in view, the net Doppler shift of the corresponding spectra will vary. The drag-free model differs in net Doppler shift from the active and uniform drag models early and late in orbital phase, when much of the nightside is observable. Our active magnetic drag model shows a reversal in the net shift versus orbital phase trend around secondary eclipse (phase of 0.50) that is not seen in the drag-free and uniform drag model.

Figure 4.2).

This figure serves as a warning to observers to ensure the template spectra they use in their data analysis are generated at phases close to the observations. Longer observations over large ranges of orbital phase should use multiple templates for best results and to avoid misleading retrieved net Doppler shifts. While here we find different velocity components due to spatial variation in the planet's thermal structure, a similar effect resulting from spatial variation in chemical abundances may have been seen in *Cont et al.* (2021), who detected two atmospheric species with significant differences in associated velocities in the UHJ WASP-33b. They interpret this large velocity offset to be a result of depletion of TiO (but not Fe) near the substellar point while both species exist on the terminator of the planet. Thus, their cross correlation technique may have detected TiO only near the terminator with large line-of-sight velocity components, which led to a higher velocity offset than the more evenly distributed Fe.

4.5.4 Cross-Correlation at Different Wavelength Ranges

As discussed in Section 5.4, we calculated spectra at two different wavelength ranges: 1.135–1.355 μm (wavelength 1, λ_1), used in all analyses up until this point, and 2.3–2.35μm (wavelength 2, λ_2). In Figure 4.9, we show the Doppler shifts of the three different models at the two different wavelength ranges. Notably, the velocity shifts differ by some amount at each orbital phase tested, in some cases altering the trends identified above. This is a result of the different dominant atmospheric species in the two wavelengths ranges. In λ_1, the dominant absorbing species is water, while in λ_2 it is CO. These two species may be probing different atmospheric pressure levels, which can have different corresponding wind speeds and will result in different net Doppler shifts. In addition, the water abundance varies strongly as a function of temperature, while the CO abundance does not (see Figure 4.1). Since the water

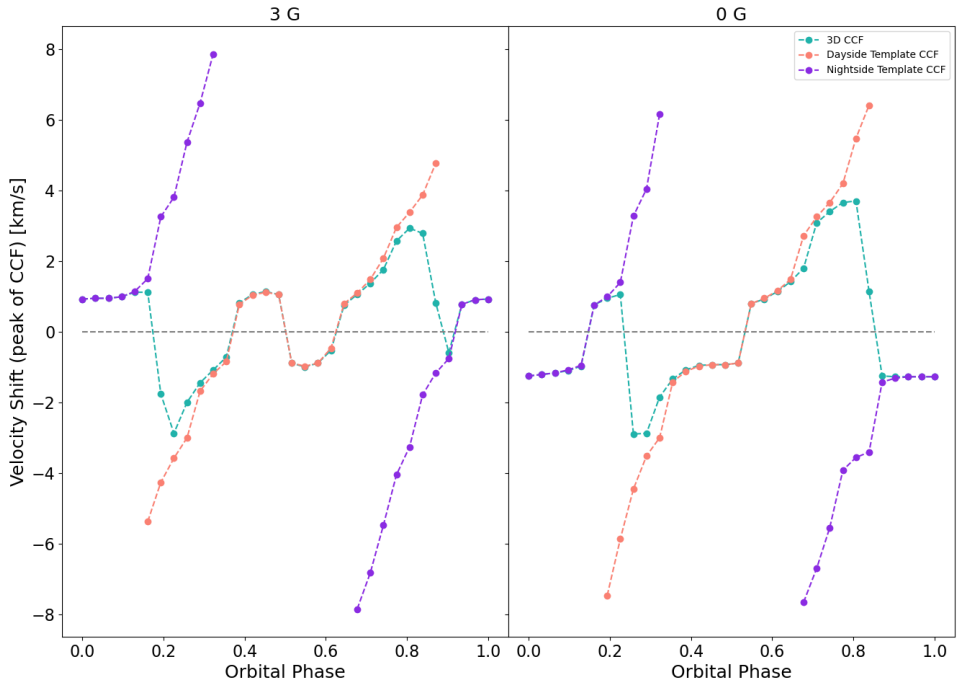

Figure 4.8 Effective retrieved net Doppler shift when using spectra generated as a function of phase (teal curve) compared to using only a dayside template (orange) or a nightside template (purple) against our 3 G model (left) and our 0 G model (right). The blue curve can be thought of as the "true" velocity shifts. While the dayside and nightside models match near their respective orbital phases, once they begin to be used at different phases, their accuracy decreases. At some points in the orbit, such as phases of 0.25 and 0.75, the day and nightside templates will return net shifts of opposite signs. To avoid introducing these errors, spectral templates should be generated as close to the true phase of observation as possible.

opacity relative to CO opacity will therefore be location dependent, this means that the difference between the pressures probed by each wavelength range should also vary with the spatial location around the planet. This is a good demonstration that the 3D structure of the planet's atmosphere influences its emission spectrum in subtle and complex ways.

4.6 Discussion

Important caveats to our GCM are already discussed in great detail in *Beltz et al.* (2022b). We will briefly mention these points here, and invite the reader to examine that work for a more detailed explanation.

Because we have chosen to focus on the effects of magnetic drag in our modeling and post-processing, we are unable to include all the physical processes expected to be present on UHJs. Potentially the most consequential of these is molecular hydrogen dissociation and recombination. This would reduce one of the main effects we see from our active magnetic drag, in that it would result in a reduction in the day–night temperature contrast (*Bell and Cowan*, 2018; *Tan and Komacek*, 2019). We also chose not to include clouds in these models, but work from *Roman et al.* (2021) suggests that if present, cloud coverage would be very minimal and confined to the nightside upper latitudes, due to the high temperatures on the planet. Inclusion of these clouds could alter the nightside temperature structure, potentially warming and cooling at different atmospheric heights. Additionally, depending on the height and opacity of the cloud deck, the strength of absorption features coming from this region of the planet could be muted. The strength of these effects would vary as a function of phase but would likely be most influential near quadrature phases (0.25 and 0.75) where emission features and absorption features are comparable in magnitude and potentially lead to these spectra to become more emission-dominated.

An important caveat to keep in mind when interpreting these results is that our

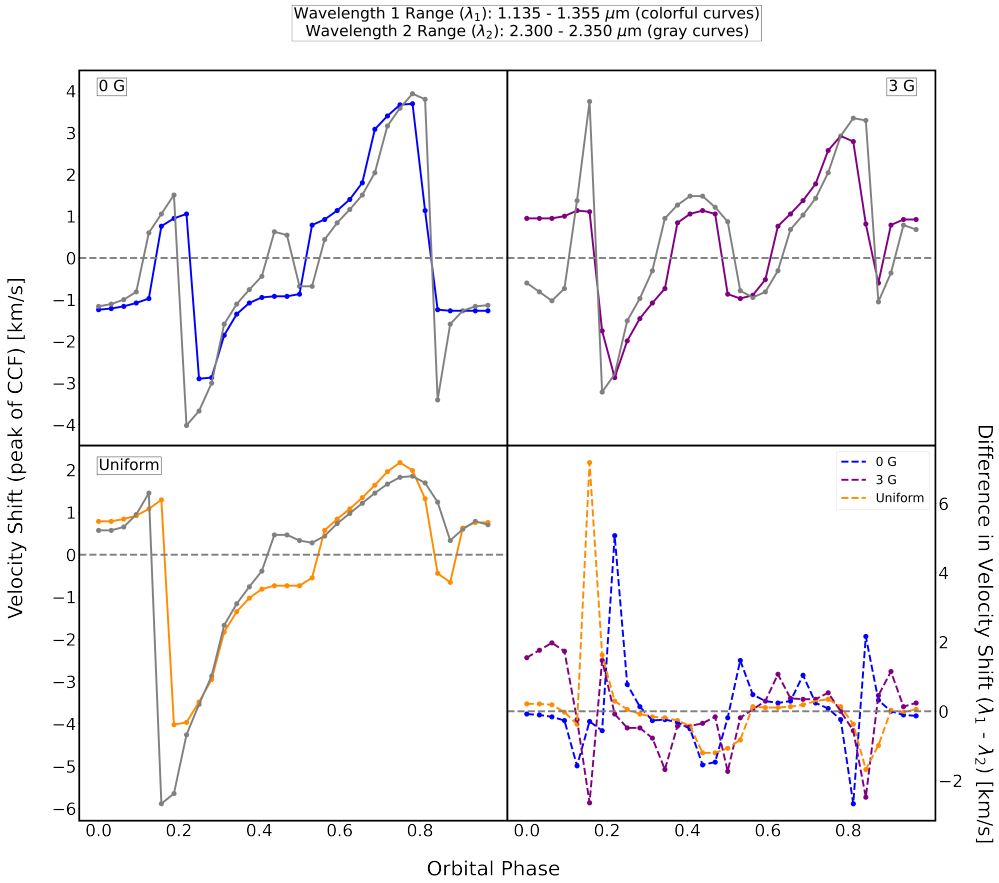

Figure 4.9 Net Doppler shifts versus orbital phase for emission spectra over the two wavelength ranges modeled. The colored lines show the Doppler shifts for wavelength range one, where water is the dominant absorber. The grey lines correspond to the shifts of wavelength range two, where CO is the dominant absorber. The different wavelength ranges probe different pressures in the atmosphere and, due to the temperature dependence of the water abundance, the disparity between the wavelength ranges should be spatially dependent. As such, the net Doppler shifts differ slightly. The bottom right panel shows this difference in net Doppler shift as a function of phase.

magnetic drag prescription is a physically-motivated approximation of the non-ideal MHD equations. Our work assumes the toroidal component of the magnetic field, that is, magnetic field lines in the latitudinal direction, is negligible. Instead, based on our dipole assumption, our magnetic field lines are solely in the poloidal (longitudinal) direction. Models devoted to solving MHD equations, like the ones presented in *Rogers and Komacek* (2014) and *Hindle et al.* (2021b), treat both of these magnetic field components, but have their own limitations, such as pre-calculated local conductivities (that do not self-consistently update as the simulation runs), using a simplified treatment for heating and cooling due to radiative fluxes, and the inclusion of explicit viscosity (resulting in significantly slower wind speeds). Our models and post-processed spectra presented here straddle the bridge between GCMs using simplified uniform drag and dedicated non-ideal MHD models. Our work highlights the ongoing need for model-to-model comparison while still presenting testable observables to gauge the validity of our approximations. Specifically, the results from Figures 4.7, 4.8, and 4.9, are examples of the type of analysis that, if compared to observational data, can test our magnetic drag scheme's ability to approximate the physical environment of UHJs.

One of the crucial assumptions in our drag treatment is that any magnetic field induced in the atmosphere is much smaller than the global magnetic field, a relationship that holds when the magnetic Reynolds number $R_m < 1$. As we show in Figure 1 of (*Beltz et al.*, 2022b), this assumption holds true for the vast majority of the atmosphere except for some parts of the dayside near the low pressure boundary of our model. In order to more physically consistently describe the magnetic effects in this region requires full non-ideal magnetohydrodynamics (MHD). Some 3D non-ideal MHD models exist for (ultra) hot Jupiter atmospheres (*Rogers and Komacek*, 2014; *Rogers and McElwaine*, 2017; *Rogers*, 2017; *Hindle et al.*, 2021b) and show that variability in the circulation pattern (including westward flow near the

substellar point) and the strength of the induced magnetic field may occur in the high magnetic Reynolds number regime.

Since the double-gray radiative transfer in our GCM is agnostic to the specifics of the atmospheric compositions, it was necessary to make assumptions regarding the abundances of species in the atmosphere for our calculation of emission spectra. For simplicity's sake we assumed solar metallicity with abundances set by local chemical equilibrium. Measuring bulk metallicity for an UHJ is difficult, but measurements of water composition (*Kreidberg et al.*, 2014) and CO (*Line et al.*, 2021) as well as results from interior models (*Thorngren et al.*, 2016; *Cridland et al.*, 2019; *Thorngren et al.*, 2019) suggest our choice of solar abundances is reasonable. Work on this planet from *Deibert et al.* (2021); *Landman et al.* (2021); *Wardenier et al.* (2021) all assume solar metallicity for their analysis. *May et al.* (2021) suggest that a lower bulk metallicity could explain the low internal heat flux that is more consistent with the observed phasecurve. On the other hand, *Tabernero et al.* (2021) retrieve a slightly higher than solar metallicity for the host star, which *Casasayas-Barris et al.* (2021) use as justification to also test super-solar composition models. With this uncertainty in mind, more work is necessary to truly understand the metallicity of this planet. As pertains to our results, increasing the metallicity could result in moving the photosphere to slightly lower pressure in our GCM, perhaps with minor changes to the circulation pattern, and would lead to stronger spectral features in the emission spectra. These changes would not likely alter the main results and conclusions presented here.

Another important aspect to consider is that in our calculations we have assumed local thermal equilibrium (LTE). This assumption is true for a majority of the atmosphere modeled, except for perhaps near the top boundary of our model. *Deibert et al.* (2021) found their NLTE model to be a slightly better fit than their LTE model of WASP-76b, but both models significantly underestimated the line depths. Its impor-

tant to note however that their work used transmission spectra, which probes higher up in the atmosphere than emission and therefore we would expect less NLTE effects in the emission spectra presented here. Other work on NLTE effects in UHJs have focused on the hottest known exoplanet to date, KELT-9b. For pressures greater than $\sim 10^{-6}$ bar (which encapsulates all of the pressures probed in our GCM) LTE and NLTE models were nearly identical in predicting hydrogen level populations. In *Fossati et al.* (2021), they use NLTE as a framework for pressures less than 10^{-4} bars when modeling temperature-pressure profiles. For pressures greater than 10^{-4} bars, they note that the retrieved temperature profiles are very similar. Based on these results, we expect that for the pressures modeled in our GCM, LTE is a valid approximation.

It is tempting to extrapolate the trends in net Doppler shifts for the different models presented here to uniquely identify evidence of magnetic effects or estimates of magnetic field strengths. However, even if we take the assumption that the planet's magnetic field is a dipole aligned with its rotation axis to be completely true, these are Doppler shifts for one planet at one wavelength range. Additional physics not included in our model, such as clouds, hydrogen dissociation, or more complex magnetic feedback mechanisms could alter the strength of the predicted Doppler shift. Future work exploring a variety of field strengths and sweeping over a range of planetary parameters would be necessary to draw more quantitative conclusions about minimum field strengths. We can note, however, that our 3G model is the closest match to the phase curve published in *May et al.* (2021). One feasible potential observational test from this work would be the case where if the trend in net Doppler shift versus orbital phase can be measured to sufficient precision, we could differentiate between whether the drag can be approximated with a uniform timescale or is better matched by our more complex treatment. Future observational and theoretical work is therefore needed to determine how robust these predictions are.

4.7 Conclusion

UHJs are planets with strong temperature and compositional gradients due to their extremely short orbital periods and thus are excellent examples of the critical need for 3D models to understand the planet's emission spectra fully. In this work, we explore these 3D effects and illuminate how different forms of drag manifest in high resolution emission spectra. Our main points are as follows:

- The strong temperature and chemical gradient on WASP-76b results in high-resolution emission spectra that vary strongly as a function of phase, showing at times absorption features, emission features, or both. These are inherently 3D features, in particular as the emission and absorption components may have different net Doppler shifts due to their emergence from regions of the planet with different line-of-sight velocities.

- The thermally ionized atmosphere of an UHJ should experience a magnetic drag acting on its winds; this influences the flow pattern in the upper atmosphere and the Doppler shifts in the planet's emission spectra. We predict that the presence of this drag should result in a slight net redshift in nightside emission spectra, compared to the slight net blueshift seen in the drag-free model (both shifts $\sim$1 km/s). In addition, the complex form of magnetic drag may be apparent, over a simpler uniform-timescale drag, in the trend of net Doppler shift versus phase when the dayside of the planet is in view (showing a reversal in behavior around secondary eclipse). We caution that these predictions are dependent on the wavelength of observation.

- Using a single atmospheric template for cross-correlation at multiple phases may be poor matches to the planet, as the spectral features inherently change with viewing geometry. This can bias the recovered net Doppler shifts, especially at phases where parts of both the day and nightside are visible. In the

most egregious cases, the amplitude of the calculated net Doppler shift can misleadingly exceed several km/s, when the inverted or non-inverted region of the planet (producing emission or absorption features, respectively) only appears on the edge of the planet disk, where the line-of-sight velocities from winds and rotation are maximized.

The extreme spatial variations in ultrahot Jupiter atmospheres, exacerbated by the complication of magnetic drag, influence their high-resolution emission spectra. While these signatures can be subtle and highly dependent on the detailed 3D structure of the atmosphere, they may in turn offer us an avenue for empirically constraining those detailed physical properties and processes, possibly with current instruments but likely within the reach of future measurements with Extremely Large Telescopes.

4.8 Acknowledgments

This work was generously supported by a grant from the Heising-Simons Foundation. Many of the calculations in this paper made use of the Great Lakes High Performance Computing Cluster maintained by the University of Michigan. The authors also thank the reviewer for their helpful comments which improved the quality of this work.

CHAPTER V

Magnetic Drag and 3D Effects in Theoretical High-resolution Transmission Spectra of Ultrahot Jupiters: the Case of WASP-76b (Beltz et al 2023)

"I never think of myself as a star because, as somebody once said, 'A star is nothing but a big ball of gas' — and I don't want to be that."

– Dolly Parton

5.1 Preface

Results in this chapter were published in : *Beltz, H., Rauscher, E., Kempton, E., Malsky, I., and Savel, A., 2023. Magnetic Drag and 3D Effects in Theoretical High-resolution Transmission Spectra of Ultrahot Jupiters: the Case of WASP-76b. The Astronomical Journal, 165, 257* and are reproduced here with minor style revisions by permission of the American Astronomical Society under the non-exclusive right of republication granted to authors.

5.2 Abstract

High resolution spectroscopy has allowed for unprecedented levels of atmospheric characterization, especially for the hottest gas giant exoplanets known as ultrahot Jupiters (UHJs). High-resolution spectra are sensitive to 3D effects, making complex 3D atmospheric models important for interpreting data. Moreover, these planets are expected to host magnetic fields that will shape their resulting atmospheric circulation patterns, but little modeling work has been done to investigate these effects. In this paper, we generate high-resolution transmission spectra from General Circulation Models for the canonical UHJ WASP-76b with three different magnetic treatments in order to understand the influence of magnetic forces on the circulation. In general, spectra from all models have increasingly blueshifted net Doppler shifts as transit progresses, but we find that the differing temperature and wind fields in the upper atmospheres of these models result in measurable differences. We find that magnetic effects may be contributing to the unusual trends previously seen in transmission for this planet. Our $B = 3$ Gauss active drag model in particular shows unique trends not found in the models with simpler or no magnetic effects. The net Doppler shifts are additionally influenced by the dominant opacity sources in each wavelength range considered, as each species probes different regions of the atmosphere and are sensitive to spatial differences in the circulation. This work highlights the ongoing need for models of planets in this temperature regime to consider both 3D and magnetic effects when interpreting high resolution transmission spectra.

5.3 Introduction

High resolution spectroscopy (HRS, typically R $\gtrsim$ 30,000) has opened windows into exoplanet atmospheres at an unprecedented level of precision. HRS has allowed for detections of new atmospheric species as well as measurements of net Doppler

shifts and broadening due to atmospheric winds and rotation (*Snellen et al.*, 2010; *Brogi et al.*, 2016; *Schwarz et al.*, 2016). *Brogi and Birkby* (2021) offers a recent review of the techniques and major results of HRS.

Due to the level of precision offered by HRS (and the fact that planets *are* multi-dimensional objects), three-dimensional (3D) atmospheric models are ideal for interpreting these spectra. Previous work has found that not only do 3D effects show up in high resolution transmission (**?***Flowers et al.*, 2019) and emission (*Herman et al.*, 2022; *van Sluijs et al.*, 2022; *Pino et al.*, 2022) spectra, but detection strengths can increase when using spectra generated from a 3D model compared to 1D models (*Beltz et al.*, 2021). Typically the 3D structure of exoplanet atmospheres are simulated with General Circulation Models (GCMs). This type of numerical model solves the set of fluid dynamical equations known as the "primitive equations of meteorology" to simulate a planet's atmospheric structure, its including temperature and wind fields throughout its orbit.

Ultrahot Jupiters (UHJs) are ideal for testing differing treatments of magnetic effects. Due to the thermal ionization of dayside species (*Parmentier et al.*, 2018; *Helling et al.*, 2021), charged particles will be blown around the planet and interact with magnetic field lines generated from the planet's interior dynamo (*Perna et al.*, 2010a). Partially due to their already significant computational time, most GCMs do not have an explicit treatment for magnetic effects in their simulated atmospheres. One commonly used treatment is applying a global uniform Rayleigh drag timescale to the atmosphere such as in GCMs from *Tan and Komacek* (2019); *Carone et al.* (2020); *Deitrick et al.* (2020); *Lee et al.* (2022). Notably this timescale is also sometimes used to encompass a variety of effects, also including hydrodynamical ones. Although easy to numerically implement, this prescription of magnetic drag includes assumptions that become problematic when applied to planets with strong day-night temperature differences. Since the strength of magnetic effects is a strong function

of local ionization levels (and so temperature), order of magnitude estimates of the global field strength corresponding to a particular uniform drag timescale (such as those carried out in *Kreidberg et al.*, 2018) effectively imply that the global magnetic field is nearly two orders of magnitude stronger on the nightside than the dayside, for the case of the UHJ WASP-76b and assuming a 10^4s uniform timescale (*Beltz et al.*, 2022b). Instead, for a uniform global magnetic field, we should expect magnetic effects to be much stronger on the dayside, compared to the negligibly ionized nightside (*Perna et al.*, 2010a; *Beltz et al.*, 2022b).

The most physically consistent treatment of magnetic effects are found in specialized non-ideal magnetohydrodynamic (MHD) models (such as those presented in *Rogers and Showman*, 2014; *Rogers and Komacek*, 2014; *Rogers*, 2017), but at the cost of simplifying other aspects of the modeling such as the treatment of radiative transfer(see *Beltz et al.*, 2022b, for a more detailed discussion) , and greatly increased computational time required, resulting in less than a handful of these types of models having been published for UHJs. In this work, our models use a medium complexity "kinematic MHD" approach, allowing the strength of the drag timescale to vary as a function of temperature, pressure, and latitude. (For a more detailed description of this approach, see *Rauscher and Menou*, 2013; *Beltz et al.*, 2022b).

UHJs are the ideal laboratory for exploration with high-resolution spectroscopy due to their extremely favorable signal to noise ratio caused by their size and temperature. Here, we specifically focus on the UHJ WASP-76b, an inflated gas giant orbiting an F-type star with a period of 1.81 days (*West et al.*, 2016). High resolution transmission spectra for this planet have been observed and studied extensively (*Casasayas-Barris et al.*, 2021; *Deibert et al.*, 2021; *Landman et al.*, 2021; *Tabernero et al.*, 2021) with a recent work (*Kesseli et al.*, 2022) exploring the wide range of species detected in the atmosphere of the planet. An influential transmission result by *Ehrenreich et al.* (2020) found a spatially asymmetric and extremely large blueshift

(−11 km/s) of neutral iron, arguing this blueshift is a result of nightside condensation of the species. Alternate physical processes have been suggested to explain this large blueshift, including clouds, non-zero eccentricity (*Savel et al.*, 2022b), or large temperature differences between limbs (*Wardenier et al.*, 2021), but so far, it has been difficult for GCMs to match this magnitude of shift. A recent work by *Gandhi et al.* (2022) performs a deep analysis on this dataset, providing constraints on both temperature and Fe abundances for four different regions of the planet and confirming spatial differences across the terminator.

In this work, we explore modeled high-resolution transmission spectra for three different models of the UHJ WASP-76b: one with a Uniform drag timescale, one with our kinematic MHD approach, and one without any treatments for magnetic effects. The difference in temperature and wind structures of these three different models result in spectra that vary throughout transit, opening the door to the exploration of how magnetic effects can alter high resolution transmission spectroscopy. This work represents the first time the impact of magnetic drag assumptions on high resolution transmission spectra has been studied (we similarly explored the impact of magnetic effects on high resolution emission spectra in *Beltz et al.*, 2022a). By identifying measurable differences between high resolution transmission spectra simulated using different prescriptions for magnetic effects, we can hope to predict how we might empirically constrain the role of magnetism in UHJ atmospheres.

In Section 5.4, we briefly describe the models used in this analysis and the different treatments for magnetic effects we tested. We also discuss our radiative transfer post-processing and choice of wavelength ranges to generate our predictive spectra. In Section 5.5, we explore the features of our predicted spectra and examine the impact of magnetic model and wavelength choices. We then put this work in context of the model's assumptions and other capabilities in Section 5.6. Finally, we summarize our main conclusions in Section 5.7.

5.4 Methods

5.4.1 GCM

For this work, we post-process previously generated 3D GCMs of the ultrahot Jupiter WASP-76b (first published in *Beltz et al.*, 2022b, where more details and specific numerical parameters can be found) using a ray-striking radiative transfer code to generate high-resolution transmission spectra at multiple wavelengths and resolutions. These models used the RM-GCM (*Rauscher and Menou*, 2012; *Roman and Rauscher*, 2017) with parameters appropriate for WASP-76b, with 65 vertical layers evenly spaced in log pressure, from 100 to 10^{-5} bars, and a horizontal spectral resolution of T31, corresponding to roughly ~ 4 degree spacing at the equator. The simulations ran for a total of 2000 planetary days. Our GCM assumes hydrostatic equilibrium, which is a valid assumption for the opacity sources included in the high-resolution spectra we calculate from these models. This is relevant to note as recent work from *Zhang et al.* (2022) finds that absorption strength of particular species often detected in transmission of UHJs, such as FeII and Hα can't be explained from hydrostatic equilibrium assumptions. This is not an issue for our work due to our choices of opacity sources.

The models from *Beltz et al.* (2022b) were calculated for several different magnetic drag prescriptions at a variety of field strengths; we choose to analyze the same subset of models as in we did in *Beltz et al.* (2022a). These models differ in the way they treat magnetic effects, as follows:

- Drag Free/0 G: This is the baseline model that contains no additional forms of drag to represent magnetic effects. The GCM does contain numerical hyper-dissipation and three sponge layers (see *Beltz et al.*, 2022b, for a discussion on sponge layers in GCMs), both of which are used for numerical stability and are also present in the models listed below.

- Uniform/10^4 s: This method of applying drag is often found in GCMs due to its numerical simplicity. A single Rayleigh drag timescale—in this case 10^4 seconds—is applied throughout the simulation to the horizontal and vertical momentum equation. This value was chosen to match the strong drag case from (*Tan and Komacek*, 2019) and provide the same comparisons as the analysis work presented in *Beltz et al.* (2022a).

- Active drag/3 G: This method for treating magnetic effects, first used in *Rauscher and Menou* (2013) and first applied to UHJs in *Beltz et al.* (2022b) is the most physically complex treatment of magnetic effects that we test. Our active drag prescription, also sometimes referred to as a "Kinematic MHD" treatment, also applies a drag on the winds, but only in the east-west direction (as geometrically appropriate for a dipole global field *Perna et al.*, 2010a) and with a timescale calculated based on local conditions, using the following expression from *Perna et al.* (2010a):

$$\tau_{mag}(B, \rho, T, \phi) = \frac{4\pi\rho\ \eta(\rho, T)}{B^2 |sin(\phi)|} \tag{5.1}$$

  where B is the chosen global magnetic field strength (in this case 3 G), ϕ is the latitude, ρ is the density, and the magnetic resistivity (η) is calculated in the same way as *Menou* (2012):

$$\eta = 230\sqrt{T}/x_e \text{ cm}^2 \text{ s}^{-1} \tag{5.2}$$

  where the ionization fraction, x_e, is calculated from the Saha equation, taking into account the first ionization potential of all elements from hydrogen to nickel (as in *Rauscher and Menou*, 2013).

There are currently no direct observational constraints on the magnetic strength of this planet, or any exoplanet for that matter. Although in *Beltz et al.* (2022b) we present a variety of active drag field strengths (0.3 G, 3 G, and 30 G), we are

primarily focusing on the 3 G model, as it is the best match for previously published *Spitzer* phase curves from *May et al.* (2021) (as shown in *Beltz et al.*, 2022b). We previously found that varying the magnetic field strength changed how deep the magnetic circulation regime—characterized by dayside flow up and over the poles—persisted. All of these models exhibit this magnetic circulation at the high pressures probed by high-resolution transmission spectroscopy. Thus, we chose the 3 G model as a representative for the active drag models. This field strength is also in line with estimates from interior modeling by *Yadav and Thorngren* (2017).

It is important to acknowledge that our GCM currently does not consider H_2 dissociation and recombination. This process is expected to reduce the day-night temperature contrast (*Bell and Cowan*, 2018; *Pluriel et al.*, 2020) of UHJs. Another important result of dissociation is the change in scale heights throughout the atmosphere. On the dayside, the mean molecular weight is decreased due to the dissociation, thus increasing the scale height. However, at the same time, the temperature of this region is decreased, meaning a potential reduction in scale height. The nightside wouuld show the opposite trend (increasing in temperature and mean molecular weight). Recent work from *Savel et al.* (2023) explores the effect of scale height differences in limb asymmetry during transit. Future work should explore the interaction between this process and magnetic effects.

The temperature distributions of the models, for the near-terminator regions probed by transmission spectroscopy, are shown in Figure 5.1, which plots the temperature structure at a slice of the planet as it would be oriented during ingress, mid-transit, and egress. Note that only the upper atmosphere (maximum pressure of $\sim$0.1 bars) is shown and the relative size between the atmosphere and planet core is not to scale. From this plot, we can see that the spatial vertical extent of each limb varies throughout transit, with the hotter regions being much more extended. The 3 G active drag model shows the most variation across the limbs at ingress and egress

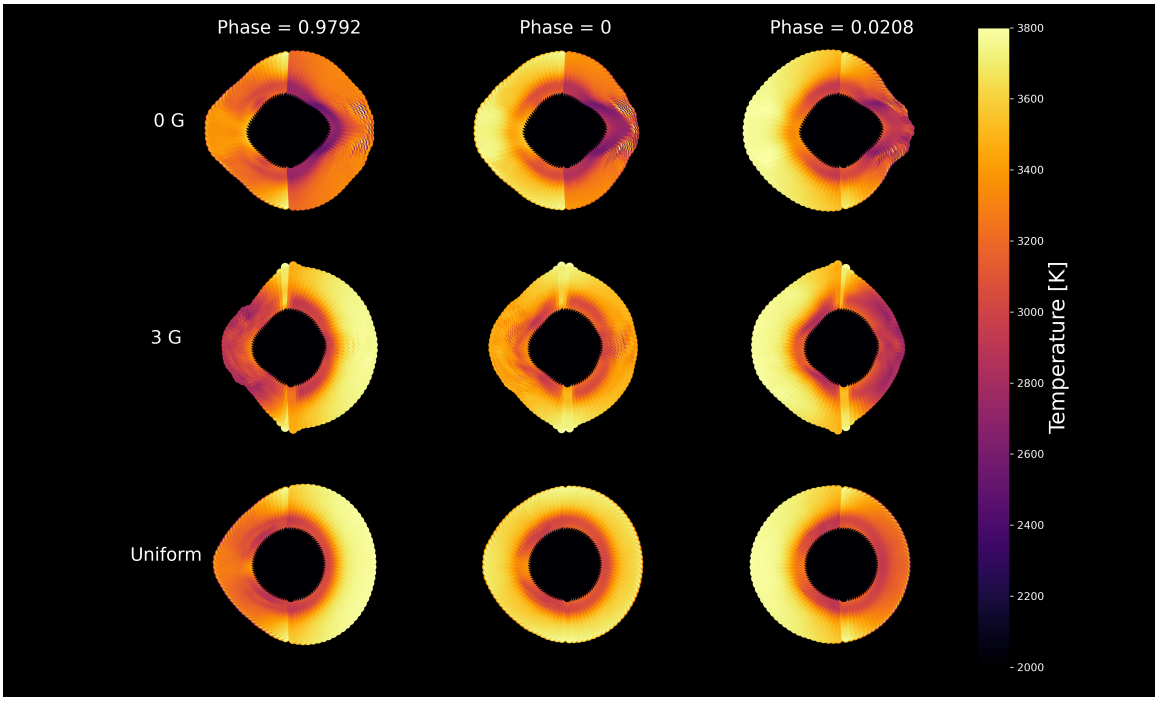

Figure 5.1 Temperature projections for the three models used in this analysis, for pressures less than ∼0.1 bars. Note that the core and atmosphere are not to scale, but the relative altitudes at different locations are accurately plotted. The east and west limb asymmetries in spatial extent is a result of the difference in scale heights of each region due to non-uniform temperatures between the east and west terminators. Because of the planet's short orbital period, it rotates considerably ($> 30^o$) between ingress to egress, which is reflected above.

but at transit center the 0 G model shows the strongest temperature variation. This is directly related to the fact that the 3 G model has the largest day-night temperature contrast of the models considered and that this planet rotates $> 30^o$ throughout the entire transit.

It is also important to consider the line of sight velocities due to strong winds of each model, as shown in Figure 5.2. As the transit proceeds, the planet rotates, allowing different parts of the atmosphere and their associated winds to come into view. These winds will directly influence the net Doppler shifts associated with each model. We delve deeper into these calculations in section 5.5, but by eye one can notice that the 3 G model has the strongest redshifted regions of the three and the

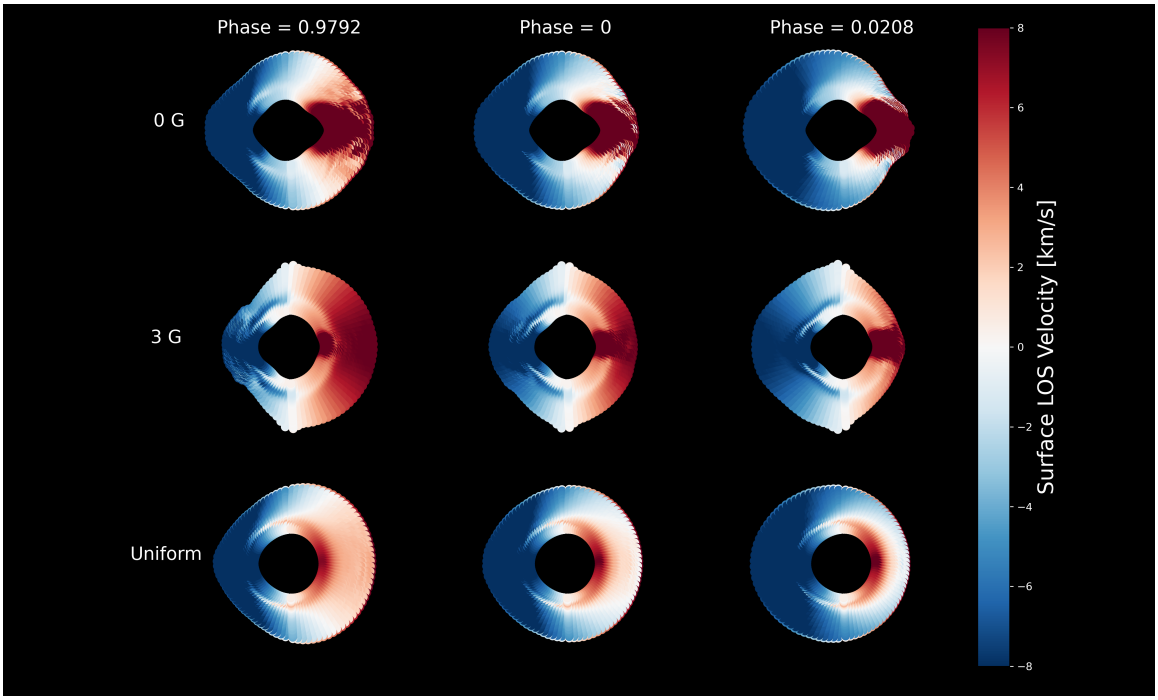

Figure 5.2 Line of sight velocities for the three models considered in this work at ingress, mid-transit, and egress. Throughout transit, the blueshifts dominate the net Doppler shift for all models, though the magnitudes of the net Doppler shifts are both model and wavelength dependent.

Uniform drag has the strongest blueshifted regions. One can additionally see that the 0 G model displays some high-altitude and high-latitude winds that are blowing in the substellar-to-antistellar direction. But, since that direction includes an east-west component, this flow structure is disrupted in the 3 G active magnetic drag model and so that blue-shifted contribution to the net Doppler shift is removed.

5.4.2 Radiative Transfer

We use the same method of calculating high resolution transmission spectra that accounts for 3D effects as that described in detail in *Miller-Ricci Kempton and Rauscher* (2012); *Savel et al.* (2022b). In short, the output from our GCM (containing temperature values, east-west wind speeds, and north-south wind speeds at every grid point) is interpolated onto a constant altitude grid so that the post-processing radiative transfer can consistently implement line-of-sight ray striking that calculates intensity and then transit depths at each wavelength. During this process, winds from the GCM and the planet's bulk rotation are incorporated via Doppler shifts in the local opacities. Stellar limb darkening effects are accounted for, meaning that as the planet progresses through transit, the projected stellar flux illuminating each region of the planet's atmosphere is adjusted based on the limb-darkening coefficients found in *Ehrenreich et al.* (2020).

5.4.2.1 Calculated Transmission Spectra

We calculate high resolution transmission spectra from our three models for three different wavelength ranges, each with a different opacity source of interest:

- Wavelength 1: 0.379-0.789 μm; R=400,000; Opacity source: Fe
- Wavelength 2: 1.135-1.355 μm; R=125,000; Opacity source: H_2O
- Wavelength 3: 2.3-2.35 μm; R=125,000; Opacity source: CO

The latter two wavelength ranges match the work done in *Beltz et al.* (2022a). The opacity sources of particular interest are noted above, but both sets contain opacity from the following six species: CO, H_2O, TiO, VO, K, and Na. Relative abundances of these species were calculated assuming solar-abundance (*Lodders*, 2003) equilibrium models with `FastChem` (*Stock et al.*, 2018, 2022). Wavelength range 2 covers a range accessible by multiple high-resolution spectrographs including WINERED (*Ikeda et al.*, 2016) and CARMENES (*Quirrenbach et al.*, 2014). Wavelength range 3 overlaps with the IGRINS instrument (*Park et al.*, 2014a). Both of these wavelength ranges are probed by the CRIRES+ instrument (*Follert et al.*, 2014). The first wavelength range matches the observations of this planet taken by the ESPRESSO spectrograph, first published in *Ehrenreich et al.* (2020). This set is also unique in that the only included source of opacity is Fe.

The choice of opacity sources is motivated by theory and observational results. To start, each of these three species are expected to absorb strongly in their corresponding wavelength range (*Kurucz*, 1995; *Rothman et al.*, 2010; *Polyansky et al.*, 2018; *Stock et al.*, 2018). Fe was chosen to allow a direct comparison to the data presented in *Ehrenreich et al.* (2020). We chose CO due to its expected near uniform abundance (as shown in Figure 1 of *Beltz et al.*, 2022a). Additionally, recent work from *Savel et al.* (2023) suggests CO represents an ideal tracer molecule for UHJ atmospheres, given this expected uniformity in abundance in these atmospheres. Finally, we chose to examine H_2O due to its lack of uniformity in abundance (*Parmentier et al.*, 2018). The daysides of UHJ are hot enough to disassociate water, reducing its abundance on the hotter limb. The net Doppler shifts resulting from this dissociation provides an interesting comparison to those from the CO spectra.

All spectra were calculated assuming local thermochemical equilibrium and solar abundances. Recent work from *Gandhi et al.* (2022) suggests a metallicity for this planet slightly higher than solar, but consistent with solar within error bars presented.

5.4.2.2 Spatial Distribution of Opacity Sources

The wavelength regimes that we produced spectra for were chosen partly because of the differing main opacity source. Given the extreme temperature contrasts of the planet, our opacity sources are not necessarily uniformly distributed around the planet. We will briefly touch on the spatial distribution of the main absorbers for each wavelength here.

- Wavelength 1, Fe: Fe is expected to have a non-uniform abundance distribution in the atmosphere. For cooler regions of the planet, Fe is expected to condense, potentially into optically thick clouds.[1] Work from *Savel et al.* (2022b) suggests there would be more Fe on the eastern limb of the planet. Additionally, *Wardenier et al.* (2021) found a lack of gaseous iron on the western limb allows for the signal from *Ehrenreich et al.* (2020) to be reproduced.

- Wavelength 2, H_2O: Given that the dayside is hot enough to thermally disassociate water, which is accounted for in the radiative transfer, the abundance of water between the morning and evening terminators differs by roughly 3 orders of magnitude for the 0 G model, but less than one order of magnitude for the other models.

- Wavelength 3, CO: Given the extremely strong triple bond of this molecule, even UHJ atmospheres will not dissociate this species (*Parmentier et al.*, 2018; *Savel et al.*, 2023). Additionally, the night side is warm enough such that CO is not expected to convert into methane. Thus, its global distribution is essentially uniform the planet.

[1]Notably, these models were ran without active clouds, so Fe condensation is applied in the radiative transfer post-processing.

5.5 Results

We begin our analysis by first searching for differences in the spectra by eye. In Figure 5.3 we show the calculated transmission spectra at mid-transit (phase=0) for all three models from a subset of wavelength range 3 (2.3-2.35 μm) for versions of the spectra calculated with and without Doppler effects from winds and rotation. The spectra without Doppler effects are difficult to differentiate by eye as the differences between the spectra are on order of 0.5%, but these small differences are a result of differing temperature structures between the models. We more clearly see the differences between the models in the broadened spectra, as these models have unique upper atmosphere wind structures due to the different types of drag applied to each model.

Because WASP-76b rotates significantly during transit, its spectra will vary as different parts of the atmosphere come into view (*Gandhi et al.*, 2022; *Wardenier et al.*, 2022). In Figure 5.4, we show transmission spectra produced from the 3 G model, where Doppler shifts and stellar limb darkening have been applied. Since the spectra are evenly spaced in phase from mid-transit (phase=0), the spectra appear in "pairs" where spectra sharing the same absolute offset from transit have similar continuum levels. These pairs are not identical though; differences in line center (due to differing wind patterns) and absorption strength (due to differing temperature structure) exist. It is also noticeable that during the second half of transit, lines become more blueshifted as the more spatially extended side of the planet increasingly dominates the back-illuminated part of the planet's atmosphere. Similar trends were found in *Savel et al.* (2022b) and *Wardenier et al.* (2021), in line with the trend presented in *Ehrenreich et al.* (2020). Thus, the 3D geometry of the model is making a noticeable difference in the resulting high resolution transmission spectra.

A tool often used in high-resolution spectral analysis is that of cross-correlation between the data and a template spectrum (in velocity space), which we can use to

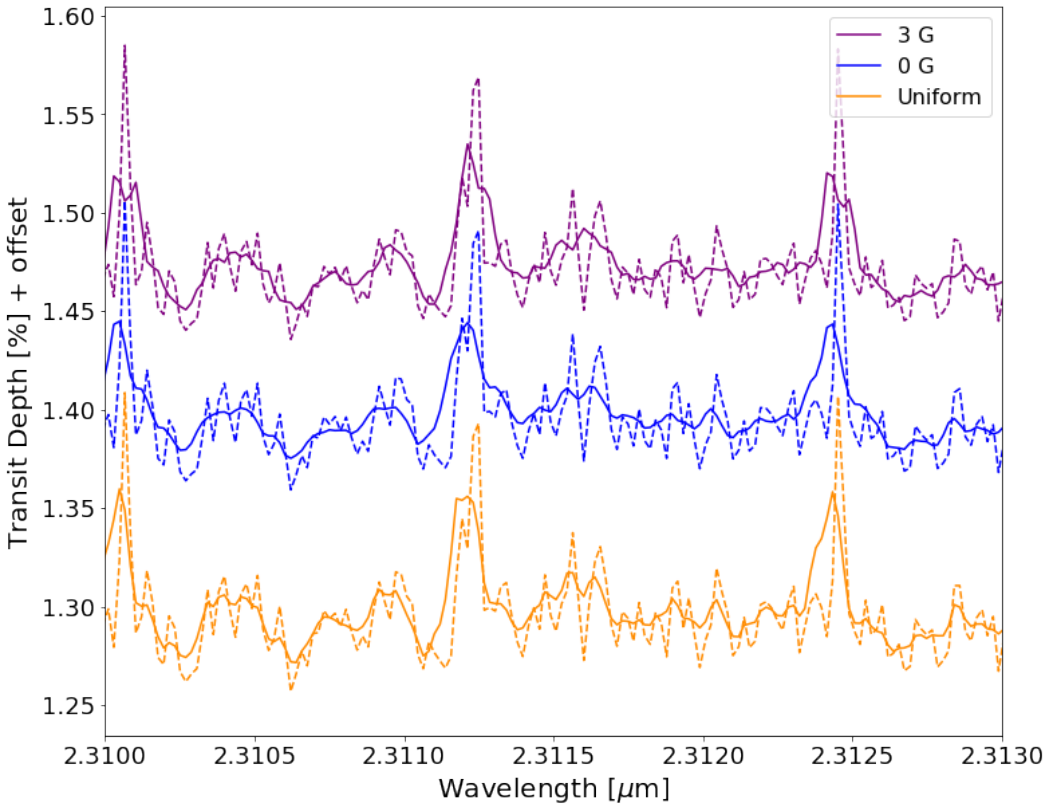

Figure 5.3 Mid transit (phase=0) spectra from our three models. The solid lines show spectra that have been shaped by Doppler shifts due to winds and rotation while the dotted curves do not have this influence. Vertical offsets have been added for clarity. Differences between the spectral features are due to the different temperature and wind patterns of the models. All three models have similar vertical temperature structures, and so the spectra without Doppler effects are only very subtly different, while the different wind patterns between the models result in noticeable differences in the resulting spectra.

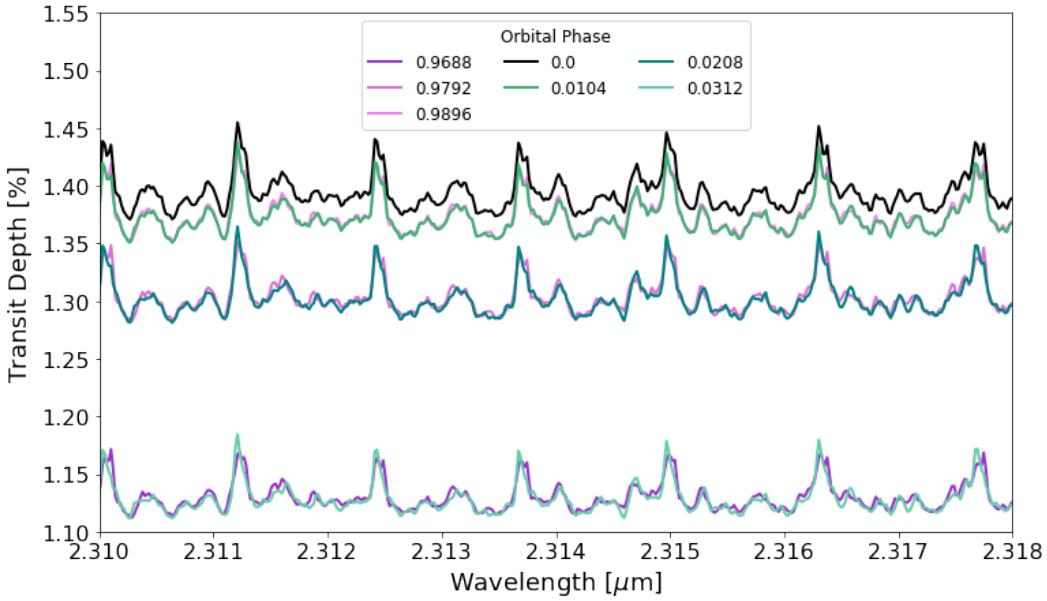

Figure 5.4 Simulated high resolution transmission spectra from our 3 G model, with Doppler effects from winds and rotation, shown at equally spaced times throughout transit. As expected, mid transit (phase=0) has the strongest absorption since the maximum amount of light is obscured by the planet's atmosphere at this phase. The first and last phases shown here are partial transits, which is why their continuum values are lower compared to the other spectra shown. We can compare spectra that are equally spaced in time before and after mid-transit to identify differences due to east-west asymmetries around the terminator. While the phases nearest to mid-transit are very similar, those phases further away show larger differences, with the spectra near the end of transit (where only a portion of the planet is transiting the host star) showing very sharply blue-shifted lines.

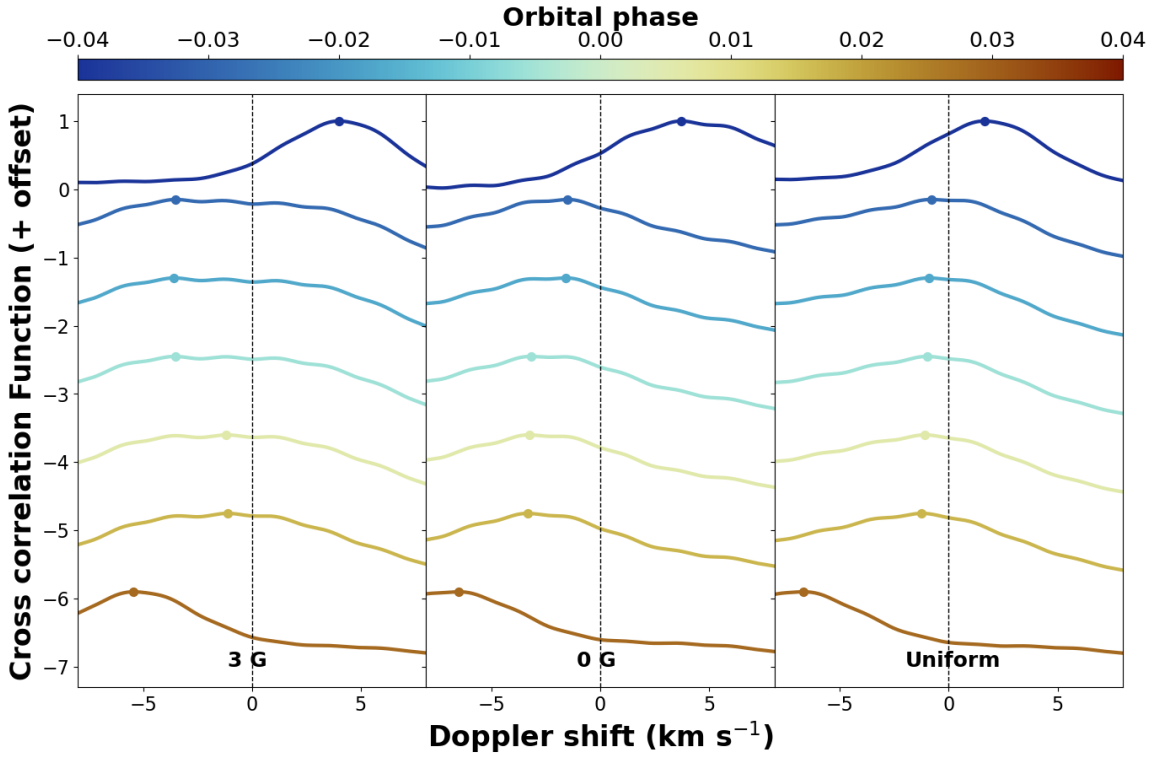

Figure 5.5 Cross correlation curves for each model throughout transit (with the first and last points being partial ingress and egress respectively) for wavelength range 1 (1.135-1.355 μm). The peak of the cross correlation curve, corresponding to the net Doppler shift of the spectrum are shown with colored points. These net Doppler shifts vary with time and differ between models due to the differing circulation patterns. Notably, for this wavelength range, the 3 G spectrum become *less* blueshifted for a time near the end of transit. This is a unique feature of the 3 G model and is a result of the differing wind structure caused by the active magnetic drag prescription.

combine the information from all of the lines in a spectrum. If the Doppler-on version of a spectrum is cross correlated with the corresponding Doppler-off version of the same spectrum, one can determine the net Doppler shift at that phase by finding the corresponding velocity of the peak of the cross correlation function, as shown by the points on the curves in Figure 5.5, calculated for wavelength range 2 (1.135-1.355 μm). Broadly, our models show a changing net Doppler shift becoming more blueshifted with time, due to the increasing contribution from the more extended, hotter eastern limb, whose motions from winds and rotation are oriented toward the observer during transit. Interestingly, the 3 G models are an exception to this for a short time after mid-transit where the net Doppler shift becomes less blueshifted for a brief time before becoming more blueshifted by the end of transit. It is also relevant to note that of all the cross-correlation curves presented in this Figure, the 3 G curves are the most broadened and least peaked, particularly near mid transit. The broadness of these curves can be attributed to the dual existence of strong blueshifted and redshifted winds in the upper atmosphere.

Figure 5.6 shows the net Doppler shifts for all the models considered in this work at each wavelength range. Each model exhibits unique trends but overall, the spectra become more blueshifted throughout transit. The Uniform drag model consistently shows the strongest blueshifts at each phase examined. Similarly, the 0 G model wavelength becomes more blueshifted throughout transit for each wavelength range. The 3 G model shows interesting structure in each wavelength regime, with the spectra covering the near-IR becoming slightly less blueshifted right after mid-transit.

The differences in these net Doppler shifts between models can be attributed to a variety of physical effects. First, the underlying velocity structure of the upper atmosphere differs between each model. For example, in *Beltz et al.* (2022b), we saw significantly different dayside wind structures for the active drag model, with the dayside winds traveling up and over the poles in the North-South direction. The

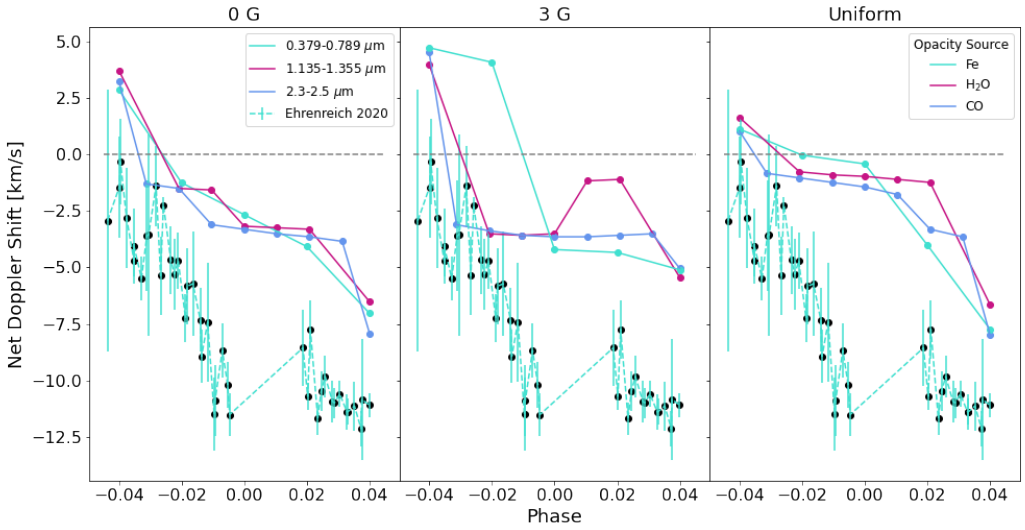

Figure 5.6 Net Doppler shifts for the simulated spectra from each model, over the three wavelength regimes considered, as well as the data from *Ehrenreich et al.* (2020). Overall, the net behavior shows the spectra becoming more blueshifted as transit proceeds. However, the 3 G active drag model shows some deviations from this shortly after mid-transit, but only when water is the dominant absorber within the wavelength range considered. When iron is the dominant absorber, we see instead that the starting net redshift persists longer into transit, before switching to a net blueshift. Both of these behaviors are unique to the 3 G model, distinguishing it from the 0 G or Uniform drag models.

influence of these differing flow patterns can be seen in Figure 5.2. Additionally, differences in relative scale heights due to atmospheric temperature differences will affect the net Doppler shifts (*Wardenier et al.*, 2022; *Savel et al.*, 2023). Figure 5.1 shows this, with the hottest atmospheric regions having the largest vertical extent.

The spatial extent of the dominant opacity source (determined by the wavelength) will influence the net Doppler shift (*Savel et al.*, 2022b). We can start by examining the wavelength range containing CO, as this species is fairly uniform in abundance around the planet. The 0 G and Uniform drag models show similar behavior for this wavelength range, but with the Uniform drag having the strongest net blueshift. We can attribute this to the weakness of the redshifted region on the western limb, which is stronger for both of the other models. For the 3 G case, we see that the net Doppler shift is roughly constant, aside from the first and last phases calculated. This means that although more blueshifted regions are coming into view during transit, this effect is roughly equaled out by the redshifted winds on the western limb and the different scale heights associated with each limb.

Water on the other hand is certainly not uniformly distributed around the planet. This is most easily seen in the case of the wavelength range 2 for the 3 G model, which actually becomes less blueshifted with time for part of egress. Water will dissociate in hot temperatures, so it is less abundant in blueshifted limb. However, as transit progresses, we see a water-depleted blue limb and a relatively water-rich red limb, resulting in a brief period during transit where the spectra becomes more redshifted. Since this effect is not seen to the same degree in the other two wavelength ranges tested, one can infer the feature is influenced by the dominant absorber, water. Although temperature inhomogeneities between the limbs exist for all models presented, the 3 G model has the strongest day-night temperature contrast and most dominant red-shifted atmospheric winds. This particular combination of atmospheric structures results in the behavior seen in Figure 5.6. *Neither the Uniform or 0 G*

models show this behavior, indicating that these net Doppler shifts may be a way of testing approximations of active drag.

Fe abundance is slightly more temperature dependent than CO, but not nearly to the same level as water. While water abundances can very by over 6 orders of magnitude from the dayside to the nightside of this planet, Fe abundances only change by less than a single order of magnitude, and is slightly more abundance in the cooler regions of the planet.

For wavelength range 1 where Fe is the dominant opacity source, , we can also make a direct comparison to the Doppler shifts measured in *Ehrenreich et al.* (2020). Although the data displays stronger magnitudes of blueshifted values than our models predict, the magnitude of this shift can be altered strongly by small changes in orbital parameters (*Savel et al.*, 2022b), leading us to instead focus on comparing the velocity trends with orbital phase between the models and the data. The 3 G model does the best job of reproducing the trend found in the data. Both experience a strong negative slope in Doppler shift shortly before mid transit and roughly constant Doppler shifts throughout the rest of transit. The Uniform and 0 G model have a roughly constant slope which does not match the data as well. Thus, out of the different drag prescriptions tested, our active drag model best matched the trend presented in *Ehrenreich et al.* (2020). Notably, other GCM work has struggled to reproduce this trend—particularly the"bottoming out" or "kink" behavior that occurs after mid transit. *Wardenier et al.* (2021) removed iron from the leading limb of their atmosphere to reproduce this "kink" while *Savel et al.* (2022b) used optically thick clouds and a slight non-zero eccentricity to best fit the data. However, the models from these two works also incorporated uniform drag in their atmospheres. Thus, this interesting behavior in the *Ehrenreich et al.* (2020) dataset may be a result of some combination of magnetic effects, clouds, or Fe condensation, however we refrain from making more detailed predictions until a model with both of these effects in concert

is presented, which we leave for future work.

5.6 Discussion

While we have presented particular features in transmission spectra of UHJs that could be used to assess drag mechanisms within the planet's atmosphere, it is important to recognize the necessary limitations of our modeling and any potential impact this could have on our results.

One caveat to this work is that due to numerical stability purposes, the top boundary of our model is $\sim 10^{-5}$ bars. Compared to emission observations, transmission spectra probe a higher region of the atmosphere, potentially at lower pressure values than what is contained in our model. These regions are less dense with potentially stronger wind speeds. This upper boundary could be contributing to why our net Doppler shifts are not as large in value as those reported in *Ehrenreich et al.* (2020), although other GCMs similarly struggle to produce such large shifts (*Wardenier et al.*, 2021; *Savel et al.*, 2022b, despite these GCMs covering nearly 2 orders of magnitude more in pressure space).

Additionally, the GCMs studied in this work use a double-gray radiative transfer scheme instead of a more complex picket-fence or correlated-k method. A downside of the double-gray method is that it results in more isothermal upper atmospheres than the other radiative transfer schemes mentioned (*Lee et al.*, 2021). This effect is minimized on transmission spectra, which is less sensitive to temperature structure than emission spectra. We also note we chose only one set of infrared and optical coefficients (chosen to most closely match observations presented in *Fu et al.*, 2021). Different choices in these coefficients would lead to slightly different temperature profiles, but this exploration is beyond the scope of this work. Future work will compare the impact of using spectra generated from double gray and picket fence GCMs to determine how robust the patterns identified here are along different radiative transfer

schemes and planet parameters.

A physical process absent from these models are clouds. Clouds should reduce the depth of spectral features and flatten the resulting spectra. Additionally, clouds could potentially sculpt the Doppler fields calculated by blocking out particular regions and create the "bottoming out" trend seen after mid transit in *Ehrenreich et al.* (2020), as discussed in *Savel et al.* (2022b). For a planet of this temperature, one could potentially find some clouds in the nightside upper latitudes (*Roman et al.*, 2021), so we may initially not expect them to have any strong signatures in the transmission spectra. However, those cloudy models were run in the absence of magnetic effects; when the advection of hot gas to the nightside is reduced, we may expect a colder nightside and therefore more cloud formation. Additionally, work from *Helling et al.* (2021) suggests that cloud opacity at the morning terminator and ionic or atomic opacity sources at the evening terminator may influence the resulting transmission spectra for UHJs. However, we leave the interplay between magnetic drag and cloud physics for later work.

Our active magnetic drag 3 G model also makes simplifying assumptions regarding the magnetic field of the planet. (For a detailed explanation of model assumptions, see *Beltz et al.*, 2022b). The most relevant of these assumptions to this work is that any magnetic field induced in the atmosphere is smaller than the global magnetic field. Mathematically, this results in our prescription being most effective when the magnetic Reynolds number, R_m, is < 1. This holds true for the vast majority of the planet's atmosphere, but there is a small region in the dayside upper atmosphere where the values of R_m reach unity or slightly above. However, given that the dayside is never fully in view during transit, this small region of the atmosphere is likely not very influential in the transmission spectra presented here, but would only influence them secondarily through any change in the day-night circulation.

5.6.1 Combining Observations for Detecting Magnetic Effects

In this work, we have identified trends in high resolution transmission spectroscopy of planets in the magnetic circulation regime. We perhaps see this trend in the *Ehrenreich et al.* (2020) data, but to more reliably convince ourselves that this planet (or any other planet) is operating within the magnetic circulation regime, we can combine this trend with others described in *Beltz et al.* (2022b) and *Beltz et al.* (2022a), therefore allowing our conclusion to become more robust. Combining three independent observations (phase curves, high resolution emission, and high resolution transmission spectroscopy) offers a chance to more conclusively identify planets that are strongly influenced by magnetic effects. We summarize these trends below:

- *High Resolution Transmission Spectra:* In this work, we found that for magnetically active models, the net Doppler shift showed less overall blueshifting throughout transit and, depending on the wavelength, could become more redshifted during parts of transit. Neither behavior was shown by the drag free or uniform drag models.

- *High Resolution Emission Spectra:* The magnetic circulation regime influences the net Doppler shift as a function of phase, especially around secondary eclipse for high resolution emission spectra. Our work in *Beltz et al.* (2022a) found that our active drag shows a unique trend in net Doppler shift compared to the ones found in the drag free and uniform models near secondary eclipse (see Figure 7 in that paper).

- *Phasecurves:* Our work in *Beltz et al.* (2022b) found that increasing our magnetic drag strength resulted in a decrease in hotspot offset and an increase in day-night temperature contrast.

This set of three papers and the trends discussed within can act as roadmap for finding exoplanet atmospheres influenced by magnetic effects.

5.7 Conclusion

In this work, we post-processed three different models of the UHJ WASP-76b with varying forms of magnetic drag treatment to generate high resolution transmission spectra for three different wavelength regimes. The main results of this work are as follows:

- 3D effects of both varying temperature and wind structure are present in this high-resolution transmission spectra and alter the line shape and depth of various features, offering an avenue for assessing sources of drag or magnetic effects within the atmosphere.

- While transmission spectra from all models generally show increasingly blueshifted net Doppler shifts as transit progresses, the specific patterns and magnitudes depend on the model and wavelength range (and the dominant source of opacity) considered.

- The 3 G model shows the largest differences in Doppler shifts from the other models, beginning with the strongest net redshift of any model as well as actually becoming less blueshifted from phase 0-0.02 for the spectra generated at 1.135-1.355 μm. This is due to the model possessing the strongest redshifted line of sight velocities during transit, as seen in Figure 5.2, and may provide a unique way to constrain the role of magnetism within UHJ atmospheres.

- Our 3 G model was best able to match the Doppler shift trends in the data presented by *Ehrenreich et al.* (2020) including the "bottoming out" behavior during the second half of transit, which only appeared in the kinematic MHD models. Thus, magnetic effects may help explain this particular dataset.

High resolution spectroscopy has opened the door to planetary atmospheric characterization at an unprecedented level, uniquely probing physical processes which

were previously unobservable. In order to extract the most meaningful, unbiased conclusions from this data, high complexity atmospheric models and sophisticated post-processing routines are needed in order to account for 3D gradients in temperature, winds, and chemical composition. UHJs, due to their favorable signal to noise ratio, remain the best planetary target for investigating analysis techniques for this type of data. However, these planets have the largest spatial gradients and, due to their high temperatures, must have partially ionized atmospheres. It is therefore necessary to consider how magnetic effects may shape the spectra of these planets and, in turn, how those spectra can give us insight into the physical states of the atmospheres.

5.8 Acknowledgments

This work was generously supported by a grant from the Heising-Simons Foundation. Many of the calculations in this paper made use of the Great Lakes High Performance Computing Cluster maintained by the University of Michigan. We thank the reviewer for their comments, which improved the quality of this manuscript.

CHAPTER VI

Concluding Remarks

"Instruments register only those things they're designed to register. Space still contains infinite unknowns"

– Mr. Spock

6.1 Summary

This dissertation set out to explore the questions: "How does the inclusion of magnetic effects change the modeled atmospheres of UHJs, and what techniques can be used to find supporting evidence?" In Chapter II I showed for the first time in the literature that high resolution emission spectra generated from a 3D GCM can out-perform hundreds of 1D models. Importantly, that work found that the biggest increase in detection significance came from using a 3D temperature structure. The inclusion of Doppler shifts and chemistry choices played a secondary role in this increase of detection. Although this work was focused on a Hot Jupiter, identifying the multidimensionality of high resolution emission data is important for the later chapters in this dissertation .

Chapter III presents the first active drag model of an UHJ and introduces the magnetic circulation regime. In this work, I explored different global magnetic field

strengths and compared them to uniform drag approaches. Although both approaches resulted in increased day-night temperature contrast and decreased hotspot offsets, the active drag approach resulted in a circulation regime that could not be reproduced by any of the uniform drag models. In addition, the inclusion of the active drag made our 3 G model the best fit to a published phase curve of the planet.

Chapter IV took the 3 G, 0 G, and strong uniform drag models from *Beltz et al.* (2022b), and post-proccessed them with a radiative transfer routine to generate high-resolution emission spectra throughout the planet's orbit. This work demonstrated how much the structure and shape of the spectra changes throughout orbit due to the different parts of the planet coming into view. At different points, the spectra showed exclusively emission features (when the hot, temperature-inverted dayside was dominating), exclusively absorption features (when the night side of the planet was in view), and both emission and absorption for the same line (at quadratures, where the dayside and nightside are visible). This 3D nature of the planet also contributes to the Doppler shift trends that are influenced by winds dictated from different magnetic prescriptions.

Finally, in Chapter V, the same three models are post-processed to examine their transmission spectra. Here, three different wavelength ranges were tested, each with their own dominant opacity source. The differing spatial extent of each species resulted in wavelength dependent Doppler trends, but to 1st order, the main trend was spectra becoming increasingly blueshifted as transit progressed. The 3 G model showed the most unique behavior of the three, with the lowest net blueshifts and wavelengths where the Doppler shifts actually became less blushifted for parts of transit. This is due to the circulation pattern of the 3 G model, which had some of the strongest redshifted line of sight velocities. The paper concludes by summarizing the behaviors of the active drag models presented in this work and those in *Beltz et al.* (2022b,a), to paint a broad picture of the magnetic circulation regime.

6.2 Overarching Themes

This dissertation presents state-of-the-art modeling and post-processing of the hottest gas giant exoplanets with a particular focus on the role of planetary magnetic fields in shaping atmospheres and observables. The set of three papers presented in the past three chapters represents the most in-depth exploration of magnetic field effects in hot giant gas planets to date. And although the models presented correspond to specific exoplanets, many of the themes and conclusions can be extrapolated to hot and ultrahot Jupiters in general. I touch on these broader themes below.

6.2.1 Planets are Multi-Dimensional

It is an uncontroversial opinion that planets are, in fact, three dimensional objects. However, it is often computationally quicker to calculate thousands of potential 1D models than to run a single 3D GCM to completion. Running large grids of GCMs is not yet computationally feasible[1], so theorists must consider: which planets and which observations should 3D effects matter the most? Hot and Ultrahot Jupiters, due to their tidal synchronization and extreme temperature gradients are the best targets, in my opinion, for detecting 3D effects. At high resolution, our group has shown that 3D effects play a role in both high resolution transmission (*Flowers et al.*, 2019) and emission (*Beltz et al.*, 2021) spectroscopy. Moreover, I showed in Chapter IV that using the same atmospheric template for the planet's entire orbit—a psuedo[2] 1D approach—can bias the returned Doppler shifts. At low enough resolution however, many of the 3D effects are washed out, limiting the benefits of applying a 3D model.

So when are 3D approaches most valuable? From the work I've presented here, high resolution emission spectroscopy (Chapter IV) is a clear choice. To first order, the dayside spectra and nightside spectra show different feature types—emission and

[1] emphasis on the *yet*

[2] The word pseudo is used here because the template was technically generated from a 3D atmosphere. Assuming this template is valid at all phases is where the bias creeps in

absorption lines respectively. At quadrature phases, emission and absorption lines for the same species were *both* present, just at slightly different Doppler shifts. In the future, I hope to carry out a project with a mentee to explore more quantitatively the minimum resolutions necessary to still see these 3D effects in the spectra themselves. For high-resolution transmission spectra, the temperature structure of the upper atmosphere—where transmission spectroscopy probes—varied less from model to model. Additionally, the significantly smaller phase coverage may make 1D models more tempting. However, caution should still be used. 1D models are helpful in this case for detecting particular species, but will be unable to match net Doppler shift patterns of the spectra. The non-uniform spatial distribution of different species in combination with complex wind fields were necessary to match the Doppler shifting trends observed for WASP-76b.

6.2.2 The Magnetic Circulation Regime

Although the first application of our active magnetic drag was by *Rauscher and Menou* (2013), it was applied to two hot Jupiters, which would be influenced by the active drag less than UHJs due to their colder temperatures. Hints of the magnetic circulation regime can be seen in their HD 209458b model, but the HD 189733b model was too cold for this regime to manifest.

The magnetic circulation regime first appeared when I applied our kinematic MHD to the UHJ WASP-76b (Chapter III). This regime is characterized by upper atmosphere dayside flow that moves up and over the poles. This is in contrast to models that do not take into account magnetic effects which show flow mostly eastward (due to the equatorial jet) or day to night flow. At some pressures in our active drag models, the nighstide still showed super-rotational flow that diverged on the dayside. In all cases, the equatorial jet was weakened, thus reducing or eliminating the hotspot offset. This combination of circulation changes were only present with our active drag

and could not be reproduced by uniform drag models.

At this point in time, this circulation regime is theoretical and has not been confirmed by observation. At the end of Chapter V, I describe a set of observations that could identify a planet operating in this regime. I briefly summarize them here:

- *Phase curves:* The active drag models showed that increasing our magnetic drag strength resulted in a decrease in hotspot offset and an increase in day-night temperature contrast.

- *High Resolution Emission Spectra:* The magnetic circulation regime influences the net Doppler shift as a function of phase, especially around secondary eclipse for high resolution emission spectra.

- *High Resolution Transmission Spectra:* For our active drag models, the net Doppler shift showed less overall blueshifting throughout transit and, depending on the wavelength, could become more redshifted during parts of transit.

If a planet was found to be exhibiting this behavior, it would be evidence that this planet's atmosphere is operating in the magnetic circulation regime. If conclusive, this would be the first (indirect or direct) detection of an exoplanet's magnetic field's effect on the planet's atmospheric circulation.[3] This claim would be highly scrutinized, and thus multiple independent pieces of evidence would be necessary to convince the exoplanet community at large.

An additional piece of evidence for planetary magnetic fields would be the discovery of a *latitudinally* shifted hotspot. Although not currently a feature reproduced from our kinematic MHD approach, time-varying and latitudinally shifted hotspots are predicted by non-ideal MHD models (*Hindle et al.*, 2021b). These features are potentially detectible via the eclipse mapping technique with *JWST* (*Rauscher et al.*, 2018).

[3]Recent work at radio frequencies may have detected evidence of stellar magnetic fields interacting with exoplanetary fields, see (*Turner et al.*, 2021).

Eclipse mapping with *JWST* is still in its infancy, but our models were included in the first ever eclipse mapping with *JWST*, from data of the UHJ WASP-18b (*Coulombe et al.*, 2023). It was found that the active drag 20 G model (without a hotspot offset) was a better fit to the calculated eclipse map than the 0 G model. Additionally, the 20 G model did a better job of fitting the longitudinally-averaged temperature gradient than the 0 G model. The data was additionally compared to another GCM which used Uniform drag, and the strong drag model was found to be their best fitting model. This eclipse map thus shows evidence for strong, circulation altering drag in this planet's atmosphere. I look forward to future work comparing more GCMs to the excellent data being taken by this telescope.

6.3 Future Work

As I prepare to leave graduate school, I am looking forward to continue my scientific exploration into the depths of magnetism. A variety of updates of varying complexity can be made to the active magnetic drag routine to allow investigations of different parameter spaces. One such addition is taking different metallicities into account when calculating the active drag timescale. More metals mean more potential ions, thus requiring stronger drag. In theory, a higher metallicity planet at a lower temperature might experience a similar level of drag as a lower metallicity planet at a higher temperature, but it is not immediately obvious how their resultant circulation patterns will look.

Another interesting avenue of investigation would be relaxing the aligned dipole assumption, potentially following the derivation presented in *Batygin and Stanley* (2014). This would be an extensive addition, as under the current approximation, only the east-west winds are dragged. Allowing the dipole to be tilted means that drag would need to be applied in the east-west and north-south direction at different strengths, in order to drag the perpendicular flow correctly. This addition may also

lead to latitudinally shifted hotspots, which provides another avenue for planetary magnetic field detection.

Speculating on the future of the field, it is already apparent that *JWST* data will shape our understanding of exoplanet atmospheres and formation for the next decade. As I finish this dissertation, many papers involving the first cycle of observations have been published, and Cycle 2 notifications have already been posted. Looking forward even further, ground based ELTs will certainly shape the field. As data quality increases and resolutions get even higher, 3D effects will only become more important.

BIBLIOGRAPHY

BIBLIOGRAPHY

Alonso-Floriano, F. J., et al. (2019), He the transmission spectrum of hd209458 b, *A&A*, *629*, A110, doi:10.1051/0004-6361/201935979.

Arcangeli, J., J.-M. Désert, V. Parmentier, K. B. Stevenson, J. L. Bean, M. R. Line, L. Kreidberg, J. J. Fortney, and A. P. Showman (2019), Climate of an ultra hot Jupiter. Spectroscopic phase curve of WASP-18b with HST/WFC3, *A&A*, *625*, A136, doi:10.1051/0004-6361/201834891.

Armstrong, D. J., E. de Mooij, J. Barstow, H. P. Osborn, J. Blake, and N. F. Saniee (2016), Variability in the atmosphere of the hot giant planet HAT-P-7 b, *Nature Astronomy*, *1*, 0004, doi:10.1038/s41550-016-0004.

Arras, P., and A. Socrates (2010), Thermal Tides in Fluid Extrasolar Planets, *ApJ*, *714*(1), 1–12, doi:10.1088/0004-637X/714/1/1.

Auclair-Desrotour, P., and J. Leconte (2018), Semidiurnal thermal tides in asynchronously rotating hot Jupiters, *A&A*, *613*, A45, doi:10.1051/0004-6361/201731683.

Baraffe, I., G. Chabrier, and T. Barman (2010), The physical properties of extra-solar planets, *Reports on Progress in Physics*, *73*(1), 016901, doi:10.1088/0034-4885/73/1/016901.

Barstow, J. K., S. Aigrain, P. G. J. Irwin, and D. K. Sing (2017), A Consistent Retrieval Analysis of 10 Hot Jupiters Observed in Transmission, *ApJ*, *834*(1), 50, doi:10.3847/1538-4357/834/1/50.

Batygin, K., and S. Stanley (2014), Non-axisymmetric Flows on Hot Jupiters with Oblique Magnetic Fields, *ApJ*, *794*(1), 10, doi:10.1088/0004-637X/794/1/10.

Batygin, K., and D. J. Stevenson (2010), Inflating Hot Jupiters with Ohmic Dissipation, *ApJ*, *714*(2), L238–L243, doi:10.1088/2041-8205/714/2/L238.

Batygin, K., D. J. Stevenson, and P. H. Bodenheimer (2011), Evolution of Ohmically Heated Hot Jupiters, *ApJ*, *738*(1), 1, doi:10.1088/0004-637X/738/1/1.

Batygin, K., S. Stanley, and D. J. Stevenson (2013), Magnetically Controlled Circulation on Hot Extrasolar Planets, *ApJ*, *776*(1), 53, doi:10.1088/0004-637X/776/1/53.

Baxter, C., J.-M. Désert, V. Parmentier, M. Line, J. Fortney, J. Arcangeli, J. L. Bean, K. O. Todorov, and M. Mansfield (2020), A transition between the hot and the ultra-hot Jupiter atmospheres, *A&A*, *639*, A36, doi:10.1051/0004-6361/201937394.

Bell, T. J., and N. B. Cowan (2018), Increased heat transport in ultra-hot jupiter atmospheres through h2 dissociation and recombination, *The Astrophysical Journal*, *857*(2), L20, doi:10.3847/2041-8213/aabcc8.

Beltz, H., E. Rauscher, M. Brogi, and E. M. R. Kempton (2021), A Significant Increase in Detection of High-resolution Emission Spectra Using a Three-dimensional Atmospheric Model of a Hot Jupiter, *AJ*, *161*(1), 1, doi:10.3847/1538-3881/abb67b.

Beltz, H., E. Rauscher, E. M. R. Kempton, I. Malsky, G. Ochs, M. Arora, and A. Savel (2022a), Magnetic Drag and 3D Effects in Theoretical High-resolution Emission Spectra of Ultrahot Jupiters: the Case of WASP-76b, *AJ*, *164*(4), 140, doi:10.3847/1538-3881/ac897b.

Beltz, H., E. Rauscher, M. T. Roman, and A. Guilliat (2022b), Exploring the Effects of Active Magnetic Drag in a General Circulation Model of the Ultrahot Jupiter WASP-76b, *AJ*, *163*(1), 35, doi:10.3847/1538-3881/ac3746.

Ben-Jaffel, L., et al. (2021), Signatures of strong magnetization and a metal-poor atmosphere for a Neptune-sized exoplanet, *Nature Astronomy*, doi:10.1038/s41550-021-01505-x.

Birkby, J. L. (2018), Exoplanet Atmospheres at High Spectral Resolution, *arXiv e-prints*, arXiv:1806.04617.

Blecic, J., I. Dobbs-Dixon, and T. Greene (2017), The Implications of 3D Thermal Structure on 1D Atmospheric Retrieval, *ApJ*, *848*(2), 127, doi:10.3847/1538-4357/aa8171.

Brogi, M., and J. Birkby (2021), High-resolution Spectroscopy, in *ExoFrontiers; Big Questions in Exoplanetary Science*, edited by N. Madhusudhan, pp. 8–1, doi:10.1088/2514-3433/abfa8fch8.

Brogi, M., and M. R. Line (2019), Retrieving Temperatures and Abundances of Exoplanet Atmospheres with High-resolution Cross-correlation Spectroscopy, *AJ*, *157*(3), 114, doi:10.3847/1538-3881/aaffd3.

Brogi, M., I. A. G. Snellen, R. J. de Kok, S. Albrecht, J. Birkby, and E. J. W. de Mooij (2012), The signature of orbital motion from the dayside of the planet τ Boötis b, *Nature*, *486*(7404), 502–504, doi:10.1038/nature11161.

Brogi, M., R. J. de Kok, J. L. Birkby, H. Schwarz, and I. A. G. Snellen (2014), Carbon monoxide and water vapor in the atmosphere of the non-transiting exoplanet HD 179949 b, *A&A*, *565*, A124, doi:10.1051/0004-6361/201423537.

Brogi, M., R. J. de Kok, S. Albrecht, I. A. G. Snellen, J. L. Birkby, and H. Schwarz (2016), Rotation and Winds of Exoplanet HD 189733 b Measured with High-dispersion Transmission Spectroscopy, *ApJ*, *817*(2), 106, doi:10.3847/0004-637X/817/2/106.

Brogi, M., M. Line, J. Bean, J. M. Désert, and H. Schwarz (2017), A Framework to Combine Low- and High-resolution Spectroscopy for the Atmospheres of Transiting Exoplanets, *ApJ*, *839*(1), L2, doi:10.3847/2041-8213/aa6933.

Bryan, M. L., et al. (2020), Obliquity Constraints on an Extrasolar Planetary-mass Companion, *AJ*, *159*(4), 181, doi:10.3847/1538-3881/ab76c6.

Burrows, A., E. Rauscher, D. S. Spiegel, and K. Menou (2010), Photometric and Spectral Signatures of Three-dimensional Models of Transiting Giant Exoplanets, *ApJ*, *719*(1), 341–350, doi:10.1088/0004-637X/719/1/341.

Caldas, A., J. Leconte, F. Selsis, I. P. Waldmann, P. Bordé, M. Rocchetto, and B. Charnay (2019a), Effects of a fully 3D atmospheric structure on exoplanet transmission spectra: retrieval biases due to day-night temperature gradients, *A&A*, *623*, A161, doi:10.1051/0004-6361/201834384.

Caldas, A., J. Leconte, F. Selsis, I. P. Waldmann, P. Bordé, M. Rocchetto, and B. Charnay (2019b), Effects of a fully 3D atmospheric structure on exoplanet transmission spectra: retrieval biases due to day-night temperature gradients, *A&A*, *623*, A161, doi:10.1051/0004-6361/201834384.

Carone, L., R. Baeyens, P. Mollière, P. Barth, A. Vazan, L. Decin, P. Sarkis, O. Venot, and T. Henning (2019), Equatorial anti-rotating day side wind flow in WASP-43b elicited by deep wind jets?, *arXiv e-prints*, arXiv:1904.13334.

Carone, L., R. Baeyens, P. Mollière, P. Barth, A. Vazan, L. Decin, P. Sarkis, O. Venot, and T. Henning (2020), Equatorial retrograde flow in WASP-43b elicited by deep wind jets?, *MNRAS*, *496*(3), 3582–3614, doi:10.1093/mnras/staa1733.

Casasayas-Barris, N., et al. (2021), CARMENES detection of the Ca II infrared triplet and possible evidence of He I in the atmosphere of WASP-76b, *A&A*, *654*, A163, doi:10.1051/0004-6361/202141669.

Cauley, P. W., E. L. Shkolnik, J. Llama, and A. F. Lanza (2019), Magnetic field strengths of hot Jupiters from signals of star-planet interactions, *Nature Astronomy*, *3*, 1128–1134, doi:10.1038/s41550-019-0840-x.

Christensen, U. R., V. Holzwarth, and A. Reiners (2009), Energy flux determines magnetic field strength of planets and stars, *Nature*, *457*(7226), 167–169, doi:10.1038/nature07626.

Cont, D., et al. (2021), Detection of Fe and evidence for TiO in the dayside emission spectrum of WASP-33b, *A&A*, *651*, A33, doi:10.1051/0004-6361/202140732.

Coulombe, L.-P., et al. (2023), A broadband thermal emission spectrum of the ultra-hot Jupiter WASP-18b, *arXiv e-prints*, arXiv:2301.08192, doi:10.48550/arXiv.2301.08192.

Cridland, A. J., E. F. van Dishoeck, M. Alessi, and R. E. Pudritz (2019), Connecting planet formation and astrochemistry. A main sequence for C/O in hot exoplanetary atmospheres, *A&A*, *632*, A63, doi:10.1051/0004-6361/201936105.

de Kok, R. J., M. Brogi, I. A. G. Snellen, J. Birkby, S. Albrecht, and E. J. W. de Mooij (2013), Detection of carbon monoxide in the high-resolution day-side spectrum of the exoplanet HD 189733b, *A&A*, *554*, A82, doi:10.1051/0004-6361/201321381.

Deibert, E. K., et al. (2021), Detection of Ionized Calcium in the Atmosphere of the Ultra-hot Jupiter WASP-76b, *ApJ*, *919*(2), L15, doi:10.3847/2041-8213/ac2513.

Deitrick, R., J. M. Mendonça, U. Schroffenegger, S. L. Grimm, S.-M. Tsai, and K. Heng (2020), THOR 2.0: Major improvements to the open-source general circulation model, *The Astrophysical Journal Supplement Series*, *248*(2), 30, doi:10.3847/1538-4365/ab930e.

Deitrick, R., J. M. Mendonça, U. Schroffenegger, S. L. Grimm, S.-M. Tsai, and K. Heng (2020), THOR 2.0: Major Improvements to the Open-source General Circulation Model, *ApJS*, *248*(2), 30, doi:10.3847/1538-4365/ab930e.

Dobbs-Dixon, I., and E. Agol (2013), Three-dimensional radiative-hydrodynamical simulations of the highly irradiated short-period exoplanet HD 189733b, *MNRAS*, *435*(4), 3159–3168, doi:10.1093/mnras/stt1509.

Drummond, B., et al. (2020), Implications of three-dimensional chemical transport in hot Jupiter atmospheres: Results from a consistently coupled chemistry-radiation-hydrodynamics model, *A&A*, *636*, A68, doi:10.1051/0004-6361/201937153.

Edwards, B., et al. (2020), ARES i: WASP-76 b, a tale of two HST spectra, *The Astronomical Journal*, *160*(1), 8, doi:10.3847/1538-3881/ab9225.

Ehrenreich, D., et al. (2020), Nightside condensation of iron in an ultrahot giant exoplanet, *Nature*, *580*(7805), 597–601, doi:10.1038/s41586-020-2107-1.

Feng, Y. K., M. R. Line, J. J. Fortney, K. B. Stevenson, J. Bean, L. Kreidberg, and V. Parmentier (2016), The Impact of Non-uniform Thermal Structure on the Interpretation of Exoplanet Emission Spectra, *ApJ*, *829*(1), 52, doi:10.3847/0004-637X/829/1/52.

Flowers, E., M. Brogi, E. Rauscher, E. M. R. Kempton, and A. Chiavassa (2019), The High-resolution Transmission Spectrum of HD 189733b Interpreted with Atmospheric Doppler Shifts from Three-dimensional General Circulation Models, *AJ*, *157*(5), 209, doi:10.3847/1538-3881/ab164c.

Follert, R., et al. (2014), CRIRES+: a cross-dispersed high-resolution infrared spectrograph for the ESO VLT, in *Ground-based and Airborne Instrumentation for Astronomy V*, *Society of Photo-Optical Instrumentation Engineers (SPIE) Conference Series*, vol. 9147, edited by S. K. Ramsay, I. S. McLean, and H. Takami, p. 914719, doi:10.1117/12.2054197.

Forget, F., F. Hourdin, R. Fournier, C. Hourdin, O. Talagrand, M. Collins, S. R. Lewis, P. L. Read, and J.-P. Huot (1999), Improved general circulation models of the Martian atmosphere from the surface to above 80 km, *J. Geophys. Res.*, *104*(E10), 24,155–24,176, doi:10.1029/1999JE001025.

Fortney, J. J., C. S. Cooper, A. P. Showman, M. S. Marley, and R. S. Freedman (2006), The Influence of Atmospheric Dynamics on the Infrared Spectra and Light Curves of Hot Jupiters, *ApJ*, *652*(1), 746–757, doi:10.1086/508442.

Fortney, J. J., K. Lodders, M. S. Marley, and R. S. Freedman (2008), A Unified Theory for the Atmospheres of the Hot and Very Hot Jupiters: Two Classes of Irradiated Atmospheres, *ApJ*, *678*(2), 1419–1435, doi:10.1086/528370.

Fortney, J. J., M. Shabram, A. P. Showman, Y. Lian, R. S. Freedman, M. S. Marley, and N. K. Lewis (2010), Transmission Spectra of Three-Dimensional Hot Jupiter Model Atmospheres, *ApJ*, *709*(2), 1396–1406, doi:10.1088/0004-637X/709/2/1396.

Fortney, J. J., R. I. Dawson, and T. D. Komacek (2021), Hot Jupiters: Origins, Structure, Atmospheres, *Journal of Geophysical Research (Planets)*, *126*(3), e06629, doi:10.1029/2020JE006629.

Fossati, L., M. E. Young, D. Shulyak, T. Koskinen, C. Huang, P. E. Cubillos, K. France, and A. G. Sreejith (2021), Non-local thermodynamic equilibrium effects determine the upper atmospheric temperature structure of the ultra-hot Jupiter KELT-9b, *A&A*, *653*, A52, doi:10.1051/0004-6361/202140813.

Fu, G., et al. (2020), The Hubble PanCET program: Transit and Eclipse Spectroscopy of the Strongly Irradiated Giant Exoplanet WASP-76b, *arXiv e-prints*, arXiv:2005.02568.

Fu, G., et al. (2021), The Hubble PanCET Program: Transit and Eclipse Spectroscopy of the Strongly Irradiated Giant Exoplanet WASP-76b, *AJ*, *162*(3), 108, doi:10.3847/1538-3881/ac1200.

Gan, T., et al. (2023), Occurrence Rate of Hot Jupiters Around Early-type M Dwarfs Based on Transiting Exoplanet Survey Satellite Data, *AJ*, *165*(1), 17, doi:10.3847/1538-3881/ac9b12.

Gandhi, S., and N. Madhusudhan (2018), Retrieval of exoplanet emission spectra with HyDRA, *MNRAS*, *474*(1), 271–288, doi:10.1093/mnras/stx2748.

Gandhi, S., and N. Madhusudhan (2019), New avenues for thermal inversions in atmospheres of hot Jupiters, *MNRAS*, *485*(4), 5817–5830, doi:10.1093/mnras/stz751.

Gandhi, S., N. Madhusudhan, G. Hawker, and A. Piette (2019), HyDRA-H: Simultaneous Hybrid Retrieval of Exoplanetary Emission Spectra, *AJ*, *158*(6), 228, doi:10.3847/1538-3881/ab4efc.

Gandhi, S., A. Kesseli, I. Snellen, M. Brogi, J. P. Wardenier, V. Parmentier, L. Welbanks, and A. B. Savel (2022), Spatially resolving the terminator: variation of Fe, temperature, and winds in WASP-76 b across planetary limbs and orbital phase, *MNRAS*, *515*(1), 749–766, doi:10.1093/mnras/stac1744.

Giacobbe, P., et al. (2021), Five carbon- and nitrogen-bearing species in a hot giant planet's atmosphere, *Nature*, *592*(7853), 205–208, doi:10.1038/s41586-021-03381-x.

Gibson, N. P., et al. (2020), Detection of Fe I in the atmosphere of the ultra-hot Jupiter WASP-121b, and a new likelihood-based approach for Doppler-resolved spectroscopy, *MNRAS*, *493*(2), 2215–2228, doi:10.1093/mnras/staa228.

Ginzburg, S., and R. Sari (2015), Hot-Jupiter Inflation due to Deep Energy Deposition, *ApJ*, *803*(2), 111, doi:10.1088/0004-637X/803/2/111.

Gu, P.-G., and G. I. Ogilvie (2009), Diurnal thermal tides in a non-synchronized hot Jupiter, *MNRAS*, *395*(1), 422–435, doi:10.1111/j.1365-2966.2009.14531.x.

Guillot, T. (2010), On the radiative equilibrium of irradiated planetary atmospheres, *A&A*, *520*, A27, doi:10.1051/0004-6361/200913396.

Guilluy, G., A. Sozzetti, M. Brogi, A. S. Bonomo, P. Giacobbe, R. Claudi, and S. Benatti (2019), Exoplanet atmospheres with GIANO. II. Detection of molecular absorption in the dayside spectrum of HD 102195b, *A&A*, *625*, A107, doi:10.1051/0004-6361/201834615.

Guo, X., J. A. Johnson, A. W. Mann, A. L. Kraus, J. L. Curtis, and D. W. Latham (2017), The Metallicity Distribution and Hot Jupiter Rate of the Kepler Field: Hectochelle High-resolution Spectroscopy for 776 Kepler Target Stars, *ApJ*, *838*(1), 25, doi:10.3847/1538-4357/aa6004.

Harada, C. K., E. M. R. Kempton, E. Rauscher, M. Roman, and M. Brinjikji (2019), Signatures of Clouds in Hot Jupiter Atmospheres: Modeled High Resolution Emission Spectra from 3D General Circulation Models, *arXiv e-prints*, arXiv:1912.02268.

Harada, C. K., E. M. R. Kempton, E. Rauscher, M. Roman, I. Malsky, M. Brinjikji, and V. DiTomasso (2021), Signatures of Clouds in Hot Jupiter Atmospheres: Modeled High-resolution Emission Spectra from 3D General Circulation Models, *ApJ*, *909*(1), 85, doi:10.3847/1538-4357/abdc22.

Helling, C., P. Gourbin, P. Woitke, and V. Parmentier (2019a), Sparkling nights and very hot days on WASP-18b: the formation of clouds and the emergence of an ionosphere, *A&A*, *626*, A133, doi:10.1051/0004-6361/201834085.

Helling, C., Y. Kawashima, V. Graham, D. Samra, K. L. Chubb, M. Min, L. B. F. M. Waters, and V. Parmentier (2020), Mineral cloud and hydrocarbon haze particles in the atmosphere of the hot Jupiter JWST target WASP-43b, *A&A*, *641*, A178, doi:10.1051/0004-6361/202037633.

Helling, C., et al. (2019b), Understanding the atmospheric properties and chemical composition of the ultra-hot Jupiter HAT-P-7b. I. Cloud and chemistry mapping, *A&A*, *631*, A79, doi:10.1051/0004-6361/201935771.

Helling, C., et al. (2021), Cloud property trends in hot and ultra-hot giant gas planets (WASP-43b, WASP-103b, WASP-121b, HAT-P-7b, and WASP-18b), *A&A*, *649*, A44, doi:10.1051/0004-6361/202039911.

Heng, K., and A. P. Showman (2015), Atmospheric Dynamics of Hot Exoplanets, *Annual Review of Earth and Planetary Sciences*, *43*, 509–540, doi:10.1146/annurev-earth-060614-105146.

Heng, K., K. Menou, and P. J. Phillipps (2011), Atmospheric circulation of tidally locked exoplanets: a suite of benchmark tests for dynamical solvers, *MNRAS*, *413*(4), 2380–2402, doi:10.1111/j.1365-2966.2011.18315.x.

Herman, M. K., E. J. W. de Mooij, S. K. Nugroho, N. P. Gibson, and R. Jayawardhana (2022), Dayside Fe I Emission, Day-Night Brightness Contrast and Phase Offset of the Exoplanet WASP-33b, *AJ*, *163*(6), 248, doi:10.3847/1538-3881/ac5f4d.

Hindle, A. W., P. J. Bushby, and T. M. Rogers (2019), Shallow-water Magnetohydrodynamics for Westward Hotspots on Hot Jupiters, *ApJ*, *872*(2), L27, doi:10.3847/2041-8213/ab05dd.

Hindle, A. W., P. J. Bushby, and T. M. Rogers (2021a), Observational Consequences of Shallow-water Magnetohydrodynamics on Hot Jupiters, *ApJ*, *916*(1), L8, doi:10.3847/2041-8213/ac0fec.

Hindle, A. W., P. J. Bushby, and T. M. Rogers (2021b), The Magnetic Mechanism for Hotspot Reversals in Hot Jupiter Atmospheres, *arXiv e-prints*, arXiv:2107.07515.

Huang, X., and A. Cumming (2012), Ohmic Dissipation in the Interiors of Hot Jupiters, *ApJ*, *757*(1), 47, doi:10.1088/0004-637X/757/1/47.

Hubeny, I., A. Burrows, and D. Sudarsky (2003), A Possible Bifurcation in Atmospheres of Strongly Irradiated Stars and Planets, *ApJ*, *594*(2), 1011–1018, doi:10.1086/377080.

Ikeda, Y., et al. (2016), High sensitivity, wide coverage, and high-resolution NIR non-cryogenic spectrograph, WINERED, in *Ground-based and Airborne Instrumentation for Astronomy VI*, *Society of Photo-Optical Instrumentation Engineers (SPIE) Conference Series*, vol. 9908, edited by C. J. Evans, L. Simard, and H. Takami, p. 99085Z, doi:10.1117/12.2230886.

Kaeufl, H.-U., et al. (2004), CRIRES: a high-resolution infrared spectrograph for ESO's VLT, in *Ground-based Instrumentation for Astronomy*, *Society of Photo-Optical Instrumentation Engineers (SPIE) Conference Series*, vol. 5492, edited by A. F. M. Moorwood and M. Iye, pp. 1218–1227, doi:10.1117/12.551480.

Kasper, D., J. L. Bean, M. R. Line, A. Seifahrt, J. Stürmer, L. Pino, J.-M. Désert, and M. Brogi (2021), Confirmation of Iron Emission Lines and Nondetection of TiO on the Dayside of KELT-9b with MAROON-X, *ApJ*, *921*(1), L18, doi:10.3847/2041-8213/ac30e1.

Kataria, T., D. K. Sing, N. K. Lewis, C. Visscher, A. P. Showman, J. J. Fortney, and M. S. Marley (2016), The Atmospheric Circulation of a Nine-hot-Jupiter Sample: Probing Circulation and Chemistry over a Wide Phase Space, *ApJ*, *821*(1), 9, doi:10.3847/0004-637X/821/1/9.

Kawauchi, K., N. Narita, B. Sato, and Y. Kawashima (2021), Investigation of the upper atmosphere in ultra-hot Jupiter WASP-76 b with high-resolution spectroscopy, *arXiv e-prints*, arXiv:2112.02546.

Kempton, E. M. R., R. Perna, and K. Heng (2014), High Resolution Transmission Spectroscopy as a Diagnostic for Jovian Exoplanet Atmospheres: Constraints from Theoretical Models, *ApJ*, *795*(1), 24, doi:10.1088/0004-637X/795/1/24.

Kesseli, A. Y., and I. A. G. Snellen (2021a), Confirmation of Asymmetric Iron Absorption in WASP-76b with HARPS, *ApJ*, *908*(1), L17, doi:10.3847/2041-8213/abe047.

Kesseli, A. Y., and I. A. G. Snellen (2021b), Confirmation of Asymmetric Iron Absorption in WASP-76b with HARPS, *ApJ*, *908*(1), L17, doi:10.3847/2041-8213/abe047.

Kesseli, A. Y., I. A. G. Snellen, N. Casasayas-Barris, P. Mollière, and A. Sánchez-López (2022), An Atomic Spectral Survey of WASP-76b: Resolving Chemical Gradients and Asymmetries, *AJ*, *163*(3), 107, doi:10.3847/1538-3881/ac4336.

Knutson, H. A., et al. (2012), 3.6 and 4.5 μm Phase Curves and Evidence for Non-equilibrium Chemistry in the Atmosphere of Extrasolar Planet HD 189733b, *ApJ*, *754*(1), 22, doi:10.1088/0004-637X/754/1/22.

Koll, D. D. B., and T. D. Komacek (2018), Atmospheric Circulations of Hot Jupiters as Planetary Heat Engines, *ApJ*, *853*(2), 133, doi:10.3847/1538-4357/aaa3de.

Komacek, T. D., and A. P. Showman (2016), Atmospheric Circulation of Hot Jupiters: Dayside-Nightside Temperature Differences, *ApJ*, *821*(1), 16, doi:10.3847/0004-637X/821/1/16.

Komacek, T. D., and A. N. Youdin (2017), Structure and Evolution of Internally Heated Hot Jupiters, *ApJ*, *844*(2), 94, doi:10.3847/1538-4357/aa7b75.

Komacek, T. D., A. P. Showman, and X. Tan (2017), Atmospheric Circulation of Hot Jupiters: Dayside-Nightside Temperature Differences. II. Comparison with Observations, *ApJ*, *835*(2), 198, doi:10.3847/1538-4357/835/2/198.

Komacek, T. D., A. P. Showman, and V. Parmentier (2019), Vertical Tracer Mixing in Hot Jupiter Atmospheres, *ApJ*, *881*(2), 152, doi:10.3847/1538-4357/ab338b.

Kreidberg, L., et al. (2014), A Precise Water Abundance Measurement for the Hot Jupiter WASP-43b, *ApJ*, *793*(2), L27, doi:10.1088/2041-8205/793/2/L27.

Kreidberg, L., et al. (2018), Global Climate and Atmospheric Composition of the Ultra-hot Jupiter WASP-103b from HST and Spitzer Phase Curve Observations, *AJ*, *156*(1), 17, doi:10.3847/1538-3881/aac3df.

Kurucz, R. (1995), Kurucz cd-rom no. 23, *Atomic Line List*.

Lally, M., and A. Vanderburg (2022), Reassessing the Evidence for Time Variability in the Atmosphere of the Exoplanet HAT-P-7 b_f, *AJ*, *163*(4), 181, doi:10.3847/1538-3881/ac53a8.

Landman, R., A. Sánchez-López, P. Mollière, A. Y. Kesseli, A. J. Louca, and I. A. G. Snellen (2021), Detection of OH in the ultra-hot Jupiter WASP-76b, *A&A*, *656*, A119, doi:10.1051/0004-6361/202141696.

Laughlin, G., M. Crismani, and F. C. Adams (2011), On the Anomalous Radii of the Transiting Extrasolar Planets, *ApJ*, *729*(1), L7, doi:10.1088/2041-8205/729/1/L7.

Lee, E. K. H., B. Prinoth, D. Kitzmann, S.-M. Tsai, J. Hoeijmakers, N. W. Borsato, and K. Heng (2022), The Mantis Network II: examining the 3D high-resolution observable properties of the UHJs WASP-121b and WASP-189b through GCM modelling, *MNRAS*, *517*(1), 240–256, doi:10.1093/mnras/stac2246.

Lee, E. K. H., et al. (2021), 3D radiative-transfer for exoplanet atmospheres. gCM-CRT: a GPU accelerated MCRT code, *arXiv e-prints*, arXiv:2110.15640.

Lee, U. (2020), Tidal oscillations of rotating hot Jupiters, *MNRAS*, *494*(3), 3141–3155, doi:10.1093/mnras/staa986.

Li, J., and J. Goodman (2010), Circulation and Dissipation on Hot Jupiters, *ApJ*, *725*(1), 1146–1158, doi:10.1088/0004-637X/725/1/1146.

Line, M. R., K. B. Stevenson, J. Bean, J.-M. Desert, J. J. Fortney, L. Kreidberg, N. Madhusudhan, A. P. Showman, and H. Diamond-Lowe (2016), No Thermal Inversion and a Solar Water Abundance for the Hot Jupiter HD 209458b from HST/WFC3 Spectroscopy, *AJ*, *152*(6), 203, doi:10.3847/0004-6256/152/6/203.

Line, M. R., et al. (2021), A solar C/O and sub-solar metallicity in a hot Jupiter atmosphere, *Nature*, *598*(7882), 580–584, doi:10.1038/s41586-021-03912-6.

Lodders, K. (2003), Solar System Abundances and Condensation Temperatures of the Elements, *ApJ*, *591*(2), 1220–1247, doi:10.1086/375492.

Lopez, E. D., and J. J. Fortney (2016), Re-inflated Warm Jupiters around Red Giants, *ApJ*, *818*(1), 4, doi:10.3847/0004-637X/818/1/4.

Lothringer, J. D., T. Barman, and T. Koskinen (2018), Extremely Irradiated Hot Jupiters: Non-oxide Inversions, H^- Opacity, and Thermal Dissociation of Molecules, *ApJ*, *866*(1), 27, doi:10.3847/1538-4357/aadd9e.

Lothringer, J. D., D. K. Sing, Z. Rustamkulov, H. R. Wakeford, K. B. Stevenson, N. Nikolov, P. Lavvas, J. J. Spake, and A. T. Winch (2022), UV Absorption by Silicate Cloud Precursors in Ultra-hot Jupiter WASP-178b, *arXiv e-prints*, arXiv:2204.03639.

Louden, T., and P. J. Wheatley (2015), Spatially Resolved Eastward Winds and Rotation of HD 189733b, *ApJ*, *814*(2), L24, doi:10.1088/2041-8205/814/2/L24.

MacDonald, R. J., and N. K. Lewis (2021), TRIDENT: A Rapid 3D Radiative Transfer Model for Exoplanet Transmission Spectra, *arXiv e-prints*, arXiv:2111.05862.

Mace, G., et al. (2016), 300 nights of science with IGRINS at McDonald Observatory, in *Ground-based and Airborne Instrumentation for Astronomy VI*, *Society of Photo-Optical Instrumentation Engineers (SPIE) Conference Series*, vol. 9908, edited by C. J. Evans, L. Simard, and H. Takami, p. 99080C, doi:10.1117/12.2232780.

Madhusudhan, N. (2012), C/O Ratio as a Dimension for Characterizing Exoplanetary Atmospheres, *ApJ*, *758*(1), 36, doi:10.1088/0004-637X/758/1/36.

Malsky, I., E. Rauscher, E. M. R. Kempton, M. Roman, D. Long, and C. K. Harada (2021), Modeling the High-resolution Emission Spectra of Clear and Cloudy Non-transiting Hot Jupiters, *ApJ*, *923*(1), 62, doi:10.3847/1538-4357/ac2a2a.

Mansfield, M., et al. (2018), An HST/WFC3 thermal emission spectrum of the hot jupiter HAT-p-7b, *The Astronomical Journal*, *156*(1), 10, doi:10.3847/1538-3881/aac497.

Mansfield, M., et al. (2021), A unique hot Jupiter spectral sequence with evidence for compositional diversity, *Nature Astronomy*, *5*, 1224–1232, doi:10.1038/s41550-021-01455-4.

May, E. M., et al. (2021), Spitzer Phase-curve Observations and Circulation Models of the Inflated Ultrahot Jupiter WASP-76b, *AJ*, *162*(4), 158, doi:10.3847/1538-3881/ac0e30.

May, E. M., et al. (2022), A New Analysis of Eight Spitzer Phase Curves and Hot Jupiter Population Trends: Qatar-1b, Qatar-2b, WASP-52b, WASP-34b, and WASP-140b, *AJ*, *163*(6), 256, doi:10.3847/1538-3881/ac6261.

Mayne, N. J., I. Baraffe, D. M. Acreman, C. Smith, N. Wood, D. S. Amundsen, J. Thuburn, and D. R. Jackson (2014), Using the um dynamical cores to reproduce idealised 3-d flows, *Geoscientific Model Development*, *7*(6), 3059–3087, doi:10.5194/gmd-7-3059-2014.

Mendonça, J. M., S.-m. Tsai, M. Malik, S. L. Grimm, and K. Heng (2018), Three-dimensional Circulation Driving Chemical Disequilibrium in WASP-43b, *ApJ*, *869*(2), 107, doi:10.3847/1538-4357/aaed23.

Menou, K. (2012), MAGNETIC SCALING LAWS FOR THE ATMOSPHERES OF HOT GIANT EXOPLANETS, *The Astrophysical Journal*, *745*(2), 138, doi:10.1088/0004-637x/745/2/138.

Miller-Ricci Kempton, E., and E. Rauscher (2012), Constraining High-speed Winds in Exoplanet Atmospheres through Observations of Anomalous Doppler Shifts during Transit, *ApJ*, *751*(2), 117, doi:10.1088/0004-637X/751/2/117.

Mollière, P., R. van Boekel, C. Dullemond, T. Henning, and C. Mordasini (2015), Model Atmospheres of Irradiated Exoplanets: The Influence of Stellar Parameters, Metallicity, and the C/O Ratio, *ApJ*, *813*(1), 47, doi:10.1088/0004-637X/813/1/47.

Nugroho, S. K., H. Kawahara, K. Masuda, T. Hirano, T. Kotani, and A. Tajitsu (2017), High-resolution Spectroscopic Detection of TiO and a Stratosphere in the Day-side of WASP-33b, *AJ*, *154*(6), 221, doi:10.3847/1538-3881/aa9433.

Nugroho, S. K., N. P. Gibson, E. J. W. de Mooij, M. K. Herman, C. A. Watson, H. Kawahara, and S. R. Merritt (2020), Detection of Fe I Emission in the Dayside Spectrum of WASP-33b, *ApJ*, *898*(2), L31, doi:10.3847/2041-8213/aba4b6.

Nugroho, S. K., et al. (2021), First Detection of Hydroxyl Radical Emission from an Exoplanet Atmosphere: High-dispersion Characterization of WASP-33b Using Subaru/IRD, *ApJ*, *910*(1), L9, doi:10.3847/2041-8213/abec71.

Owen, J. E., and F. C. Adams (2014), Magnetically controlled mass-loss from extrasolar planets in close orbits, *MNRAS*, *444*(4), 3761–3779, doi:10.1093/mnras/stu1684.

Park, C., et al. (2014a), Design and early performance of IGRINS (Immersion Grating Infrared Spectrometer), in *Ground-based and Airborne Instrumentation for Astronomy V*, *Society of Photo-Optical Instrumentation Engineers (SPIE) Conference Series*, vol. 9147, edited by S. K. Ramsay, I. S. McLean, and H. Takami, p. 91471D, doi:10.1117/12.2056431.

Park, C., et al. (2014b), Design and early performance of IGRINS (Immersion Grating Infrared Spectrometer), in *Ground-based and Airborne Instrumentation for Astronomy V*, *Society of Photo-Optical Instrumentation Engineers (SPIE) Conference Series*, vol. 9147, edited by S. K. Ramsay, I. S. McLean, and H. Takami, p. 91471D, doi:10.1117/12.2056431.

Parmentier, V., and I. J. M. Crossfield (2018), Exoplanet Phase Curves: Observations and Theory, in *Handbook of Exoplanets*, edited by H. J. Deeg and J. A. Belmonte, p. 116, doi:10.1007/978-3-319-55333-7$_1$16.

Parmentier, V., et al. (2018), From thermal dissociation to condensation in the atmospheres of ultra hot Jupiters: WASP-121b in context, *A&A*, *617*, A110, doi:10.1051/0004-6361/201833059.

Pelletier, S., et al. (2021), Where Is the Water? Jupiter-like C/H Ratio but Strong H_2O Depletion Found on τ Boötis b Using SPIRou, *AJ*, *162*(2), 73, doi:10.3847/1538-3881/ac0428.

Penn, J., and G. K. Vallis (2017), The Thermal Phase Curve Offset on Tidally and Nontidally Locked Exoplanets: A Shallow Water Model, *ApJ*, *842*(2), 101, doi:10.3847/1538-4357/aa756e.

Perez-Becker, D., and A. P. Showman (2013), Atmospheric Heat Redistribution on Hot Jupiters, *ApJ*, *776*(2), 134, doi:10.1088/0004-637X/776/2/134.

Perna, R., K. Menou, and E. Rauscher (2010a), 20020530Magnetic Drag on Hot Jupiter Atmospheric Winds, *ApJ*, *719*(2), 1421–1426, doi:10.1088/0004-637X/719/2/1421.

Perna, R., K. Menou, and E. Rauscher (2010b), 20020603Ohmic Dissipation in the Atmospheres of Hot Jupiters, *ApJ*, *724*(1), 313–317, doi:10.1088/0004-637X/724/1/313.

Pinhas, A., N. Madhusudhan, S. Gandhi, and R. MacDonald (2019), H_2O abundances and cloud properties in ten hot giant exoplanets, *MNRAS*, *482*(2), 1485–1498, doi:10.1093/mnras/sty2544.

Pino, L., et al. (2022), The GAPS Programme at TNG. XLI. The climate of KELT-9b revealed with a new approach to high spectral resolution phase curves, *arXiv e-prints*, arXiv:2209.11735.

Piskorz, D., et al. (2016), Evidence for the Direct Detection of the Thermal Spectrum of the Non-Transiting Hot Gas Giant HD 88133 b, *ApJ*, *832*(2), 131, doi:10.3847/0004-637X/832/2/131.

Pluriel, W., T. Zingales, J. Leconte, and V. Parmentier (2020), Strong biases in retrieved atmospheric composition caused by day-night chemical heterogeneities, *A&A*, *636*, A66, doi:10.1051/0004-6361/202037678.

Polyansky, O. L., A. A. Kyuberis, N. F. Zobov, J. Tennyson, S. N. Yurchenko, and L. Lodi (2018), Exomol molecular line lists xxx: a complete high-accuracy line list for water, *Monthly Notices of the Royal Astronomical Society*, *480*(2), 2597–2608.

Prinoth, B., et al. (2021), Titanium oxide and chemical inhomogeneity in the atmosphere of the exoplanet WASP-189b, *arXiv e-prints*, arXiv:2111.12732.

Quirrenbach, A., et al. (2014), CARMENES instrument overview, in *Ground-based and Airborne Instrumentation for Astronomy V*, *Society of Photo-Optical Instrumentation Engineers (SPIE) Conference Series*, vol. 9147, edited by S. K. Ramsay, I. S. McLean, and H. Takami, p. 91471F, doi:10.1117/12.2056453.

Rasio, F. A., C. A. Tout, S. H. Lubow, and M. Livio (1996), Tidal Decay of Close Planetary Orbits, *ApJ*, *470*, 1187, doi:10.1086/177941.

Rauscher, E., and E. M. R. Kempton (2014), THE ATMOSPHERIC CIRCULATION AND OBSERVABLE PROPERTIES OF NON-SYNCHRONOUSLY ROTATING HOT JUPITERS, *The Astrophysical Journal*, *790*(1), 79, doi:10.1088/0004-637x/790/1/79.

Rauscher, E., and K. Menou (2010), Three-dimensional Modeling of Hot Jupiter Atmospheric Flows, *ApJ*, *714*(2), 1334–1342, doi:10.1088/0004-637X/714/2/1334.

Rauscher, E., and K. Menou (2012), A general circulation model for gaseous exoplanets with double-gray radiative transfer, *The Astrophysical Journal*, *750*(2), 96.

Rauscher, E., and K. Menou (2013), Three-dimensional atmospheric circulation models of hd 189733b and hd 209458b with consistent magnetic drag and ohmic dissipation, *The Astrophysical Journal*, *764*(1), 103, doi:10.1088/0004-637x/764/1/103.

Rauscher, E., V. Suri, and N. B. Cowan (2018), A More Informative Map: Inverting Thermal Orbital Phase and Eclipse Light Curves of Exoplanets, *AJ*, *156*(5), 235, doi:10.3847/1538-3881/aae57f.

Rogers, T. M. (2017), Constraints on the magnetic field strength of HAT-P-7 b and other hot giant exoplanets, *Nature Astronomy*, *1*, 0131, doi:10.1038/s41550-017-0131.

Rogers, T. M., and T. D. Komacek (2014), MAGNETIC EFFECTS IN HOT JUPITER ATMOSPHERES, *The Astrophysical Journal*, *794*(2), 132, doi:10.1088/0004-637x/794/2/132.

Rogers, T. M., and J. N. McElwaine (2017), The Hottest Hot Jupiters May Host Atmospheric Dynamos, *ApJ*, *841*(2), L26, doi:10.3847/2041-8213/aa72da.

Rogers, T. M., and A. P. Showman (2014), MAGNETOHYDRODYNAMIC SIMULATIONS OF THE ATMOSPHERE OF HD 209458b, *The Astrophysical Journal*, *782*(1), L4, doi:10.1088/2041-8205/782/1/l4.

Roman, M., and E. Rauscher (2017), Modeling the effects of inhomogeneous aerosols on the hot jupiter kepler-7b's atmospheric circulation, *The Astrophysical Journal*, *850*(1), 17.

Roman, M. T., E. M.-R. Kempton, E. Rauscher, C. K. Harada, J. L. Bean, and K. B. Stevenson (2021), Clouds in three-dimensional models of hot jupiters over a wide range of temperatures. i. thermal structures and broadband phase-curve predictions, *The Astrophysical Journal*, *908*(1), 101, doi:10.3847/1538-4357/abd549.

Rothman, L. S., I. Gordon, R. Barber, H. Dothe, R. R. Gamache, A. Goldman, V. Perevalov, S. Tashkun, and J. Tennyson (2010), Hitemp, the high-temperature molecular spectroscopic database, *Journal of Quantitative Spectroscopy and Radiative Transfer*, *111*(15), 2139–2150.

Sánchez-López, A., et al. (2019), Water vapor detection in the transmission spectra of hd 209458 b with the carmenes nir channel, *A&A*, *630*, A53, doi:10.1051/0004-6361/201936084.

Savel, A. B., E. M.-R. Kempton, M. Malik, T. D. Komacek, J. L. Bean, E. M. May, K. B. Stevenson, M. Mansfield, and E. Rauscher (2022a), No umbrella needed: Confronting the hypothesis of iron rain on wasp-76b with post-processed general circulation models, *The Astrophysical Journal*, *926*(1), 85.

Savel, A. B., E. M.-R. Kempton, M. Malik, T. D. Komacek, J. L. Bean, E. M. May, K. B. Stevenson, M. Mansfield, and E. Rauscher (2022b), No umbrella needed: Confronting the hypothesis of iron rain on wasp-76b with post-processed general circulation models, *The Astrophysical Journal*, *926*(1), 85.

Savel, A. B., E. M. R. Kempton, E. Rauscher, T. D. Komacek, J. L. Bean, M. Malik, and I. Malsky (2023), Diagnosing limb asymmetries in hot and ultra-hot Jupiters with high-resolution transmission spectroscopy, *arXiv e-prints*, arXiv:2301.01694.

Schwarz, H., M. Brogi, R. de Kok, J. Birkby, and I. Snellen (2015), Evidence against a strong thermal inversion in HD 209458b from high-dispersion spectroscopy, *A&A*, *576*, A111, doi:10.1051/0004-6361/201425170.

Schwarz, H., C. Ginski, R. J. de Kok, I. A. G. Snellen, M. Brogi, and J. L. Birkby (2016), The slow spin of the young substellar companion GQ Lupi b and its orbital configuration, *A&A*, *593*, A74, doi:10.1051/0004-6361/201628908.

Seidel, J. V., et al. (2019), Hot Exoplanet Atmospheres Resolved with Transit Spectroscopy (HEARTS). II. A broadened sodium feature on the ultra-hot giant WASP-76b, *A&A*, *623*, A166, doi:10.1051/0004-6361/201834776.

Showman, A. P., and T. Guillot (2002), Atmospheric circulation and tides of "51 Pegasus b-like" planets, *A&A*, *385*, 166–180, doi:10.1051/0004-6361:20020101.

Showman, A. P., and L. M. Polvani (2011), Equatorial Superrotation on Tidally Locked Exoplanets, *ApJ*, *738*(1), 71, doi:10.1088/0004-637X/738/1/71.

Showman, A. P., J. J. Fortney, Y. Lian, M. S. Marley, R. S. Freedman, H. A. Knutson, and D. Charbonneau (2009), Atmospheric Circulation of Hot Jupiters: Coupled Radiative-Dynamical General Circulation Model Simulations of HD 189733b and HD 209458b, *ApJ*, *699*(1), 564–584, doi:10.1088/0004-637X/699/1/564.

Showman, A. P., J. Y. K. Cho, and K. Menou (2010), *Atmospheric Circulation of Exoplanets*, pp. 471–516, University of Arizona Press.

Showman, A. P., J. J. Fortney, N. K. Lewis, and M. Shabram (2013), Doppler Signatures of the Atmospheric Circulation on Hot Jupiters, *ApJ*, *762*(1), 24, doi:10.1088/0004-637X/762/1/24.

Showman, A. P., X. Tan, and V. Parmentier (2020), Atmospheric Dynamics of Hot Giant Planets and Brown Dwarfs, *arXiv e-prints*, arXiv:2007.15363.

Snellen, I. A. G., R. J. de Kok, E. J. W. de Mooij, and S. Albrecht (2010), The orbital motion, absolute mass and high-altitude winds of exoplanet HD209458b, *Nature*, *465*(7301), 1049–1051, doi:10.1038/nature09111.

Snellen, I. A. G., B. R. Brandl, R. J. de Kok, M. Brogi, J. Birkby, and H. Schwarz (2014), Fast spin of the young extrasolar planet β Pictoris b, *Nature*, *509*(7498), 63–65, doi:10.1038/nature13253.

Stassun, K. G., K. A. Collins, and B. S. Gaudi (2017), Accurate Empirical Radii and Masses of Planets and Their Host Stars with Gaia Parallaxes, *AJ*, *153*(3), 136, doi:10.3847/1538-3881/aa5df3.

Stock, J. W., D. Kitzmann, A. B. C. Patzer, and E. Sedlmayr (2018), FastChem: A computer program for efficient complex chemical equilibrium calculations in the neutral/ionized gas phase with applications to stellar and planetary atmospheres, *MNRAS*, *479*(1), 865–874, doi:10.1093/mnras/sty1531.

Stock, J. W., D. Kitzmann, and A. B. C. Patzer (2022), FASTCHEM 2 : an improved computer program to determine the gas-phase chemical equilibrium composition for arbitrary element distributions, *MNRAS*, *517*(3), 4070–4080, doi:10.1093/mnras/stac2623.

Tabernero, H. M., et al. (2021), ESPRESSO high-resolution transmission spectroscopy of WASP-76 b, *A&A*, *646*, A158, doi:10.1051/0004-6361/202039511.

Tan, X., and T. D. Komacek (2019), The atmospheric circulation of ultra-hot jupiters, *The Astrophysical Journal*, *886*(1), 26, doi:10.3847/1538-4357/ab4a76.

Taylor, J., V. Parmentier, P. G. J. Irwin, S. Aigrain, E. K. H. Lee, and J. Krissansen-Totton (2020), Understanding and mitigating biases when studying inhomogeneous emission spectra with JWST, *MNRAS*, *493*(3), 4342–4354, doi:10.1093/mnras/staa552.

Thorngren, D., P. Gao, and J. J. Fortney (2019), The Intrinsic Temperature and Radiative-Convective Boundary Depth in the Atmospheres of Hot Jupiters, *ApJ*, *884*(1), L6, doi:10.3847/2041-8213/ab43d0.

Thorngren, D. P., and J. J. Fortney (2018), Bayesian Analysis of Hot-Jupiter Radius Anomalies: Evidence for Ohmic Dissipation?, *AJ*, *155*(5), 214, doi:10.3847/1538-3881/aaba13.

Thorngren, D. P., J. J. Fortney, R. A. Murray-Clay, and E. D. Lopez (2016), The Mass-Metallicity Relation for Giant Planets, *ApJ*, *831*(1), 64, doi:10.3847/0004-637X/831/1/64.

Thorngren, D. P., J. J. Fortney, E. D. Lopez, T. A. Berger, and D. Huber (2021), Slow Cooling and Fast Reinflation for Hot Jupiters, *ApJ*, *909*(1), L16, doi:10.3847/2041-8213/abe86d.

Thrastarson, H. T., and J. Y.-K. Cho (2011), Relaxation Time and Dissipation Interaction in Hot Planet Atmospheric Flow Simulations, *ApJ*, *729*(2), 117, doi:10.1088/0004-637X/729/2/117.

Toon, O. B., C. P. McKay, T. P. Ackerman, and K. Santhanam (1989), Rapid calculation of radiative heating rates and photodissociation rates in inhomogeneous multiple scattering atmospheres, *J. Geophys. Res.*, *94*, 16,287–16,301, doi:10.1029/JD094iD13p16287.

Tsiaras, A., et al. (2018), A population study of gaseous exoplanets, *The Astronomical Journal*, *155*(4), 156, doi:10.3847/1538-3881/aaaf75.

Turner, J. D., et al. (2021), The search for radio emission from the exoplanetary systems 55 Cancri, υ Andromedae, and τ Boötis using LOFAR beam-formed observations, *A&A*, *645*, A59, doi:10.1051/0004-6361/201937201.

van Sluijs, L., et al. (2022), Carbon monoxide emission lines reveal an inverted atmosphere in the ultra hot Jupiter WASP-33 b and indicate an eastward hot spot, *arXiv e-prints*, arXiv:2203.13234.

Wallace, J., and P. Hobbs (2006), *Atmospheric Science: An Introductory Survey*, International geophysics series, Elsevier Academic Press.

Wang, H., and R. Wordsworth (2020), Extremely long convergence times in a 3d GCM simulation of the sub-neptune gliese 1214b, *The Astrophysical Journal*, *891*(1), 7, doi:10.3847/1538-4357/ab6dcc.

Wardenier, J. P., V. Parmentier, E. K. H. Lee, M. R. Line, and E. Gharib-Nezhad (2021), Decomposing the iron cross-correlation signal of the ultra-hot Jupiter WASP-76b in transmission using 3D Monte Carlo radiative transfer, *MNRAS*, *506*(1), 1258–1283, doi:10.1093/mnras/stab1797.

Wardenier, J. P., V. Parmentier, and E. K. H. Lee (2022), All along the line of sight: a closer look at opening angles and absorption regions in the atmospheres of transiting exoplanets, *MNRAS*, *510*(1), 620–629, doi:10.1093/mnras/stab3432.

West, R. G., et al. (2016), Three irradiated and bloated hot Jupiters:. WASP-76b, WASP-82b, and WASP-90b, *A&A*, *585*, A126, doi:10.1051/0004-6361/201527276.

Wills, R. C., and T. Schneider (2016), How Stationary Eddies Shape Changes in the Hydrological Cycle: Zonally Asymmetric Experiments in an Idealized GCM, *Journal of Climate*, *29*(9), 3161–3179, doi:10.1175/JCLI-D-15-0781.1.

Wittenmyer, R. A., et al. (2020), Cool Jupiters greatly outnumber their toasty siblings: occurrence rates from the Anglo-Australian Planet Search, *MNRAS*, *492*(1), 377–383, doi:10.1093/mnras/stz3436.

Wu, Y., and Y. Lithwick (2011), Secular Chaos and the Production of Hot Jupiters, *ApJ*, *735*(2), 109, doi:10.1088/0004-637X/735/2/109.

Wu, Y., and Y. Lithwick (2013), Ohmic Heating Suspends, Not Reverses, the Cooling Contraction of Hot Jupiters, *ApJ*, *763*(1), 13, doi:10.1088/0004-637X/763/1/13.

Yadav, R. K., and D. P. Thorngren (2017), Estimating the Magnetic Field Strength in Hot Jupiters, *ApJ*, *849*(1), L12, doi:10.3847/2041-8213/aa93fd.

Yu, C. (2020), Thermally Driven Angular Momentum Transport in Hot Jupiters, *ApJ*, *893*(1), L22, doi:10.3847/2041-8213/ab84e9.

Yuk, I.-S., et al. (2010), Preliminary design of IGRINS (Immersion GRating INfrared Spectrograph), in *Ground-based and Airborne Instrumentation for Astronomy III*, *Society of Photo-Optical Instrumentation Engineers (SPIE) Conference Series*, vol. 7735, edited by I. S. McLean, S. K. Ramsay, and H. Takami, p. 77351M, doi:10.1117/12.856864.

Žák, J., P. Kabáth, H. M. J. Boffin, V. D. Ivanov, and M. Skarka (2019), High-resolution transmission spectroscopy of four hot inflated gas giant exoplanets, *The Astronomical Journal*, *158*(3), 120, doi:10.3847/1538-3881/ab32ec.

Zellem, R. T., et al. (2014), THE 4.5 m FULL-ORBIT PHASE CURVE OF THE HOT JUPITER HD 209458b, *The Astrophysical Journal*, *790*(1), 53, doi:10.1088/0004-637x/790/1/53.

Zhang, J., E. M. R. Kempton, and E. Rauscher (2017), Constraining Hot Jupiter Atmospheric Structure and Dynamics through Doppler-shifted Emission Spectra, *ApJ*, *851*(2), 84, doi:10.3847/1538-4357/aa9891.

Zhang, Y., et al. (2022), Transmission spectroscopy of the ultra-hot Jupiter MASCARA-4 b. Disentangling the hydrostatic and exospheric regimes of ultra-hot Jupiters, *A&A*, *666*, A47, doi:10.1051/0004-6361/202244203.

Zhu, W., and S. Dong (2021), Exoplanet Statistics and Theoretical Implications, *ARA&A*, *59*, 291–336, doi:10.1146/annurev-astro-112420-020055.